University of Strathclyde
Department of Naval Architecture, Ocean and Marine Engineering

An investigation into the characteristics and optimisation of a high-pressure common rail injection system

By

NAO HU

A thesis presented in fulfilment of the requirements
for the degree of Doctor of Philosophy

21 September 2017

To my wife, Qishan Li

Abstract

The primary aim of this research was to predict the emissions and fuel savings when replacing a mechanical fuel oil injection system with a high pressure common rail one. The work in this study consists of two parts. In the first part, a novel routine is proposed for the optimisation of electronic fuel injectors and their dynamic response, including the needle valve opening delay and the needle valve closing delay (The needle valve opening delay refers to the delay between the control signal being trigged and the needle valve being fully open; the needle valve closing delay refers to the delay between the control signal deactivating and the needle valve being fully closed). Two injectors (Type-I and Type-II) were included; their one-dimensional (1D) models were built in AMESim software and validated respectively.

A parametric study on the Type-I fuel injector was conducted before the optimisation process in order to examine the effects of various parameters including the control piston diameter (CPD), control oil (i.e. the fuel oil used for control in a typical solenoid electronic fuel injector) inlet passage diameter (IPD) and control oil outlet passage diameter (OPD) on injection characteristics, i.e. injection rate, injection mass, needle valve lift and control chamber pressure. Then, the optimisation of the injector dynamic response was investigated by the proposed routine in modeFRONTIER software. In detail, the routine included the following steps: First, a random sequence was adopted in the design of experiment (DOE) type. Then, an NSGA-II (Non-dominated Sorting Genetic Algorithm II) algorithm was selected. Next, a whole electronic fuel injector model was chosen, where the displacements of the needle valve were generated. These data were first written into an input file, and to do this, appropriate writing and reading rules needed to be developed. The text file was read by the MATLAB code, where the control signal and needle valve displacement timings were calculated. The valve opening delay and the valve closing delay were thus obtained from these timings. Additionally, a constraint was set between the control oil inlet passage diameter and control oil outlet passage diameter in that the former should be smaller than the latter in each run.

The CPD, OPD and IPD were the three design parameters to be varied in the optimisation process of the Type-I fuel injector at a specific rail pressure. However, three more design parameters (the spring preload force (SPF), nozzle orifice number (NZN) and nozzle orifice diameter (NZD)) were involved in the optimisation process of the Type-II fuel injector under three different rail pressures (80 MPa, 120 MPa and 160 MPa). The optimal design with the best trade-off between the valve opening delay and the valve closing delay of each fuel injector was singled out via a scattering chart. Results show that the optimum Type-I fuel injector achieved reductions of 40% and 25% of the baseline design on the valve opening delay and valve closing delay respectively. The optimal design of the Type-II fuel injector also achieved a huge reduction at all three rail pressures. Specifically, the valve opening delay was reduced by 29.8%, 29.2% and 20.9%, and the valve closing delay was reduced by 25.6%, 24.5% and 30.1% at 80 MPa, 120 MPa and 160 MPa rail pressures respectively. RSM (response surface method) contour maps were used to study the interactions between design parameters. Results indicated that the CPD, IPD and OPD and their interactions are influential design parameters for the valve opening delay, while the IPD has a dominant effect on the valve closing delay. A large CPD together with a large IPD was found to increase the valve opening delay dramatically. Surprisingly, the effects of the spring preload force (SPF) on the valve closing delay are noticeable at low rail pressures. The valve closing delay decreases with an increase in the spring preload force. The feasibility and efficiency of the proposed routine was validated both on the Type-I fuel injector and the Type-II fuel injector. It was not only achieved great reductions on both the valve opening delay and the valve closing delay, but was also able to comprehensively disclose the effects and interactions of the design parameters on the injector dynamic response.

In the second part, Type-II fuel injector matches with the combustion chamber of a medium-speed marine diesel engine was conducted by a CFD model of the medium-speed marine diesel engine built in AVL FIRE software. The model was validated by using the cylinder pressures, rate of heat release (ROHR) and NO_x emissions under four engine loads, i.e. L25 (25%), L50 (50%), L75 (75%) and L100 (100%) loads. Seven engine design parameters, including four injection-related

parameters (spray angle, nozzle protrusion length, injection timing and swirl ratio) and three combustion chamber geometry parameters (bowl diameter, centre crown height and toroidal radius), were examined by a parametric study and a multi-objective optimisation.

The parametric study was carried out to discover the sensitivity of design parameters on the objectives (nitrogen oxides (NO_x) emissions, soot emissions and specific fuel oil consumption (SFOC)). In it, each engine design parameter was investigated independently under three engine loads (25% engine load was excluded due to the fact that it is very unstable operating condition). Results showed that the injection-related parameters were found to have much more influence than the combustion chamber geometries. In addition, the injection timing, one of the injection-related parameters, has the largest influence on the objectives.

In the optimisation study, two algorithms (the nonlinear programming by quadratic Lagrangian (NLPQL) algorithm and multi-objective genetic algorithm (MOGA)) were used in two stages, initially separately and then sequentially, for the first time in the engine optimisation domain. This study aims to reduce the NOx emission, soot emissions as well as to improve fuel economy. Detailed comparisons were made for NO_x emissions, soot emissions and SFOC as well as the design parameters. The optimisation study showed that the NLPQL algorithm failed to obtain optimal designs whilst the MOGA offered more feasible Pareto designs. Since the NLPQL algorithm is a local optimisation method, and as a result it is affected by the selection of appropriate initial conditions. The optimal design with the best trade-off between NO_x and soot emissions obtained by the MOGA was set as the starting point of the NLPQL algorithm. In this case, a better design with lower NO_x emissions and soot emissions was obtained. The combustion processes of these optimal designs were also analysed and compared in detail. Late injection and small swirl ratio were reckoned to be the main reasons for reducing NO_x emissions. In the end, contour maps generated by response surface method (RSM) were applied in order to gain a better understanding of the interaction and sensitivity of the design parameters on NO_x emissions, soot emissions and SFOC. Results indicated that NO_x emissions and

soot emissions can be greatly reduced by adopting a late injection, a low swirl and a large spray angle, but fuel economy was sacrificed.

Acknowledgement

After a long time of hard working, this thesis is finished finally. During the long journey of the study, many people contributed to this thesis, and now, I would like to acknowledge them. First of all, I would like to deliver my deepest gratitude to my supervisors, Professor Peilin Zhou and Professor Jianguo Yang, for their invaluable guidance not only on the course study, research skills cultivation, articles and thesis writing but also on the behaviour to conduct oneself in life. I wouldn't be more grateful for Professor Peilin Zhou, who offered me the opportunity to study in the UK and this would be the most impressive experience in my life. I can never forget Professor Jianguo Yang, for his consistent appreciation, urging and encouragement. Their vast knowledge, rigorous scholarship and charming personalities set examples for my future improvements. As a PhD student, I am really lucky to have a chance to get constructions from the two supervisors and have an access to the facilities in both the UK and China.

I would also like to thank Professor Yonghua Yu for his insightful comments and suggestions. And thanks Professor Fucai Hu and Professor Yuhai He, your care and help will not be forgotten. Special thanks to Mrs Thelma Will, who provides helps and handles all kinds of problems I met in the first three years of my PhD study.

My sincere thanks also go to Dr Haibin Wang, Dr Qinpeng Wang, Dr Lei Hu, Dr Ying Hu, Dr Xinna Tian, Dr Yifang Han, Dong Han and other fellows, for the continual support and the harmony research environment they offered. Without their help, this thesis would not have been so smooth.

The author also wants to thank the Lloyd's Register of shipping for the financial support on the year 2015, without which I wouldn't have able to live in the UK.

Special thanks to my father Youfang Hu and mother Xiaolan Wang. Words cannot express how grateful I am for all of the sacrifices that you've made. Wherever I sailed, you are always my warm harbour. At the end, I would like to express appreciation to my beloved wife Qishan Li who gives me meticulous care, company and encouragement. You swept away pressures throughout the years of my PhD study. I really lucky and grateful to have you fight side by side for our future.

Content

List of Figures

List of Tables

Nomenclature List

A_0	geometrical cross section of the passage or orifice, m^2
$\overline{c_p}$	average specific heat, J/(kg·K)
c_p^0	specific heat when temperature is T_0, J/(kg·K)
C_c	contraction coefficient
C_d	discharge coefficient
CN	cavitation number
Compact RIO	a real-time embedded industrial controller made by National Instruments
d003	connection length
D_o	outlet diameter, mm
E	set
f	function
F_{hj}	enthalpy diffusion flux on x_j direction
$g_j(x)$	constraints
h	enthalpy, J
h_t	heat enthalpy, J
H_m	heat generated by component *m*
h001	bowl radius, mm
j	variable
k	objective number

L100	full engine load
L25	25% engine load
L50	50% engine load
L75	75% engine load
LABCAR	a flexible test system developed by ETAS Company
m_e	real number
$\dot{i}_{,}$	mass flow rate, g/s
M_m	molecular molar mass of composition m
N	maximum objective numbers
NO_x_b	NO_x emissions of the base-line design
NO_x_M	design of minimum NO_x emissions with MOGA method
NO_x_N	design of minimum NO_x emissions with NLPQL method
OPT_M	design with best balance of MOGA algorithm
OPT_M&N	best design of sequential method
OPT_N	best design of NLPQL algorithm
O_i	objectives of merit function
PAHs	gas-phase precursors
P_b	back pressure, MPa
P_{inj}	injection pressure, MPa
P_v	saturation vapour pressure, MPa
r002	toroidal radius, mm
Re	Reynolds number

R^n	n-dimensional real space
s_h	energy source component
s_i	momentum source component
SFOC_b	specific fuel oil consumption of baseline design
SFOC_M	design of minimum SFOC with MOGA
SFOC_N	design of minimum SFOC with NLPQL
Soot_b	soot emission of baseline design
Soot_M	design of minimum soot emissions with MOGA method
Soot_N	design of minimum soot emissions with NLPQL method
t	time, s
T	temperature, K
t1	moment of the control signal starts to be initialised
T1	moment of the needle valve starts to open
t2	moment of the control signal has reached to its maximum amplitude
T2	moment of the needle valve has reached its maximum displacement
t3	moment of the control signal begins to be de-activated
T3	moment of the needle valve begins to close
t4	moment of the control signal has fully closed
T4	moment of the needle valve has fully closed
u_i	velocity component
U_o	velocity of the orifice outlet, m/s
v	velocity, m/s

v001	distance from the centre of toroidal surface to the piston top surface, mm
v002	clearance, mm
v003	crown centre height, mm
v_f	kinematic viscosity, Ns/m^2
x	n-dimensional parameter vector
$\vec{x}^*$	Pareto design
$\vec{x}_j$	arbitrary design
$\vec{x}_j$	lower boundary of x
x_Q	
x_u	upper boundary of x
Y_m	mass fraction of component m

Greek symbols

μ	micro
μ_i	weight
ρ	density, kg/m3
τ_{ij}	tensor component

Abbreviation List

1D	one dimensional

2D	two dimensional
3D	three dimensional
ARMOGA	adaptive range multi-objective genetic algorithm
ATDC	after top dead centre
BTDC	before top dead centre
CPD	control piston diameter
CFD	computational fluid dynamics
CO	carbon monoxide
CO2	carbon dioxide
DI	direct injection
DNA	deoxyribonucleic acid
DOE	design of experiment
DSP	digital signal processing
ECA	emission control area
ECU	electronic control unit
EGR	exhaust gas recirculation
Exp.	experimental
FPGA	field programmable gate array
GA	genetic algorithm
HC	hydrocarbons
HIL	hardware in loop
HFO	heavy fuel oil
HP	high-pressure

HPCR	High pressure common rail
IMO	internal maritime organization
IPD	control oil inlet passage diameter
I/O	input/output
LDC	lower dead centre
LDO	light diesel oil
LES	large eddy simulation
LMA	Levenberg-Marquardt algorithm
MARPOL	the international convention for the prevention of pollution from ships
MOGA	multi-objective genetic algorithm
NLPQL	non-linear programming by quadratic Lagrangian
NN	neural networks
NO_x	nitrogen oxides
NPL	nozzle protrusion length
NSGA II	non-dominated sorting genetic algorithm II
NZD	nozzle orifice diameter
NZN	nozzle orifice number
OPD	control oil outlet passage diameter
PID	proportional-integral-derivative
Piso	pressure implicit split operator
PSO	particle swarm optimisation
PLC	programmable logic controller
ROHR	rate of heat release

RSM	response surface methodology
SA	spray angle
SCR	selective catalytic reduction
SFOC	specific fuel oil consumption
Sim.	simulation
Simple	semi-implicit method for pressure linked equations
Sobol	quasi-random low-discrepancy sequences
SOI	start of injection
SPF	spring preload force
SQP	sequential quadratic programming
SR	swirl ratio
SS-ANOVA	smoothing spline analysis of variance
TDC	top dead centre
TWC	three-way catalytic

Chapter 1. Introduction

1.1. Background

Energy is a continual pursuit of humankind. One of the most common sources of energy is fossil energy, especially oil, which significantly affects the world's economic development. Every time its price increases, a financial tsunami is caused. This is reflected in the three oil crises in the past four decades. The first oil crisis happened in October 1973, which lasted for nearly half a year: oil price rose to three times its initial price. The high price of oil triggered the worst global crisis since the Second World War. The second oil crisis happened in 1979: the price of crude oil doubled in the following 12 months due to a severe reduction of oil output. It is recognised as the main reason for causing economic recession in the USA and other countries. The third oil crisis, which lasted nine months, was in response to the Iraqi invasion of Kuwait on 2nd August, 1990.

Although the price of oil has reached its lowest these days, due to the low demand of a slowing-down world economy, the main trend increases steadily over a long period of time. Since adequate substitutes in the marine domain have not been developed yet, fossil oil will play an indispensable role in the future for a long period of time.

About 90% of the world's trade is transported by ships, which are mainly powered by marine diesel engines. A high fossil oil price results in a high operating cost and a low economic benefit. In addition, ships are causing intolerable pollution as their number grows. Compared to automotive diesel engines, marine diesel engines exhaust far less carbon monoxide (CO), carbon dioxide (CO_2) and hydrocarbon (HC), but generate a high level of NO_x emissions. It is reported that NO_x emissions are estimated to be about 10 million tons per annum, which is equivalent to about 14% of total global NO_x emissions from fossil fuels [1]. Facing such a severe situation, IMO expressly stipulated what the NO_x emissions should be in the revised MARPOL (the international convention for the prevention of pollution from ships) Annex VI, as shown in Table 1-1. Tier II NO_x emission regulation came into force for engines

mounted on a ship constructed on or after 1st January, 2011. It stipulated the reduction of NO_x emissions up to 20% in comparison to Tier I regulations in the global area. The more stringent Tier III regulations were applied to engines installed on ships constructed on or after 1st January, 2016, operating in ECAs (emission control areas). It requires a reduction of NO_x emissions up to 80% from the Tier I regulations. Tier II regulations are still applied for ships operating outside of the ECAs.

Table 1-1 IMO NO_x emission regulations [2, 3]

Rated Speed n (r/min)	n<130	130≤n ≤2000	n>2000
Tier I (2000)/ g/(kWh)	17.0	$45 \cdot n^{-0.2}$	9.84
Tier II (2011)/ g/(kWh)	14.36	$44 \cdot n^{-0.23}$	7.66
Tier III (2016)/ g/(kWh) none ECAs	14.36	$44 \cdot n^{-0.23}$	7.66
Tier III (2000)/ g/(kWh) ECAs	3.4	$9 \cdot n^{-0.2}$	1.97

Emissions and pollution are already threatening life on the planet. It is necessary to have these emissions and pollution reduced and under control in every aspect, including pollution from ships. Most of the emissions from ships are generated by marine diesel engines. Measurements for boosting engine performance and cutting down emissions can be taken from two aspects, i.e. adopting advanced engine control technologies or after-treatment technologies. The former usually refers to the technologies of HPCR fuel oil injection, adjustable turbocharger, Miller cycle, low emission combustion and clean fuel combustion (nature gas, dual fuel) [4]. The latter consists of the oxidation catalyst, exhaust particles purifier, SCR, EGR, TWC (three-way catalytic) and NO_x absorber-reduction catalytic converter [5-7].The HPCR fuel oil injection system is one of the most extensively used technologies for the control of internal combustion engines. However, some marine diesel engines

operating can only meet the Tier I emission regulations. These engines are still using mechanical fuel oil injection systems, which cannot improve their emission levels by adjusting fuel oil injection settings. A promising choice for these engines is to be retrofitted with HPCR systems. A HPCR system provides a flexible control over engine injection laws, disregarding engine loads and speed, and at the same time, a finer fuel atomization is achieved due to a higher and more stable injection pressure.

1.2. Aim and Objectives

The primary aim of this thesis was to predict the emission and fuel economy when replacing a mechanical fuel oil injection system with a high pressure common rail one.

The electronic fuel injector, one of the key components of a HPCR system, is of particular significance. Its dynamic response affects the shape of the fuel oil injection rate and the delay to the start of injection; thus, a good dynamic response gives a great way of achieving a precise injection and offers flexible control to the multi-injection. However, an electronic fuel injector is a precision device that integrates mechanical, electronic and hydraulic technologies. The optimisation of an electronic fuel injector in order to have an excellent dynamic response is of great interest to both researchers and engineers. In this respect, the first objective is to find balanced dynamic response (valve opening delay and valve closing delay) of Type-I (a typical Bosch solenoid fuel injector for automotive applications) and Type-II (a newly-designed electronic fuel injector for medium-speed marine diesel engines) fuel injectors.

Additionally, the designed Type-II fuel injector matches with the combustion chamber of a medium-speed marine diesel engine is studied. However, combustion is very susceptible to the match status of the fuel injector and combustion chamber. Without a proper match, the performance, emissions and fuel economy might also be unsatisfied. Thus, the second objective is to find a set of design parameters which contribute to the reduction of NO_x emissions and soot emissions, and improve fuel

economy. This was studied thoroughly through a parametric study and a multi-objective optimisation executed with a CFD model in FIRE software.

1.3. Innovation and contribution

Since two objectives are involved in this thesis, it can be naturally divided into two parts, with each part having connections with the other. The first part deals with the optimisation of the dynamic response of two types of electronic fuel injectors. Then, in the second part, one of the injectors is selected for the match optimisation with a combustion chamber of a medium-speed marine diesel engine. The main innovation and contribution are stated below.

(1) Optimisation of structural parameters on injector dynamic response

In the first part, an optimisation routine is proposed for the optimisation of the dynamic response of electronic fuel injectors. The feasibility and efficiency of the proposed optimisation routine was validated on the Type-I fuel injector. The following are the most significant developments described and presented in the investigation of a Type-I electronic fuel injector:

- To understand the influence of injector structural parameters including the control piston diameter, control oil inlet passage diameter and control oil outlet diameter on injection characteristics, a parametric study of the Type-I fuel injector was carried out.

- To find a set of optimal structural parameters of the Type-I electronic fuel injector, an optimisation routine was built in the modeFRONTIER, in which a MOGA method was applied.

- To analyse the effect of the electronic fuel injector structural parameters on the dynamic response, RSM (response surface method) was adopted.

- To single out a Pareto optimum for the Type-I fuel injector with the best

trade-off between the valve opening delay and the valve closing delay, scattering charts were used.

When the optimisation routine was fully validated it was applied to the optimisation of the Type-II fuel injector. The following are the most crucial developments reported in the investigation of the Type-II electronic fuel injector:

- To demonstrate the 1D modelling technology, a detailed model of the Type-II fuel injector was built in AMEsim according to structure parameters of the authentic electronic fuel injector.

- To obtain the best design of the Type-II electronic fuel injector, the proposed optimisation routine was adopted and two more design parameters were considered.

- To cut down analysis complexity, the sensitivity of design parameters on the dynamic response was analysed before the RSM study.

(2) Type-II fuel injector match with a combustion chamber

In the second part, the match study of the Type-II fuel injector and a combustion chamber was carried out by both the parametric study and the multi-objective optimisation. A total of seven design parameters, including four injection-related parameters and three combustion chamber geometry parameters, were included in the study. Two optimisation methods, the NLPQL algorithm and the MOGA, were also included. The former is used for the optimisation of diesel engine by only a few researchers, while the latter is the most frequently used one in solving multi-objective problems. These two algorithms are compared and used sequentially for the optimisation of a medium-speed marine diesel engine with seven design parameters to be optimised. The following points present the main contributions and the innovations of the match study:

- To gain a better understanding of how design parameters of the Type-II fuel

injector and combustion chamber affect emissions and fuel economy, a CFD model was used in FIRE software and a parametric study was conducted under three engine loads.

- To investigate the efficiency of multi-objective algorithms for engine match optimisation, the NLPQL algorithm and MOGA method were compared on four aspects, i.e. optimisation history, objectives, design parameters and the combustion process.

- To discover a better optimal design and investigate the initial conditions of the NLPQL algorithm, the optimal design obtained from the MOGA method was set as the starting point of the NLPQL algorithm.

- To examine the interactions and the sensitivities of design parameters on emissions and fuel economy, RSM surfaces were created with neural networks.

1.4. Organisation of the thesis

As was stated previously, the thesis has two objectives and thus the contents are divided into two parts. The main work of the first part is included in chapters 3 and 4. And the main work of the second part is in chapters 5 to 7. The organisation of the thesis is listed below:

- Chapter 1 introduces the background, objectives, innovations and contributions of the study.

- Chapter 2 reports the history and literature review of fuel oil injection technologies, high-pressure common rail fuel oil injection systems of marine diesel engines, numerical simulation of the in-cylinder process and hardware-in-loop systems.

- Chapter 3 validates the proposed optimisation routine of the Type-I electronic fuel injector. A parametric study was performed to investigate the effects of the control piston diameter, control oil inlet passage diameter and control oil outlet passage diameter on injection characteristics. Then an optimisation routine was built and the multi-objective optimisation was carried out to discover the optimal design. The interactions and the sensitivities of design parameters on the dynamic response were disclosed by using RSM.

- Chapter 4 introduce the validated optimisation routine for the optimisation of the Type-II fuel injector, which is designed especially for medium-speed marine diesel engines. Three more design parameters were added and the sensitivity of design parameters was found. Finally, an optimum was obtained and compared with the baseline design.

- Chapter 5 shows the mesh, equations and models used for the CFD in-cylinder process simulation. The final model was verified by cylinder pressures, ROHR and NO_x emissions under four engine loads.

- Chapter 6 introduces a parametric study, the impacts of the spray angle, nozzle protruding length, injection timing, swirl ratio, bowl diameter, centre crown height and toroidal radius on NO_x emissions, soot emissions and SFOC were carefully investigated under three engine loads.

- Chapter 7 compares and sequentially used of the NLPQL and MOGA methods for the optimisation of the medium-speed marine diesel engine with seven design parameters.

- Chapter 8 draws conclusions and gives recommendations for the future research.

Chapter 2. Critical review

2.1. A review of fuel oil injection systems of diesel engines

2.1.1. History of electronic fuel oil injection systems

The first electronic fuel oil injection system was developed by American Motors Corporation in 1957, and was called the Electrojector. Unfortunately, the Electrojector failed pre-production testing. In 1958, American Motors Corporation overcame some of the problems of the Electrojector and then successfully applied it to some engine types, e.g. the DeSoto Adventurer, the Dodge D-500, and the Plymouth Fury. These applications can be regarded as the first commercialisation fuel oil injection system. After that, Bosch bought the patent design and made a lot of improvements and upgrades [8]. In 1967, Bosch created a marketable fuel oil injection system, called the D-Jetronic. Electronic controller and sensors were adopted in the D-Jetronic to measure the air flow and air temperature, which enabled the accurate delivery of fuel mass; thus, fuel oil was conserved. In 1979, a new generation of D-Jetronic was developed by Bosch with the name of Motronic. A central control unit was used to control the ignition and fuel oil injection. Later, in 1995, Bosch introduced the e-gas for electronic throttle control. The e-gas can pass fuel, air and ignition signals from the throttle system to control units, based on what would achieve the best airflow control. Then in 2000, Bosh successfully applied the first gasoline direct injection system to the Volkswagen Lupo. The above events are the milestones in the history of the fuel oil injection system [9].

The common rail fuel oil injection system, which is dated back to the 1960s, was pioneered by Societe des Procedes Modernes D'Injection (SOPROMI) [10]. In the early 1970s, SOPROMI technology, created by CAV Ltd, beat the existing pump-line-nozzle system with slight advantages. Further improvements to common rail fuel oil injection systems are still needed if they are to be mature enough to be brought to the market.

In the 1980s, attempts were made by Industrieverband Fahrzeugbau (IFA) of the former East Germany and General Motors. The former developed a common rail fuel oil injection system for their W50 truck, but failed to take it to series production and the system was discarded a few years later [11]. The latter developed a common rail fuel oil injection system for their light-duty IDI engines [12] before further study was ended due to the cancellation of their light-duty diesel engine program. In the late 1980s and 1990s, a series of significant events occurred. Nippondenso developed a common rail system for commercial vehicles [13], which put into production in Hino Rising Ranger trucks in 1995. Bosch put its passenger car common rail fuel oil injection systems into production in 1997 [14].

Since then, common rail fuel oil injection systems became perspective into higher pressures with a lot more flexible lay-outs. Lots of competitors, for example, the Delphi Corp. and Denso Crop., have brought a variety of common rail fuel oil injection systems into the market.

2.1.2. Advantages of HPCR fuel oil injection systems

Nowadays, the applications of HPCR fuel oil injection systems have been the main trend in both automotive and marine diesel engines due to their overwhelming advantages in meeting the more stringent emission regulations and boosting engine power performance.

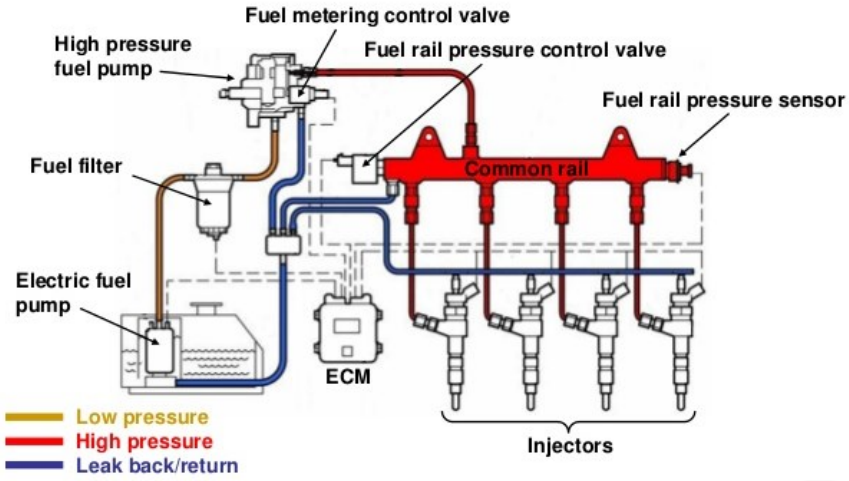

Figure 2-1 Schematic of HPCR fuel injection system

Figure 2-1 presents a schematic view of the components of a typical Bosch HPCR system, which includes one or more high pressure pumps, common rails, ECU, electronic fuel injectors, high pressure oil pipes and a variety of sensors and actuators. Compared to mechanical fuel oil injection systems, high pressure common rail systems have the following advantages:

(1) Pressure is built and transported independently of engine speed and load conditions.

This offers great flexibility for controlling fuel oil injection quantity and injection timing. Meanwhile, common rail fuel oil injection systems also improve the engine's performance and emissions at low engine speeds and loads with better spray penetration and finer spray droplets which are beneficial for fuel-air mixing. This kind of characteristic distinguishes common rail fuel oil injection systems from other fuel oil injection systems. As shown in Figure 2-2, the pressure of pump-line-nozzle system and EUI system rise with an increase in engine speed. However, the pressure of common rail fuel injection system is the same, a variety of fuel oil injection control strategies can be developed according to engine speed and operation load for boosting engine performance and reducing emissions.

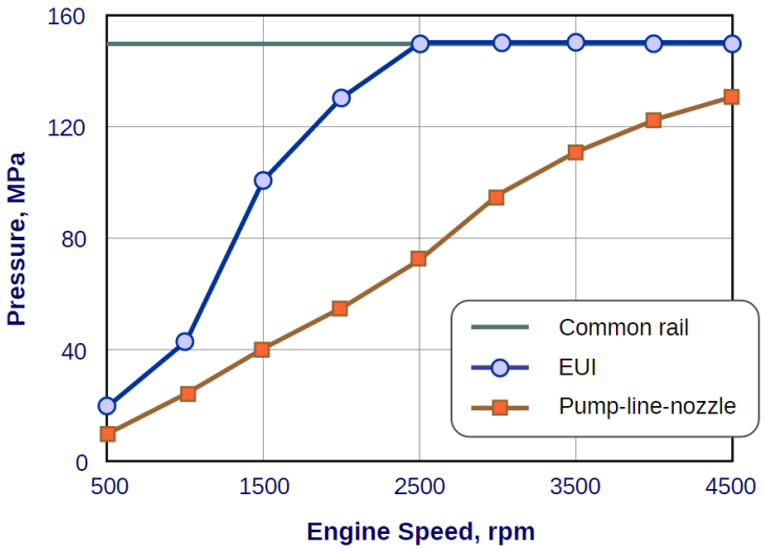

Figure 2-2 Pressure changes with engine speed

(2) Reduced emissions and combustion noise.

Pilot injection can be easily achieved in common rail fuel oil injection systems, which is capable of precise control over a small amount of pilot fuel oil injection quantities. Pilot injection was found to be one of the ways to realise low noise and NO_x emissions.

(3) Low fuel pump peak torque requirements

In traditional combustion engines, swirl plays an import role in fuel-air mixing. This is replaced in common rail fuel oil injection systems, which rely on higher rail pressure instead.

To generate the energy required to inject the fuel in approximately 1 millisecond, a conventional distributor pump needs a larger maximum pump torque and places a considerable strain on the drive shaft [15]. However, the peak torque requirements are much lower in common rail fuel oil injection systems. Fuel oil is delivered to the accumulator and thus the peak flow rate has nothing to do with the injection event or the distributor pump. In this circumstance, the pump discharge flow can be spread out over a longer portion of the engine cycle to keep pump torque demand more even [14].

When injection occurs in a HPCR system, a depression wave propagates from the nozzle along the injector feeding pipe and is then reflected, as a compression wave. It features hydraulic capacitance when the compression wave meets HPCR system components, i.e., common rail and HP pump delivery chamber. Therefore, the injection dynamics would be affected by the lay-out types, geometries, accumulation volume distributions. The compression wave mitigated the pressure drop in the accumulation volumes, a compensating action of compression wave on the pressure drop is stronger than for smaller accumulation volumes. Thus, the compression wave reduces the pressure differences between common rails and accumulation chambers, and explains for the fact that the flow-rate time histories are almost the same in these

volumes [16].

2.2. Typical HPCR systems for marine engines

The application of HPCR systems for marine engines have become prosperous since 1996. Some world-famous companies have developed and applied HPCR systems of their own. For example, Wärtsilä developed a HPCR system for W32CR diesel engines with heavy oil applications in 2003 and then created a new HPCR system with the cooperation of L' Organge for W20CR diesel engines in 2006. MAN B&W also developed a HPCR system for its 32/40 diesel engines in 2003. Deutz and MTU companies never fall behind, they developed their own HPCR systems with unique structure feathers. These systems are discussed below.

2.2.1. The Wärtsilä HPCR system

The HPCR system for the Wärtsilä W32CR marine diesel [17] is shown in Figure 2-3. It is suitable for heavy oil operation and the maximum operating pressure is 150 MPa. Oil is pumped into the accumulator by the mono-block HP pumps, which are driven by the camshaft of double projections. Pressure sensors are mounted on accumulators and check valves are installed between accumulators and injectors. Two injectors share the same accumulator. For safety reasons, two independent oil circle loops are used for controlling injectors, i.e. the control oil loop and the fuel oil loop.

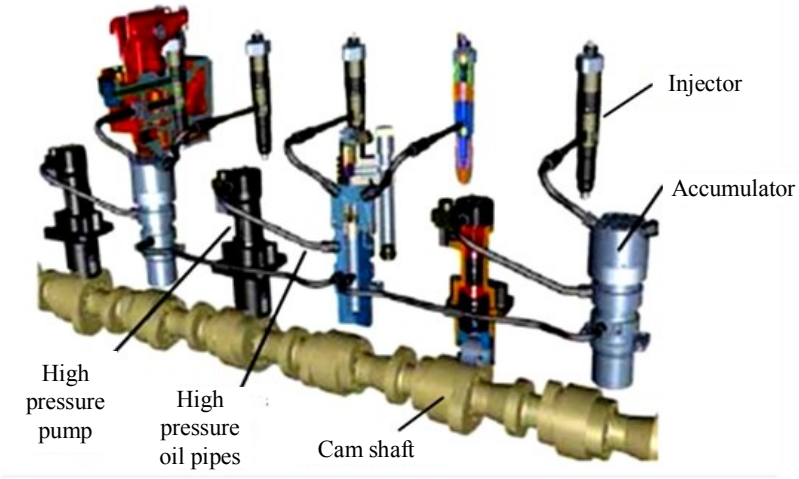

Figure 2-3 HPCR system for Wärtsilä W32CR diesel engine

2.2.2. The HPCR system for MAN 32/40 diesel engines

The HPCR system developed by MAN Diesel &Turbo [18] is shown in Figure 2-4 and Figure 2-5; they were designed for HFO operating conditions. They replaced one common rail of a traditional HPCR system by three common rails. Thus, a series of problems caused by the one common rail application for a large bore marine diesel engine is avoided, for instance,

1) The fuel temperature can range from 25°C to 150°C in the engine, which makes an obvious difference to the thermal expansion in the rail linear direction.

2) High material stresses are unavoidable because all the connections to each cylinder unit need to be drilled in a long rail.

3) Various lengths of common rails are required for engines with different numbers of cylinders.

4) Injection quantity deviations are caused by the position of the HP pump which connects with a rail at only one point.

Therefore, MAN HPCR systems cut a long rail into several rails, each of a suitable length. At least two HP pumps are needed for a six-cylinder engine. This kind of distribution offers flexibility for the HPCR system to be installed on engines with different cylinder numbers. Moreover, the HPCR system makes full use of precious available space in an engine.

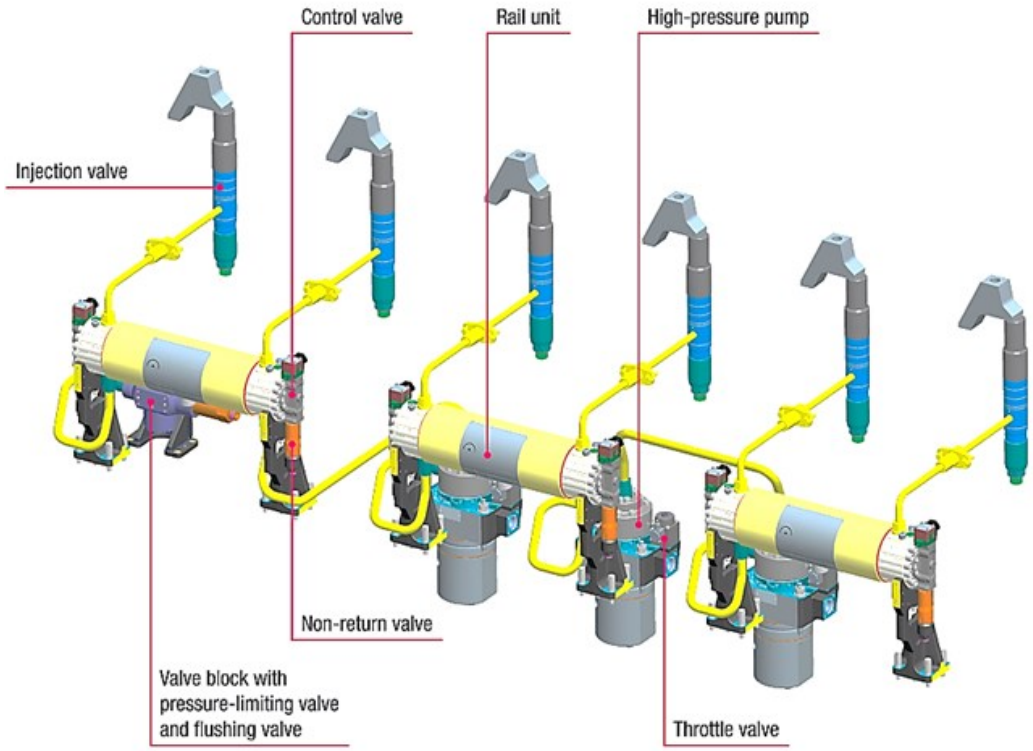

Figure 2-4 The HPCR system for MAN 32/40 diesel engines

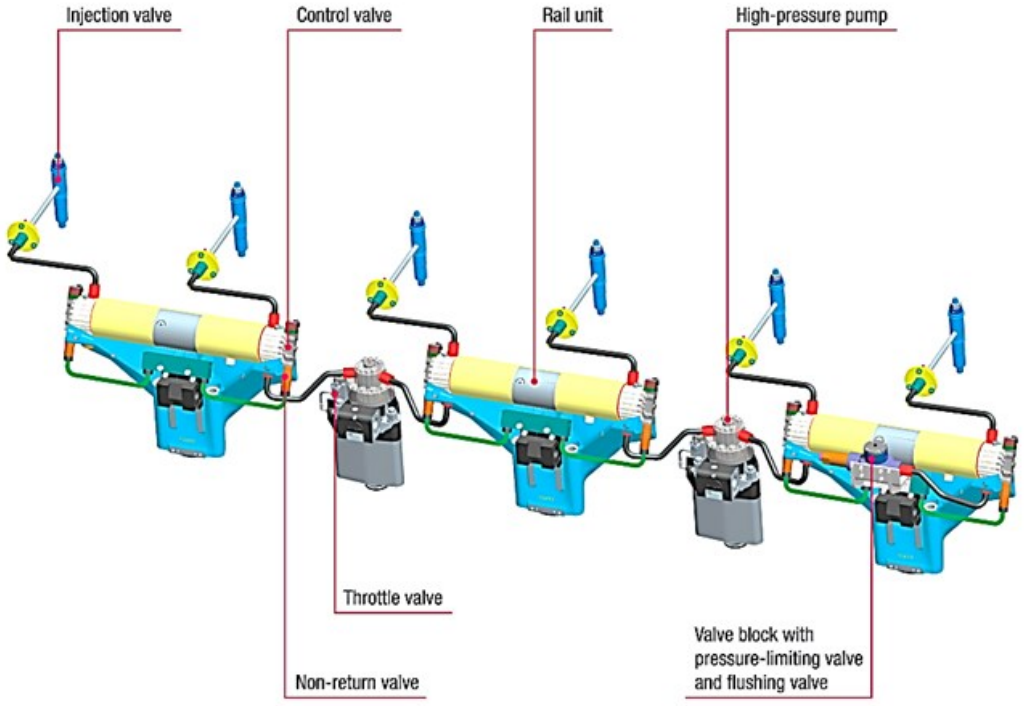

Figure 2-5 The HPCR system for MAN 48/60 diesel engines

2.2.3. A New type of HPCR system for Deutz diesel engines

Figure 2-6 shows an HPCR system developed by Deutz company for an 8-cylinder inline Deutz 628 engine [19]. The HPCR system has two rails, each serving four cylinders. For safety reasons, both rails have double walls. Fuel oil is fed in by an HP pump. The first and second generation HPCR systems have a shortcoming of static leakages in the needle valve and the control piston due to the huge pressure differences in these components. This kind of leakage is the main factor that affects the lifetime of an injector.

To conquer this, a new type HPCR system was developed, as shown in Figure 2-7. The new type HPCR system has no rail, which is replaced by connecting junctions. The volume of the traditional common rail is moved to the injector head. Each injector has an individual accumulator. These accumulators are connected by studs with connecting junctions. A great benefit of flexibility is achieved by using this type of distribution, because a smaller amount of place is required and no modification is needed to an existing engine.

At the same time, some other measurements should be taken to handle the transient pressure waves in high pressure oil tubes. The transient pressure waves result from the huge pressure drop during the injection process, since a small accumulator volume is adopted. In order to overcome this, the volume of the accumulator must be 20 to 50 times larger than the maximum quantity injected every stroke.

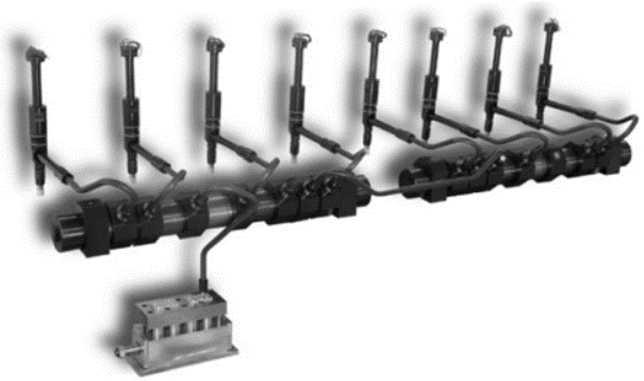

Figure 2-6 The new type of HPCR system for Deutz 628 diesel engines

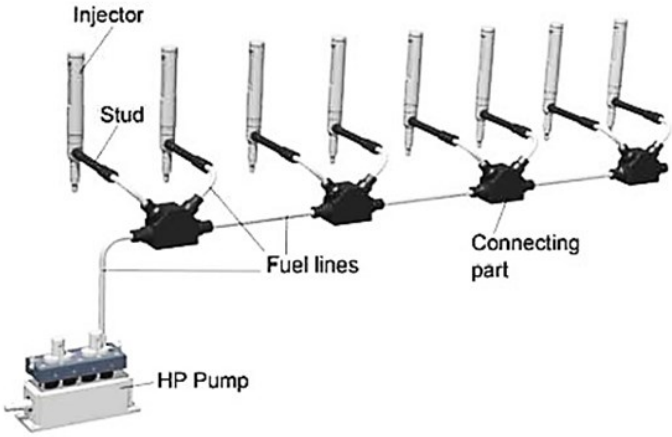

Figure 2-7 The new type of HPCR system for diesel engines with a power of 1 to 5 MW

2.2.4. The HPCR system for MTU series diesel engines

Figure 2-8 gives detailed information about the HPCR system for MTU-series diesel engines [20]. It can be clearly seen that the rails are only used for oil supplement, and that accumulators are placed at the head position of fuel injectors. Oil is fed by an in-line roller tappet designed high-pressure pump integrating with a metering unit. The metering unit is controlled by the ECU to maintain 1,800 bar rail pressure in the system. The whole system is designed with double walls to prevent potential leakages.

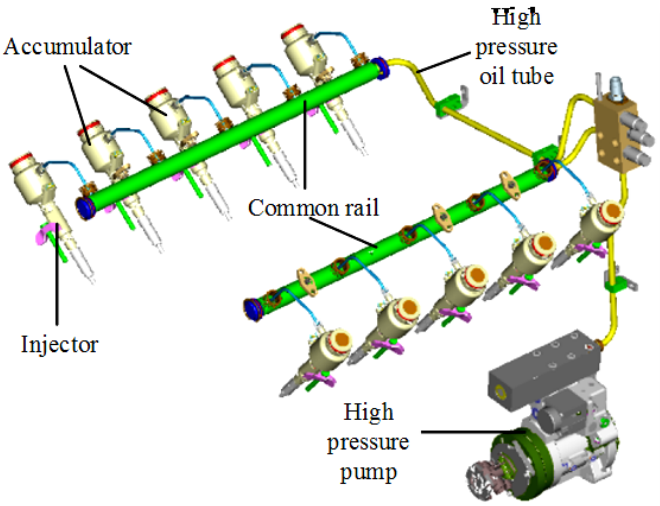

Figure 2-8 The HPCR system for MTU2000CR-series diesel engines

2.2.5. Comparisons of HPCR systems

The comparisons of HPCR systems form different engine manufactures were shown in Table 2-1. The HPCR systems with 1-3 rails are extensively adopted, while the Deutz new type HPCR system cancels the rail and move the volume of rail to the injector heads, which offers great flexibility for installation. The details of each HPCR systems refer to sections 2.2.1 to 2.2.4.

Table 2-1 Comparisons of HPCR systems

HPCR system	W32CR	MAN 32/40, 48/60	Deutz 628	Deutz new type	MTU 2000CR
Rail number	1	3	2	0	2
Pump number	3	2	1	1	1
Accumulator number	3	0	0	8	10
Studs	-	-	-	4	-

2.3. Electronic fuel injectors

The electronic fuel injector is an indispensable component of an HPCR system that greatly affects injection performance. Many companies can provide electronic fuel injectors, e.g. Denso, Bosch and Delphi. Although their fuel injectors vary in structure and appearance, they can mainly be divided into two types: solenoid and piezo. The solenoid fuel injectors are extensively used in engine applications. A typical solenoid fuel injector is discussed below.

2.3.1. Injector structure and working principle

A solenoid electronic fuel injector mainly comprises of armature institutions, solenoid valve coils, an injector body, a control chamber, fuel oil inlet and outlet

passages, a control piston, a needle valve and a nozzle (see Figure 2-9).

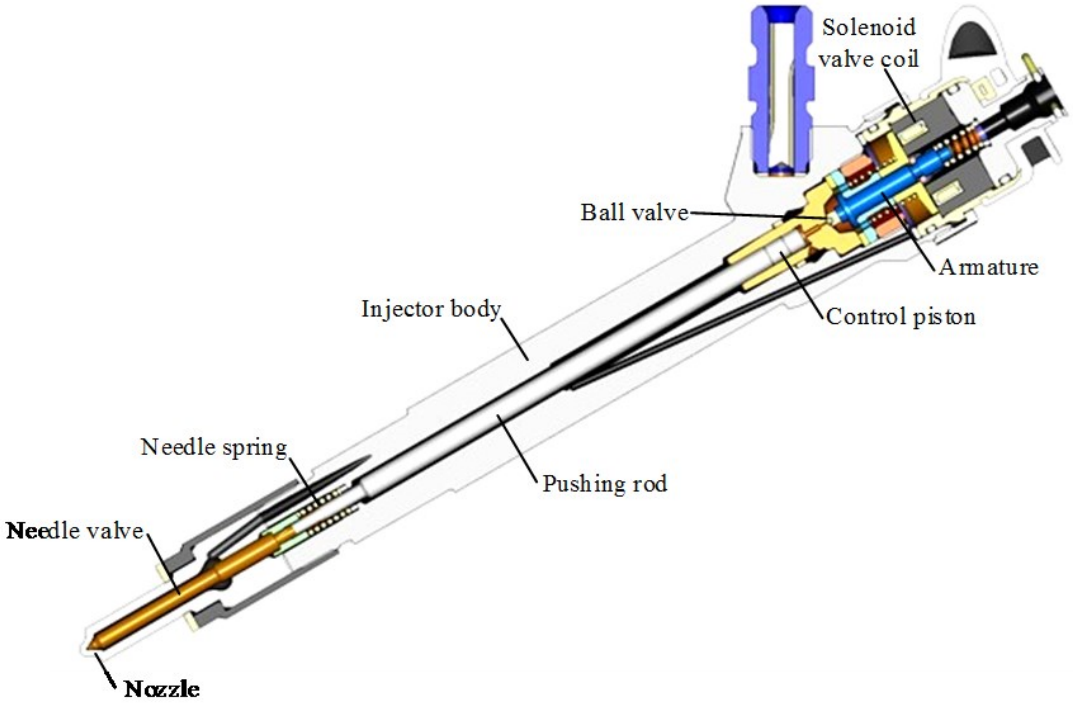

Figure 2-9 The composition of a typical solenoid electronic fuel injector

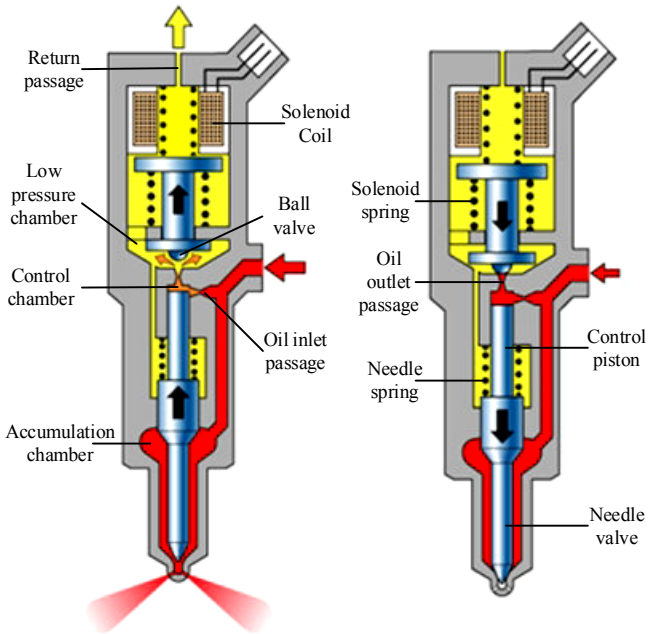

Figure 2-10 Working principle of a typical solenoid electronic fuel injector

Figure 2-10 gives the details of the working principle of a solenoid electronic fuel injector. The illustrations are as follows:

(1) In closing position

The control oil outlet passage is closed due to the preloaded spring force in the solenoid part. Equivalent rail pressure is presented in both the control chamber and the accumulation chamber. Since the area of the upper part of the control piston is bigger than that of the lower part of the needle valve, a net closing force presents, forcing the needle valve to keep at its seat. Thus, no injection occurs.

(2) Start of fuel oil injection [21]

When the solenoid valve is activated, the magnetic force overcomes the preloaded solenoid spring force. So, the ball valve is lifted up from its seat to open the control oil outlet passage. Therefore, oil flows into the low-pressure chamber and then continues to flow back to the fuel oil tank via the return passage. Due to the pressure drop in the control chamber, an upward net force pushes the needle valve to move upward to start fuel oil injection.

(3) End of fuel oil injection [22, 23]

When the solenoid valve is deactivated, the magnetic force vanishs and the ball valve returns to its seat thanks to the returning spring force. As a result, pressure in the control chamber re-gained to the rail pressure and the needle valve is pushed down to its seat to end the injection.

2.3.2. Literature review of electronic fuel injectors

Many studies have already been carried out on injectors' nozzle area, and on the influence of nozzle types and nozzle numbers on the internal flow and cavitation performance. For example, Molina et al. [24] investigated the inner nozzle flow and cavitation development of elliptical orifices. In that study, four nozzles with different major axis orientation and eccentricity values were compared with each other and also with the standard nozzle. Benajes et al. [25], Payri et al. [26], and Han et al. [27] focused on nozzle orifice types for electronic fuel injectors, comparisons were made between a cylindrical nozzle and a conical one. He et al. [28], Moon et al. [29] and

Salvador et al. [30] studied the effects of different nozzle hole arrangements and needle lift movements on the initial flow and cavitation development inside diesel injectors. However, to date, limited attention has been paid to the influence of the nozzle parameters on dynamic response, i.e. the valve opening delay and the valve closing delay.

Few studies were found in the literature which consider the impact of electronic fuel injector structural parameters on the dynamic response. Salvador et al. [31] compared the influences of a standard diesel fuel and biodiesels on the dynamic behaviour of a solenoid-operated injector. A change of the control oil outlet passage diameter from 0.246 mm to 0.27 mm was proposed to eliminate the needle lift and injection rate deviations between the two fuels. The deviations were caused by higher viscosity biodiesel fuel compared to regular diesel fuel. Results showed that the valve opening delay of the biodiesel fuel was reduced significantly under low injection pressure to match that of the standard diesel fuel. Additionally, some related studies are also worth mentioning. Wang et al. [32] investigated the influence of control valve parameters on flow and cavitation inside the control valve. Beccari et al. [33] predicted the mass injected by a gaseous fuel solenoid injector for spark ignition engines, with special attention paid to a gas injector and to the complex needle motion during the opening and closing phases. Cheng et al. [34] investigated the impact of drive strategies on the power loss and dynamic response of a solenoid injector. These studies focused on the dynamic response of the needle motion itself rather than on the valve opening delay and valve closing delay, and also left structural parameters such as the control piston diameter, control oil inlet passage diameter, control oil outlet passage diameter and the spring preload force at the needle valve out of their scope. Salvador et al. [35] investigated the impact of fuel temperature on injection dynamics, especially during the opening stage and closing stage. The delays were considered, but the structural parameters were still not included.

One-dimensional (1D) models have frequently been built and adopted in many studies to predict the performance of electronic fuel injectors. Payri et al. [36] used a

1D model of a solenoid-driven common rail ballistic injector to study the influences of the inlet fuel temperature on injection rate. Seykens et al. [37] built a 1D model of an injector to analyse the elasticity of the injector needle valve and nonlinearities caused by the impact of the needle valve when it returns to its seat. Rahim et al. [38] implemented a 1D model to study the effect of temperature on diesel engine performance. The detailed modelling of a solenoid fuel injector and a third-generation piezo injector were demonstrated by Payri et al. [39] and Salvador et al. [40] respectively.

2.4. CFD modelling and simulation

2.4.1. Introduction to the numerical simulation of an in-cylinder process

The combustion process of a diesel engine is very complicated with transients and multi-dimensional multi-phase processes. The research of new technologies like HPCR fuel oil injection systems, EGR and alternative fuels are all closely connected to the process of combustion. In this situation, many engine producers and research institutes are making great strides towards combustion simulation and visualisation.

For a long time, experimentation was the only method available for studying combustion; it had a high cost and was sometimes limited by circumstances and the accuracy of test devices. From the 1960s, great strides in the development of computer technologies, together with the breakthrough of computational fluid mechanics theory, computational heat transfer theory and chemical dynamics theory, an independent branch of simulating the diesel engine intake flow, injection, spray and combustion became prospective. This independent branch is also called the numerical simulation of diesel engine working process. In the simulation, theories and experiments are integrated, providing lots of advantages, e.g. adjusting flexible parameters, effective calculation period and low cost. Since then, the numeric simulation of the diesel engine working process has become an effective method for engine study and optimisation.

The combustion inside a cylinder is an extremely complex process where all kinds of fluid dynamics and chemical dynamics are interlaced. The unsteady boundary condition of each point cannot be determined, so a variety of physical and chemical models for describing combustion were built under different assumptions. The simulation history of combustion has gone from the zero-dimensional model, through the phenomenological model, to the multi-dimensional model [41].

(1) The zero-dimensional model

The basic assumption of the zero-dimensional model is that all the working media is uniformly distributed, i.e. thermal parameters and thermos-physical parameters are equal at all the calculation points. So, this model can be used to describe, evaluate and diagnose the energy transport occurring in the combustion process visually. But no emission behaviour can be predicted due to the combustion process only being described in general and in abstract terms, because none of parameters change with space.

(2) The phenomenological model [42]

With growing attention on emissions, emission prediction was brought into consideration for combustion simulations. Therefore, a phenomenological model was developed in the 1970s. It divides the combustion chamber into two or more regions according to the flame position and fuel oil injection distribution. In that model, the atomisation diffusion, droplet vaporisation, mixing and entrainment, flame spreading and the changing of combustion products of the burnt zone are all taken into consideration. Temperatures in the different zones are calculated and monitored as well. Different sub-processes can be highlighted with different engine types so that a more precise rate of heat release can be obtained. Although the phenomenological model is a great improvement over the zero-dimensional model, it is still limited in practical applications, because some sub-processes are built and tuned on phenomenon and experiences.

(3) Multi-dimensional model

The multi-dimensional model overcomes the drawbacks of the phenomenological model. It was built on the basic laws of fluid dynamics, thermodynamics and combustion chemistry. More specifically, it solves the mass conservation equation, momentum conservation equation and state equation in order to obtain the details of transient distribution of all species' velocity, temperature, pressure and component density, etc. These details are of great significance to get a better understanding of the combustion process and emission formation.

The multi-dimensional model for diesel engines includes three parts, they are air motion simulation of single-phase fluid mechanics; fuel oil injection, atomisation and mixing simulation by two-phase fluid dynamics and combustion simulation by combustion chemistry. So far, most of the multi-dimensional simulations are concentrated on fuel oil injection and combustion.

For the fuel oil injection, the main method is tracking and processing typical droplets by Lagrangian approach. Each group of droplets is assumed to have the same properties, i.e. motion, breakup, impingement and vaporisation are identical. The coupling of liquid phase with the gas phase is achieved by exchanging the source items of the mass, energy, momentum and turbulence equations. The turbulence diffusion, gathering, vaporisation, impingement and fuel droplet's breakup are described by different sub-models.

For the combustion, the ignition and combustion chemical process follow the chain transmission mechanism. The fuel density is decided by air-fuel mixing and changes with space and time. This process greatly affects chemical reaction dynamics. High anisotropy turbulence field interacts fiercely with laminar flow reaction. The appearance of the chemical and turbulence interaction in each combustion region is decided by a transient chemical reaction rate and flow variable's random impulse strength, i.e. the time scale ratio of chemical reaction and physical process.

2.4.2. CFD simulation software

This section introduces the software commonly used for combustion simulation. The most frequently used software for simulating combustion working processes are PHOENICS, EPISO, KIVA, FIRE, Star.CD, VERTIS, SCRYU, FLUENT, PowerFLOW, CFX-5, SPICE and FIDAP. They show some differences in physical or chemical models when describing the combustion process. None can be replaced by another since they show advantages and professional competence in different fields. For example, SCRYU [43] and PowerFLOW [44] are suitable for aerodynamic research due to their high accuracy calculations on peeling reattachment, cascade and eddy. KIVA codes are developed by Los Alamos National Laboratory. They are open source codes and can be modified by researchers to suit specific situations; hence, they are frequently used by researchers all around the world. FLUENT [45] is one of the most frequently used pieces of software in CFD simulation. Lots of models are included in FLUENT, e.g. steady and unsteady flow, laminar flow, turbulence flow, incompressible and compressible flow, heat and mass transfer, porous media, chemistry, particle trajectories and multiphase flow, free surface flow and phase change flow. Star-CD [46] software is extensively used for engine combustion simulation due to a shorter analysis and calculation time with a lower memory requirement. It consists of the main program, GUI (graphical user interface), and pre-and post-processor PROSTAR.

FIRE software from AVL was developed rapidly due to the powerful support of test data. It is extensively used in many higher education institutions. It consists of a pre-processor, a main program, modules and a post-processor. FIRE's pre-processor is a powerful and flexible tool for 3D grid generation, which offers high quality grids for problems with dynamic meshing. FIRE's solver contains a two-stage pressure correction technique which provides outstanding accuracy and stability. First or second order accuracy is provided by implicit time discretization schemes, while third order accuracy is offered by conservative and bounded differencing schemes. The software also includes lots of turbulence models, e.g. k-ζ-f and LES models. Moreover, physical and chemistry of advanced CFD applications are placed in each

module. The main program is parallelised for different engine applications. The post-processer is performed in both 2D and 3D formats, and it is of great help in simulation monitoring, visualisation, analysis and presentation of results [47].

2.4.3. Literature review on the engine combustion

The 1D, 2D and 3D engine combustion models and the frequently used software were introduced in the previous sections, the literature review on the engine combustion.

A lot of meaningful work has been done on this subject, Taghavifar et al. [48] studied the effects of bowl movements and radius on mixture formation in terms of homogeneity factor, combustion initiation and emissions for a 1.8 L Ford diesel engine. They pointed out that the mixture uniformity increased as the bowl displacement toward the cylinder wall, but got penalty of a rise of combustion delay which substantially reduces the effective in-cylinder pressure. They also found that smaller bowl size contributes to better squish and vortex formation in the chamber, although with lesser spray penetration and flame quenching. Park [49] used a micro-genetic algorithm coupling with a KIVA code to optimise combustion chamber geometries and engine operating conditions for an engine fuelled with dimethyl ether. He found the combustion and emission characteristics were significantly different from that of conventional diesel engines. Mobasheri et al. [50] investigated the influence of a re-entrant combustion chamber geometry on mixture forming, combustion and performance for a high-speed direct injection diesel engine. Thirteen combustion chambers with different shapes were designed by adjusting piston parameters, i.e. bowl depth, bowl width, piston bottom surface and the lip area. Results indicated that small bowl diameter is the main reason for high soot emissions, and a slightly larger bowl diameter is where the optimal operating point locates.

Recently, the ever-changing calculation ability of computers brings the computational fluid dynamics to a more sophisticated and precise level. Some algorithms were frequently used in engine optimisation domain. High efficiency was

achieved in the study of a huge amount of optimisation cases. Researchers of references [51-52] developed a KIVA code with μGA, MOGA or NSGA II to study the matching of a variety of engine parameters, from small bore, high-speed direct injection engines to heavy-duty large bore slow-speed diesel engines. This huge amount of optimisation work was done owing to the effective optimisation algorithms. Taghavifar et al. [53] used a DOE method incorporating with a Sobol sequence to scan through various design points of a 1.8 L Ford diesel engine, aimed to seek a reduction of NO_x and an enhancement of the spraying performance. He found the optimal case has a lower injection angle and a smaller bowl volume. Jeong et al. [54] used a hybrid evolutionary algorithm by coupling a GA and a PSO for the optimisation of a diesel combustion chamber. Results indicated that hybrid evolutionary algorithm shows better diversity and convergence. Chen et al. [55] used an orthogonal design method to optimise the match of injection-related parameters with three combustion chamber geometries for an 8.9L Cummins diesel engine. Then, NLPQL algorithm was adopted for a more detailed study on combustion chamber geometries.

2.5. Algorithms for solving and analysing multi-optimisation problems

2.5.1. DOE method

DOE is a systematic method for building a relationship between the input factors and output factors of a process. A great deal of information can be obtained through a reduced number of DOE simulations; therefore, it is effective to investigate the influences of individual variables on the response. In DOE, “factors” refer to design variables, and “level” refers to a specific value assigned to a factor. A DOE method creates a number of design points, which is a variation in the selected model’s parameters [56].

The LH is one of the most commonly used DOE methods. In it, the design space of each factor or design parameter is divided into n uniform levels. On each level of

every factor, only one design point is placed. For each factor, permutations of the *n* levels are possible. The design matrix of the LH consists of one column for each factor, which is determined by a randomly chosen permutation of the n levels. For a row of the design matrix, n^k combinations are possible and have an equal chance of occurring. As the matrix is generated randomly, a correlation between the columns may exist [57].

2.5.2. Genetic algorithm

(1) Multi-objective genetic algorithm

The genetic algorithm (GA) is frequently used in solving multi-objective problems. The GA optimisation based on the idea of the natural selection which obeys the law of 'survival of the fittest'. The GA works with a number of populations, which stand for a group of solutions for a given problem. A fitness is assigned to each individual according to objectives. An individual with a higher fitness has a higher probability of getting the chance of survival and reproduction. Thus, a new generation of individuals will be produced and it inherent some features from their parents. Crossover of the GA drives the population toward a local minimum/maximum while mutation of the GA increases the diversity of individuals. Since the less fit individuals tend to die off due to the reason that they have less chance for reproduction. At the same time, the new generation is likely to have a higher fitness since they possessed good characteristics from their parents. GA's process continually improves a population's average fitness level effectively, thus, a series of optimums can be searched out eventually[58-61]. MOGA refers to the modified version of the classic GA which can find a set of multiple non-dominant solutions in a single run [62].

(2) NSGA-II

NSGA-II (non-dominated sorting genetic algorithm II), one of the genetic algorithms, proposed by Deb et al. [63], was proved to have better performance of finding a diverse set of solutions and converging near the true Pareto front. The NSGA-II

algorithm employs an elite-preserving strategy and an explicit diversity-preserving mechanism. According to objectives, elitism is given to the corresponding designs. Designs with a higher elitism have priority to be selected. If two designs have the same elitism, the one with less crowding distance (proximity to other Pareto solutions) is assigned with a higher priority.

2.5.3. NLPQL algorithm

NLPQL was developed by Klaus Schittkowski [64] for solving the nonlinear programming problem.

Min $f(\mathrm{x})$

$$\begin{gathered} g_j = 0, j = 1,...,m_e \\ x \in R^n : g_j(x) \geq 0, j = m_e + 1,...,m \\ x_Q \leq x \leq x_u \end{gathered} \tag{2.1}$$

Where, x is the n-dimensional parameter vector; x_Q and x_u are the lower boundary and upper boundary of x; $f(\mathrm{x})$ is the problem function; $g_j(x)$ are the constraints of the problem.

The optimisation method generates a sequence of quadratic programming subproblems which are to be solved successively. The method is therefore known as the SQP method. It assumes that objective functions and constraints are continuously differentiable on the set $E = \{x \in \Re^n : x_Q \leq x \leq x_u\}$. Note that the functions f and $g_j, j = 1,...,m$ need to be defined only in the set *E*, since the iterations computed by the algorithm will never violate the lower and upper boundaries.

2.5.4. Pareto optimality

Pareto Optimality indicates a condition in which economic efficiency reaches a state

where no one can be made better off by making someone else worse off. It is commonly used in optimisation problems with two objectives, as shown in Figure 2-11, which illustrates the definition of the Pareto optimum. If the aim is to minimise the both objectives I and II, case A-D can be considered as Pareto optimal cases due to the fact that none of them are out-performed by other cases. Terminology dominance is frequently used here to describe the Pareto optimal designs. All Pareto optimal designs are dominant designs. These dominant designs can be grouped together to form Pareto front. The dominated designs mean that at least one of their objectives is worse than other designs, i.e., designs E-H.

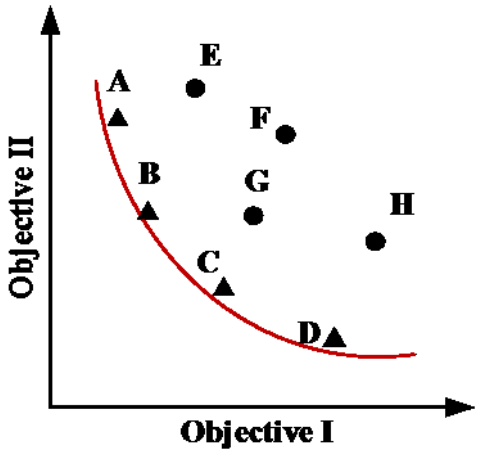

Figure 2-11 Definition of Pareto optimum

The Pareto optimality can be defined as: For all designs $\vec{x}$ and the corresponding N objectives $f_k(\vec{x})$, where, k= 1, 2, …, N, the Pareto design $\vec{x}$ is defined that for an arbitrary design j, there exists at least one objective, k, which meets the condition $f_k(\vec{x}_j) \prec f_k(\vec{x})$.

2.5.5. Response surface method

RSM was frequently used as the tool for analysing the sensitivity of design parameters on the objectives [65]. It uses an approximation model to analyse the data generated by Design of Experiments (DOE). Several functions can be used for

building approximation models, such as polynomials, smoothing spline ANOVA, NN [66-68], *k*-nearest [69], etc. Comparisons were made in literature that *k*-nearest method was suggested for dealing with large data sets and the NN was recommended for having a better accuracy and performance in the prediction process [70-71].

2.6. Hardware-In-Loop (HIL) systems in the engine domain

The first and earliest application of a HIL system can be dated back to 1936, where they simply tried to simulate the devices with a fixed cockpit 'linktrainer'. Then, the cockpit moved according to the aircraft's motion. In the HIL system, the cockpit and the pilot are real, while the motions are virtual and simulated by analogue tube controllers and analogue motion simulations. The HIL system is aimed at training pilots [72].

Lots of new technologies and state-of-the-art products (like DSP, FPGA micro controllers, high performance computers with sophisticated models) are used in HIL systems. Their basic rules are that control targets or some actuators which are inconvenient to realise are simulated by models. So, the HIL system is also regarded as a semi-physical simulation technology. It is the combination of the physical and virtual prototyping technologies.

The engine industry is one of the most competitive fields which face the challenges of ever increasing complexity and more stringent emission regulations. However, these challenges drive the designer trying to shorten the development period from the engine design to production. For this reason, an increasing number of HIL systems are being introduced. Wu et al. conducted a series of FRM/Simulink co-simulations and HIL tests to verify a GT-Power fast run model [73]. Yang et al. used an HIL to validate a control-oriented model for the SIHCCI hybrid combustion model [74]. Saad et.al applied double Wiebe functions on an HIL system to simulate the heat release rate, temperature, and pressure during the combustion process. The HIL application showed a good agreement with 57 engine tests in terms of ignition delays and cylinder pressures [75]. Schuette et.al provides a condensed technical overview

of the state-of-the-art HIL test system components and structures for engine control systems, in which ECUs, sensors, actuators and interfaces are included and described in detail [76].

The main advantages of an HIL system are as follows [77]:

- Control and regulation functions and codes can be verified in advance, even before a test prototype has been produced. Hence, control programs can reach a high degree of maturity to fit the development later on.

- The simultaneous development of the ECU and vehicle can be achieved by HIL simulation, which can cut down the development period.

- Expensive devices or hazardous situations can partly or fully be replaced by software models in computers or other devices.

- Extreme conditions that may cause damage to real devices can be simulated and tested repeatedly.

- Experiments performed on the HIL system can be reproduced precisely and repeated as needed.

A HIL system was built according to a medium-speed marine diesel engine for injectors testing (in this study) and injection rate control strategies development.

Chapter 3. Investigation of the Type-I fuel injector

The previous section presented that few studies have been carried out on how the control piston diameter (CPD), control oil inlet passage diameter (IPD) and control oil outlet passage diameter (OPD) affects the injection characteristics and injector dynamic response. However, the injection characteristics and injector dynamic response have significant effects on injection quality and combustion. Therefore, in this chapter, the effects of CPD, IPD and OPD on injection characteristics and injector dynamic response are investigated by using a parametric study and a multi-objective study. In the multi-objective study, a novel optimisation routine is proposed and later proved to be an effective solution. Firstly, a complete and detailed 1D Type-I electronic fuel injector model was built in AMESim [78] and was validated by using injection quantity and injection rate data. Then, an optimisation routine was built in modeFRONTIER [79] software, where the 1D fuel injector model was included and a MOGA was applied for the optimisation. In addition, the interactions between these design parameters were also studied and an optimum with the best trade-off between the valve opening delay and valve closing delay was singled out. The detailed information is reported below.

3.1. Modelling of Type-I fuel injector

In this model, some assumptions are made that all the variations are isothermal, so, the fuel temperature was assumed to be constant along the injector and equal to the one at the injector inlet. And the fuel property was considered to be constant [80]. Additionally, a constant pressure source was adopted here to simulate the pressure from the high-pressure pump, thus neglecting the pressure fluctuations caused by the periodical oil supply from the high-pressure pump. Moreover, the pressure wave propagation was not considered in the model. The details of the modelling of the Type-I fuel injector refers to Appendix A.

3.2. Simulation verification

The 1D model was validated under three different rail pressures, i.e., 30 MPa, 80 MPa and 130 MPa. Under each pressure, four initialise times of injection were applied, 0.24 ms, 0.5 ms, 1 ms and 2 ms. Injection rate comparisons are shown in Figure 3-1 to Figure 3-3 and injection mass comparisons are shown in Figure 3-4. The fuel properties used for simulation are shown in

Table 3-1. Figure 3-1 to Figure 3-3 indicate the simulation injection rate are approximately the same with the experimental one, especially when the incentive time is larger than 1 ms. The simulation injection rates show an identical tendency at the end of needle valve closing are much lower than the experimental results. This can be attributed to the elastic differences in the material between an injector model and an authentic fuel injector. The authentic fuel injector has an elastic body. Thus, when the injector is deactivated, the needle valve moves back to its original place and hits on the seat. The needle valve bounces back several times before it closes completely, which results in a small fuel injection rate in the experimental results. In Figure 3-4，it can be seen that there is a small difference between the simulation results and experimental results, which becomes larger with an increase in the rail pressure. This is because a high rail pressure leads to a larger flow speed. When the cross-section area of the nozzle orifice is the same, a larger flow speed results in a larger injection quantity. However, these tiny differences in the injection rate and injection quantity can hardly have an impact on the injector dynamic response (opening/closing delay and opening/closing time), which are mainly decided by the injection rate slopes. And Figure 3-1 to Figure 3-3 indicate that the injection rate slopes in all the sub-figures present a highly accurate reproduction of the experimental injection rate. Therefore, the 1D Type-I fuel injector model would able to be used to predict the performance of the authentic fuel injector with high accuracy and precision.

Table 3-1 Physical and chemical properties of Repsol CEC RF-06-99 fuel [**Error! Bookmark not defined.**]

Properties	Value	Uncertainty
Density at 15 °C, kg/m^3	843	±0.2
Viscosity at 40 °C, mm^2/s	2.847	±0.42
Average fuel molecular composition	$C_{13}H_{28}$	

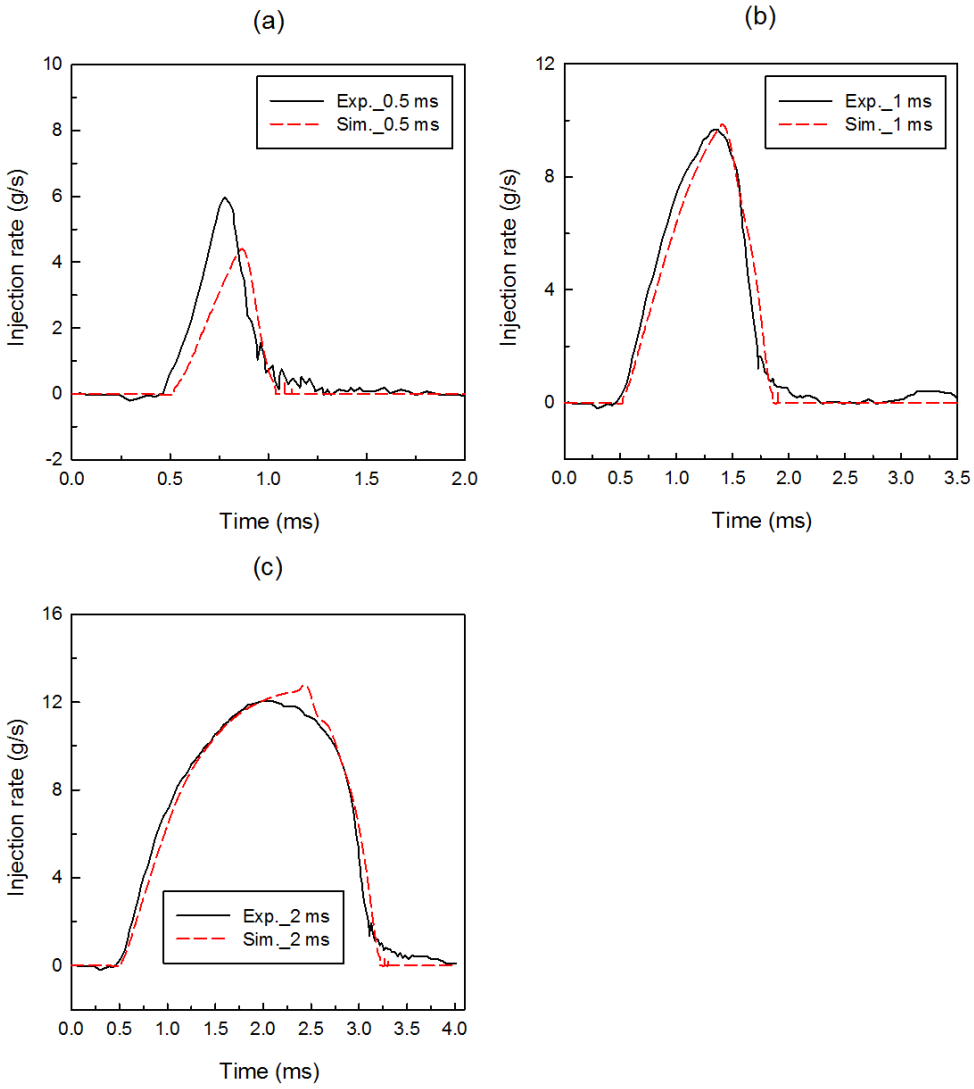

Figure 3-1 Injection rate comparisons at 30 MPa rail pressure

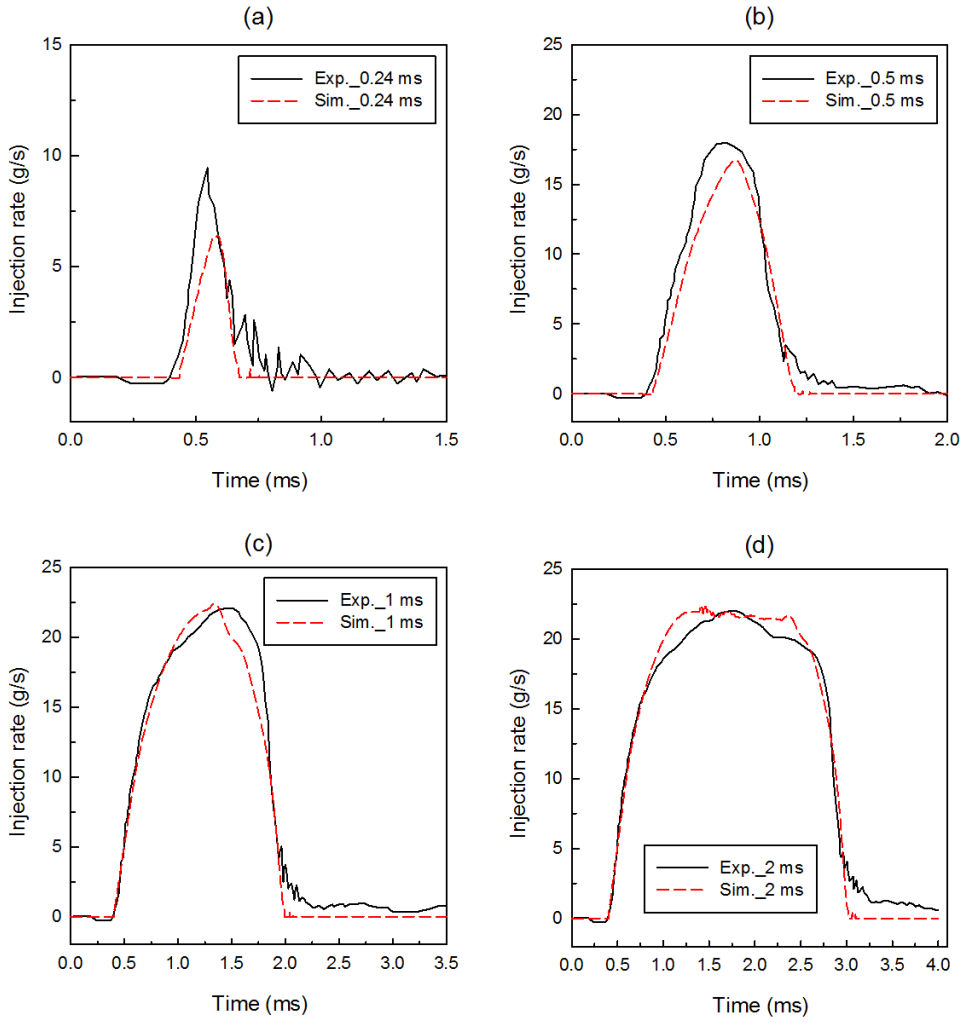

Figure 3-2 Injection rate comparisons of simulation and experimental data at 80 MPa rail pressure

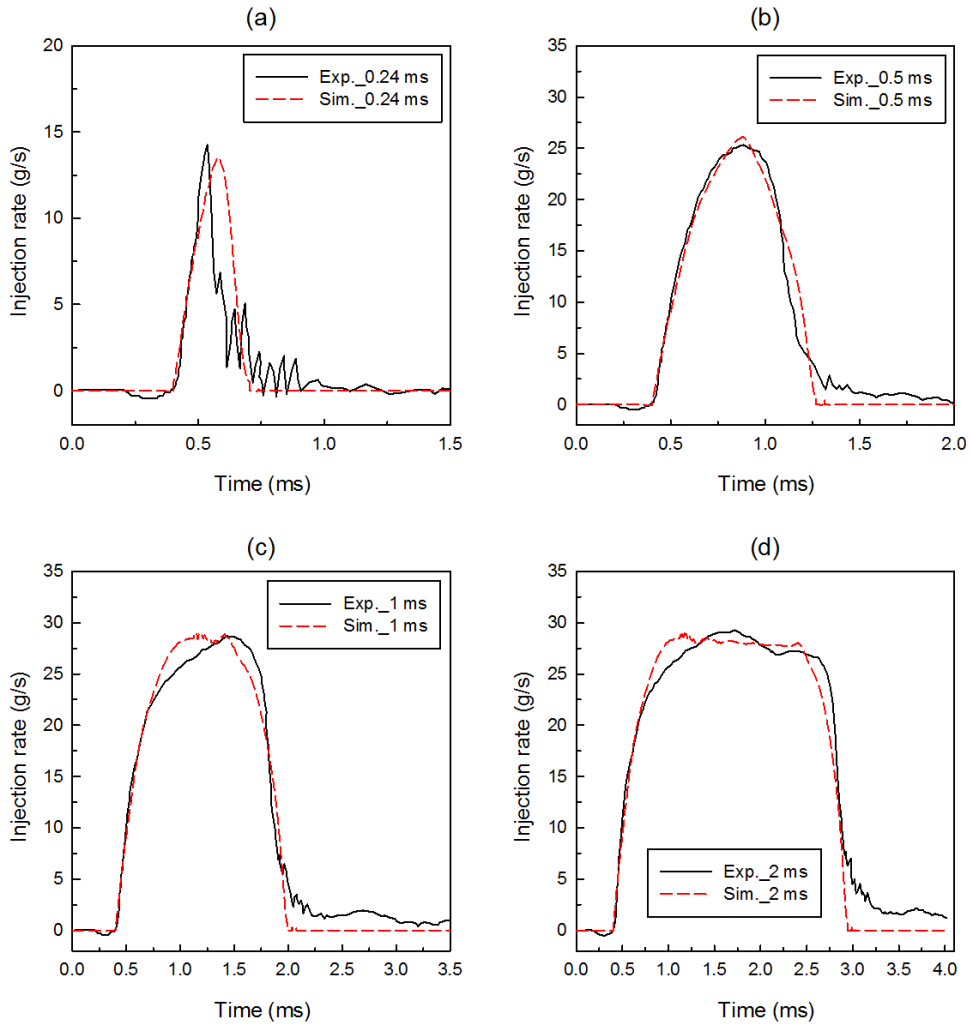

Figure 3-3 Injection rate comparisons of simulation and experimental data at 130 MPa rail pressure

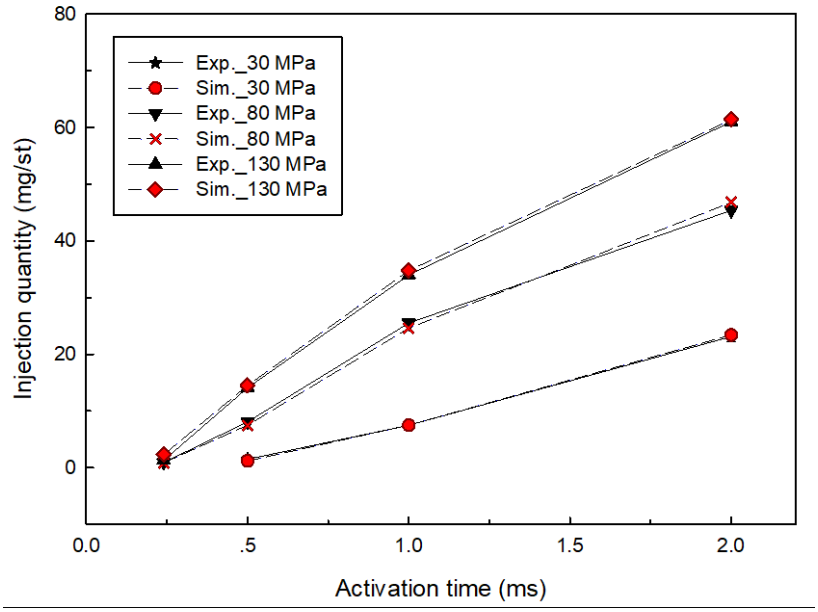

Figure 3-4 Injection mass comparisons of simulation and experimental data at each rail pressure

3.3. Definition of the dynamic response

As was stated above, the dynamic response affects the shape and the delay of the fuel oil injection rate; therefore, an effective dynamic response provides a great ease on achieving a precise injection and offers flexibility for the control of the multi-injection. The injector dynamic response includes mass flow rate, injection delays and injection rate slopes. In this study, only the valve opening delay and the valve closing delay were selected. Small valve opening and valve closing delays means a faster and better injection response. The definitions of the dynamic response are shown in Figure 3-5, where the valve opening delay is defined as $\Delta T1$, which is the period of time between t1 and T2, and the valve closing delay is defined to $\Delta T3$, which is the period of time between t3 and T4. In other words, $\Delta T1=T2-t1$ and $\Delta T3=T4-t3$.

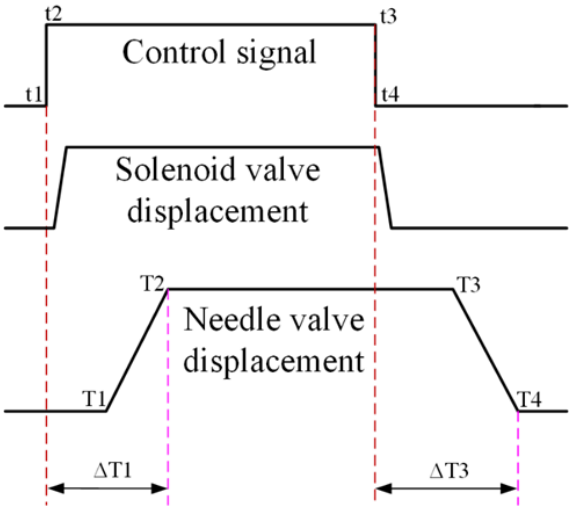

t1: the control signal is initiated; t2: the control signal has reaches its maximum amplitude; t3: the control signal is de-activated; t4: the control signal has fully closed; T1: the needle valve starts to open; T2: the needle valve has reached its maximum displacement; T3: the needle valve begins to close; T4: the needle valve has fully closed.

Figure 3-5 Definition of the injector dynamic response

3.4. Parametric study

In the parametric study, the design parameters including control piston diameter (Rod), control oil inlet passage diameter (OZ), control oil outlet passage diameter (OA), were varied at five values and only one parameter was changed at a time. The lower and upper boundaries were selected basing on the trial simulation results.

3.4.1. Control piston diameter

The control piston diameter was set to 3.7 mm, 3.9 mm, 4.1 mm, 4.3 mm and 4.5 mm respectively. The derived results are shown in Figure 3-6 and Figure 3-8 to Figure 3-10.

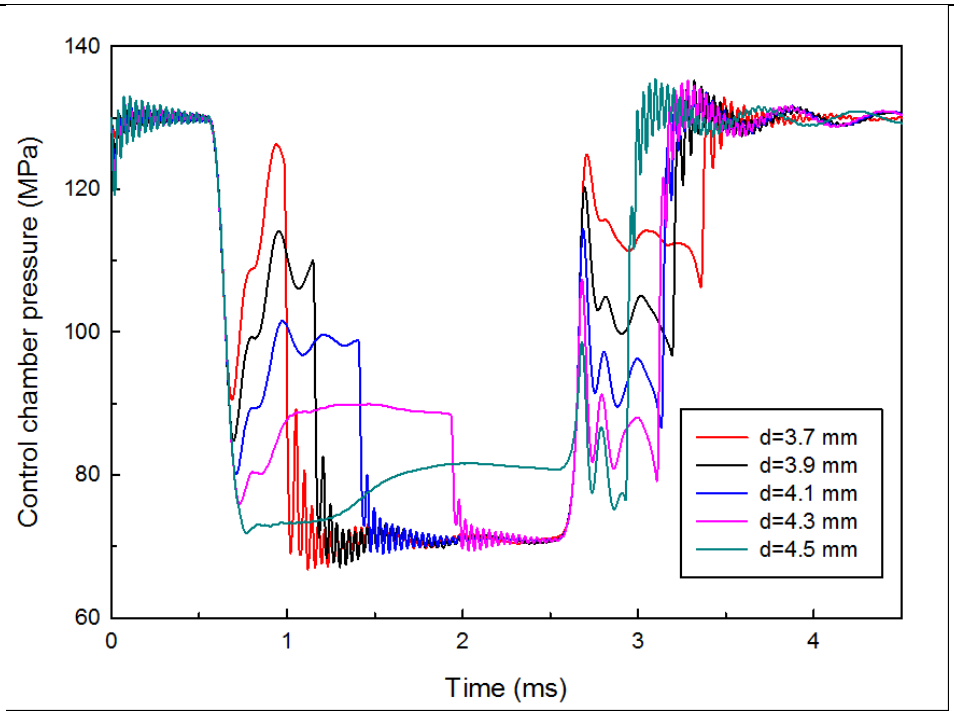

Figure 3-6 Impact of the control piston diameter on the control chamber pressure

The theoretical explanation about the pressure fluctuations shown in Figure 3-6 is presented by considering Figure 3-7: when an electronic fuel injector is deactivated, the pressure in the control chamber is kept the same as the rail pressure until the electronic fuel injector is energised; the control oil discharges via the oil outlet passage which leads to a pressure drop in the control chamber. When pressure in the control chamber decreases to the pressure critical for the needle valve opening, the needle valve starts to lift up. During this process, pressure in the control chamber increases slightly. When the needle valve opens to its maximum lift position, the pressure in the control chamber drops again to a steadier platform. In contrast, when the electronic fuel injector is deactivated, the pressure in the control chamber increases to push needle valve to close; during this time, the pressure in the control chamber increases slightly and then restores the rail pressure once the needle valve is completely closed.

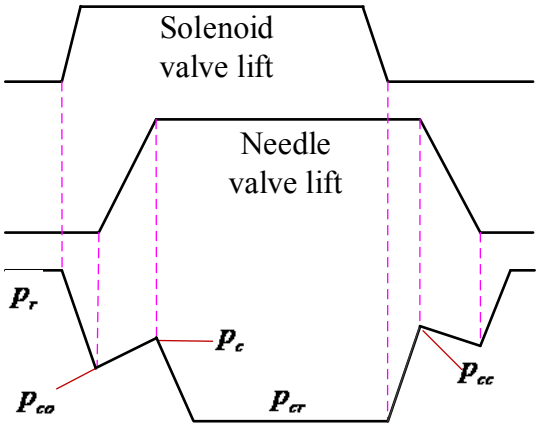

Figure 3-7 Pressure fluctuations in control chamber

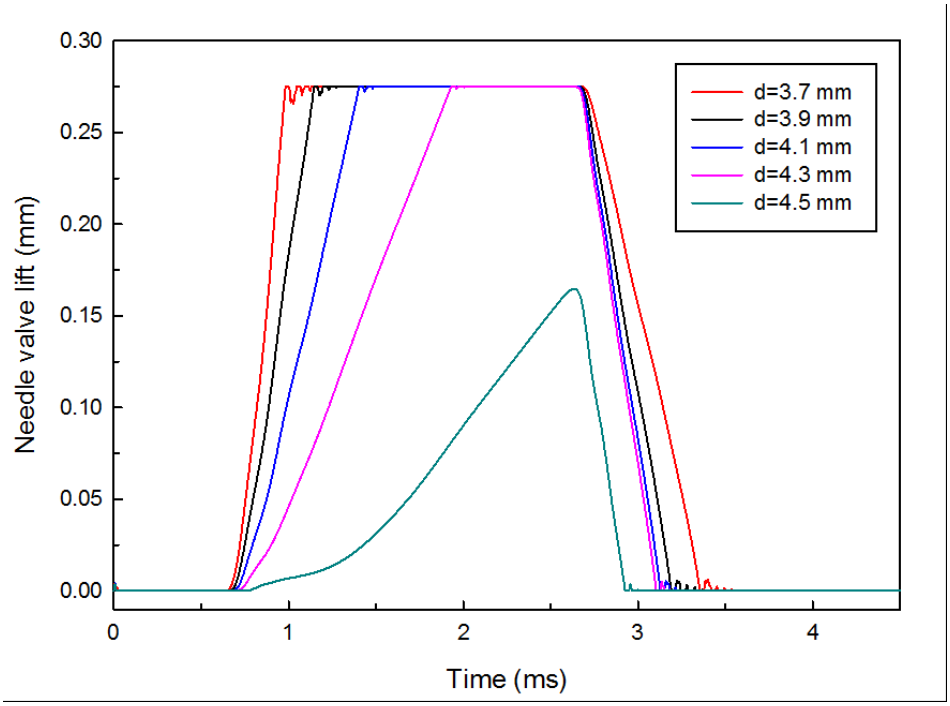

Figure 3-8 Impact of the control piston diameter on the needle valve lift

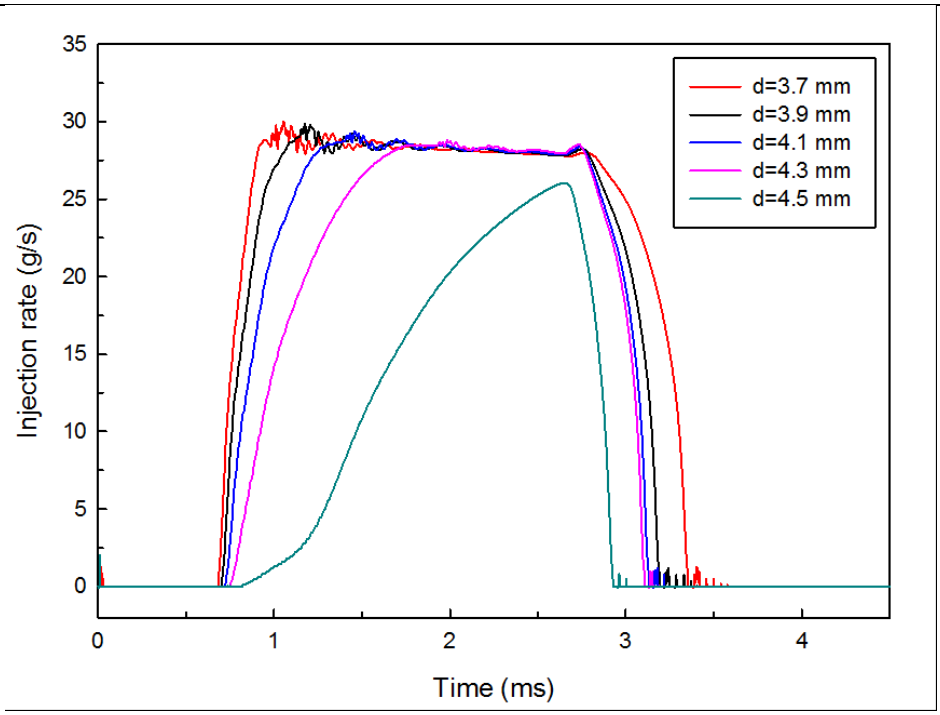

Figure 3-9 Impact of the control piston diameter on the injection rate

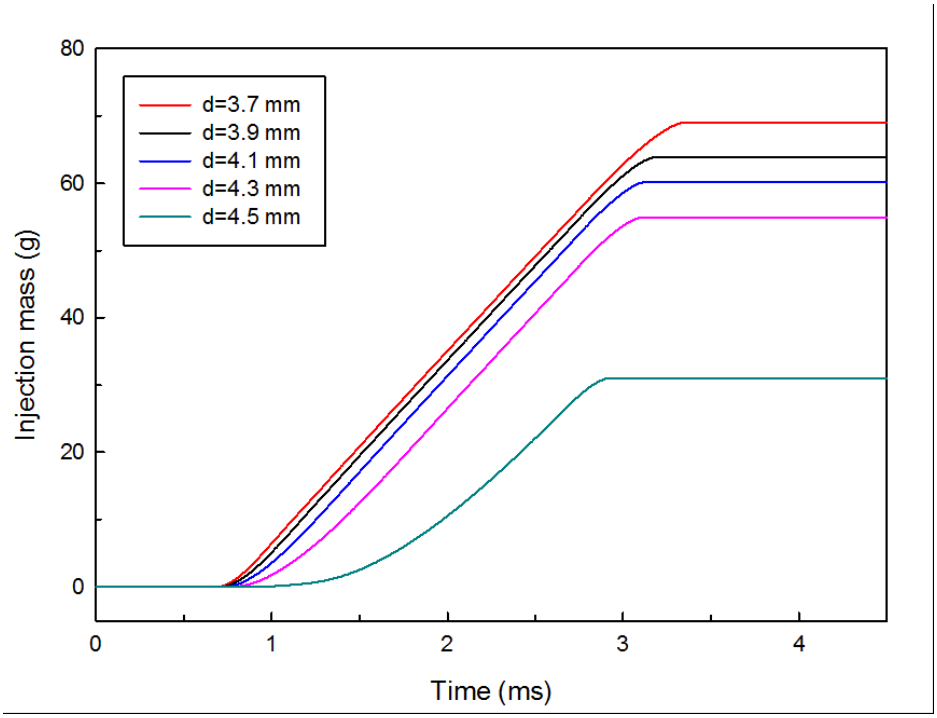

Figure 3-10 Impact of the control piston diameter on the injection mass

Figure 3-6 to Figure 3-10 indicate that with an increase in the CPD (control piston diameter), the needle valve opening delay increases, and the valve closing delay deceases (see Figure 3-8), which leads to a decrease in total fuel oil injection quantity (see Figure 3-10) and smaller pressure fluctuations in the control chamber (see Figure 3-6). The main reasons are summarised below.

The variation of CPD changes the upper surface area of the control piston. Thus, a larger CPD means a larger upper surface area of the control piston, and a higher force is exerted on it. Since the pressure on the lower part of the needle valve remains the same, a smaller net force is obtained when the solenoid valve is activated. This net force pushes the needle valve upwards to start the fuel oil injection. In this condition, a smaller net force slows the needle valve opening velocity and extends the valve opening delay, as shown in Figure 3-8. When the solenoid valve is deactivated, the control chamber regains the rail pressure and a larger opposite net force pushes the needle valve quickly downwards, which reduces the valve closing delay.

3.4.2. Control oil inlet passage diameter

The control oil inlet passage diameter was changed considering the following five values, 0.15 mm, 0.17 mm, 0.19 mm, 0.21 mm and 0.23 mm, respectively. The derived results are shown in Figure 3-11 to Figure 3-14.

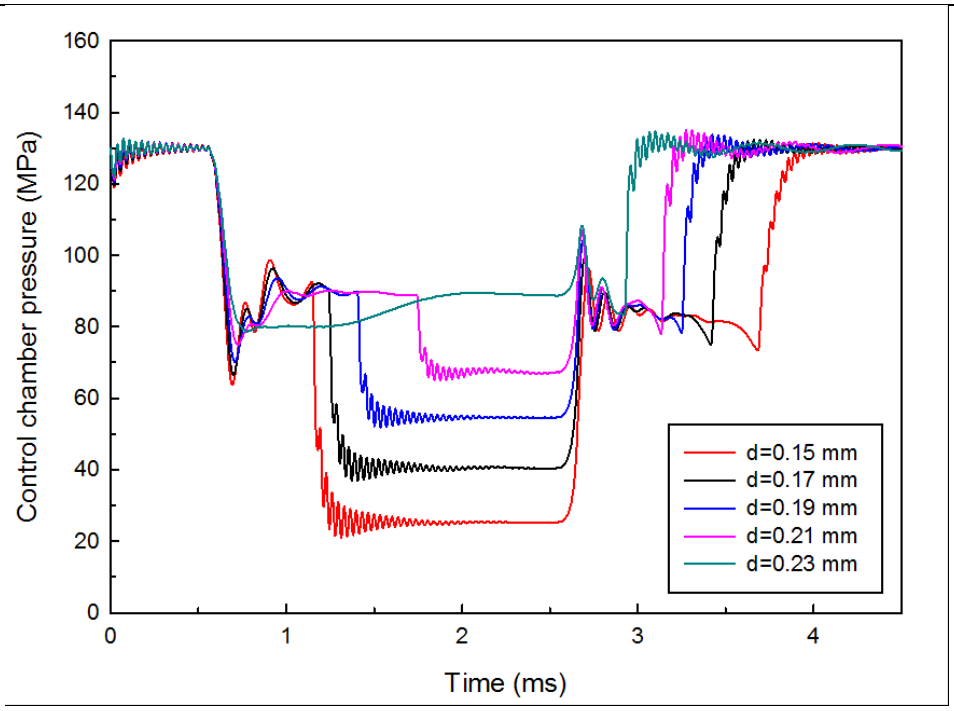

Figure 3-11 Impact of the control oil inlet passage diameter on the control chamber pressure

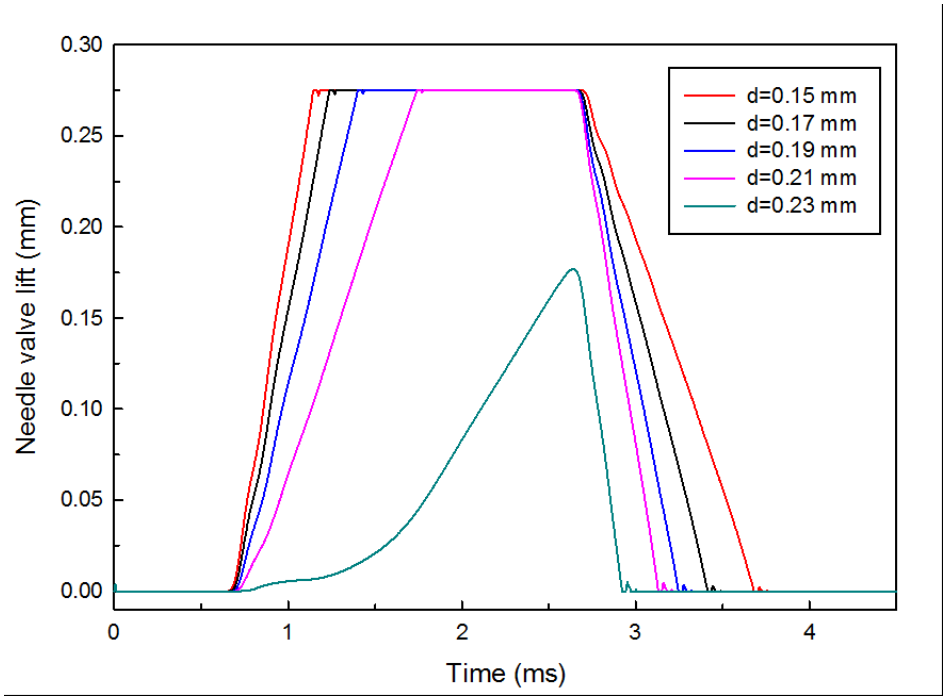

Figure 3-12 Impact of the control oil inlet passage diameter on the needle valve lift

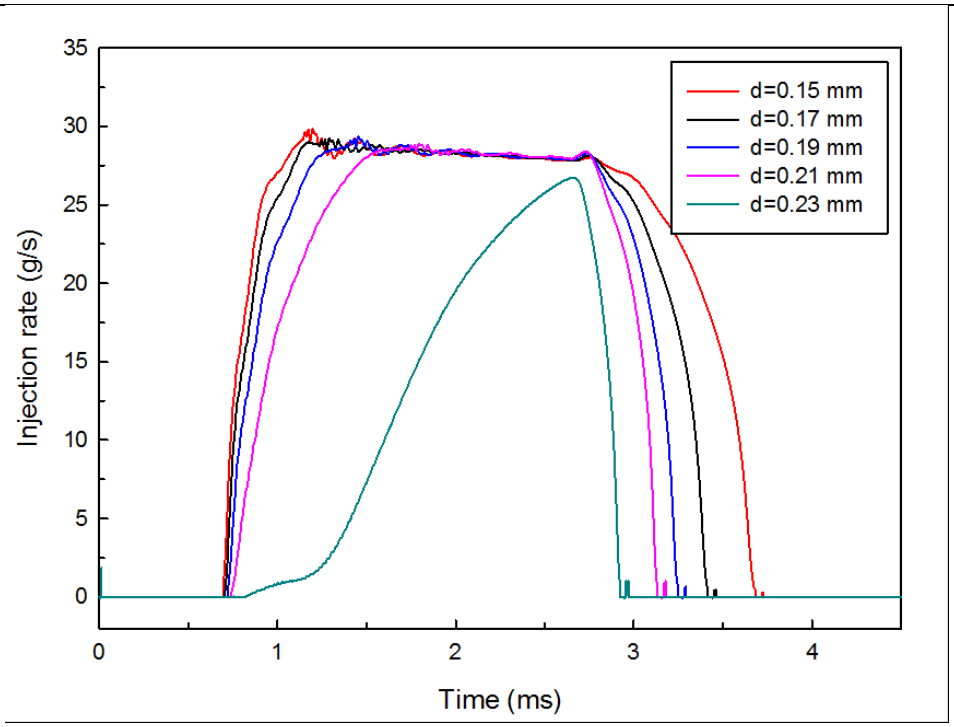

Figure 3-13 Impact of the control oil inlet passage diameter on the injection rate

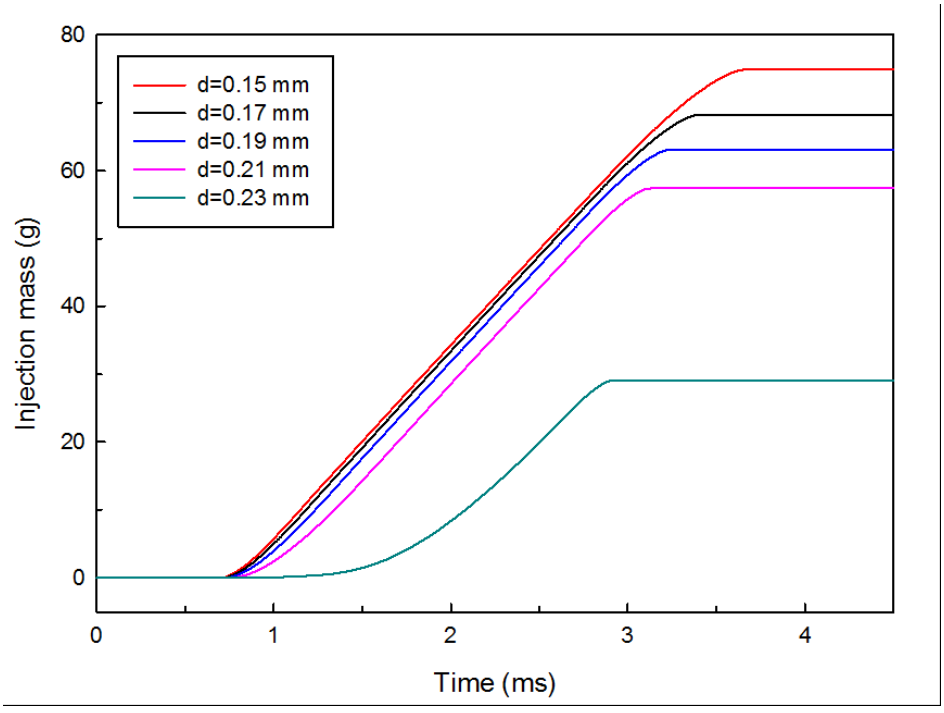

Figure 3-14 Impact of the control oil inlet passage diameter on the injection mass

The results above demonstrate that the IPD has a huge impact on fuel oil injection characteristics. With the increase in the IPD, the fuel oil injection quantity (as shown in Figure 3-14) decreases significantly, and the needle valve opening delay becomes greater. In general, the larger the IPD is, the slower needle valve opening action, and the faster the closing action, as shown in Figure 3-12. This is because the change of IPD has an effect on the oil charge rate. A larger IPD results in a greater oil charge rate when the solenoid valve is activated. Since the oil discharge rate in the oil outlet passage remains the same, the pressure in the control chamber drops slower than with a small IPD, which slows down the needle valve velocity at the opening stage and speeds up the needle valve closing movement at the closing stage. Thus, a larger IPD leads to a larger valve opening delay and a smaller valve closing delay and vice versa.

Additionally, a larger IPD (oil inlet passage diameter) results in a smaller control chamber pressure fluctuation. This is due to the greater IPD offering a larger oil charge rate and thus supplementing the control oil in time to alleviate the fluctuation caused by the needle valve opening and injection.

3.4.3. Control oil outlet passage diameter

The control oil outlet passage diameter was changed to 0.23 mm, 0.265 mm, 0.305 mm, 0.345 mm and 0.385 mm, respectively. The derived results are shown in Figure 3-15 to Figure 3-18.

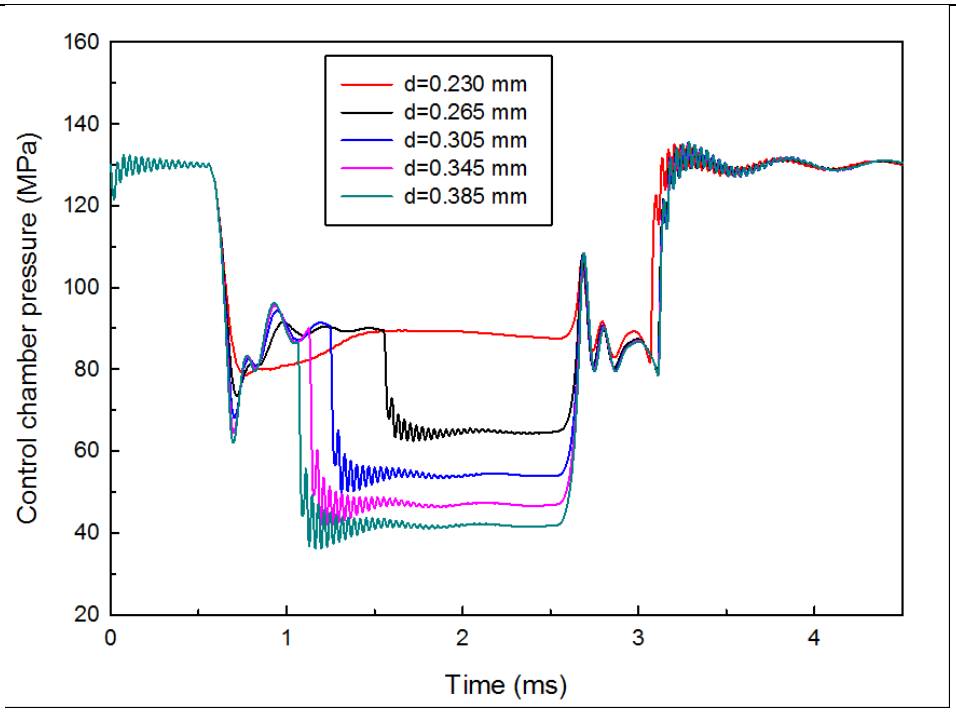

Figure 3-15 Impact of the control oil outlet passage diameter on the control chamber pressure

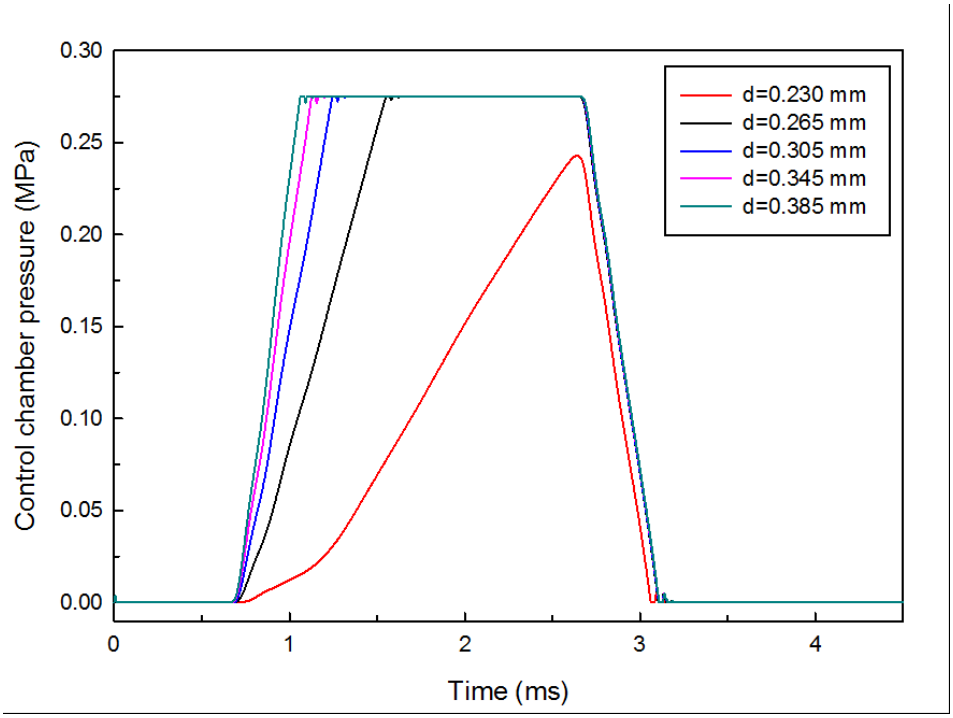

Figure 3-16 Impact of the control oil outlet passage diameter on the needle valve lift

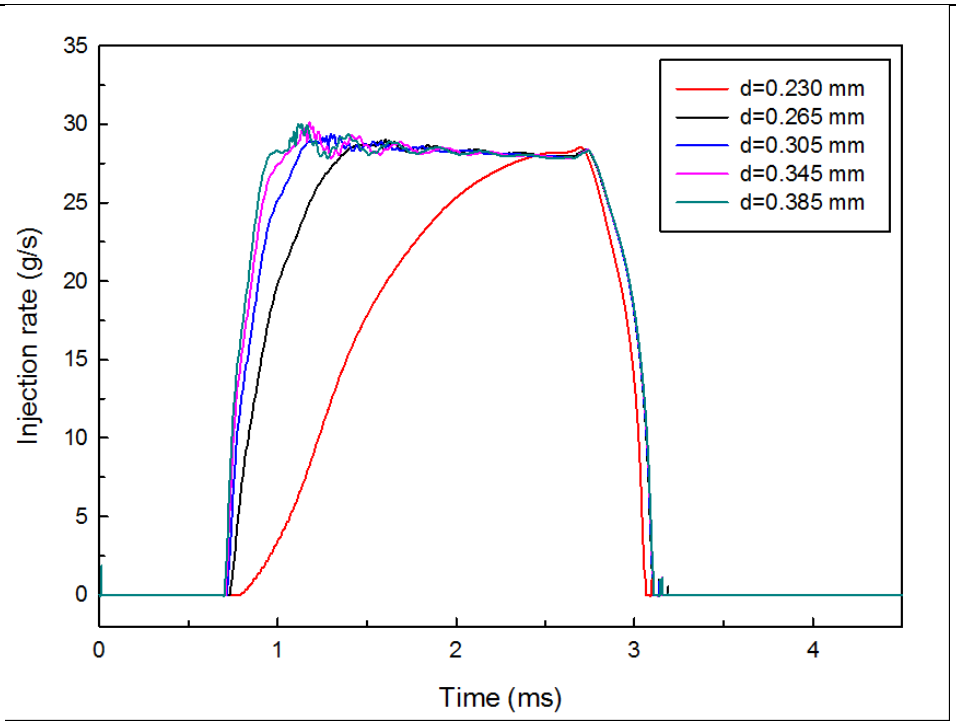

Figure 3-17 Impact of the control oil outlet passage diameter on the injection rate

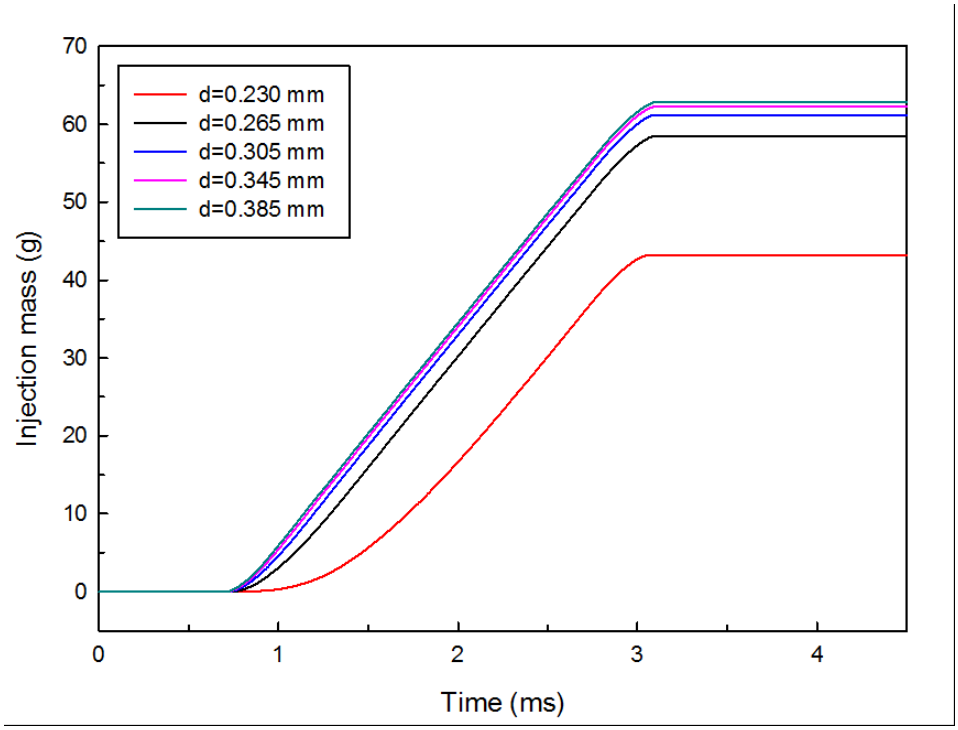

Figure 3-18 Impact of the control oil outlet passage diameter on the injection mass

With an increase in the oil outlet passage diameter, the fuel oil injection quantity increases (as shown in Figure 3-18), the needle valve opening delay shortens and valve closing delay remains nearly the same, as shown in Figure 3-16. This is due to the fact that the OPD determines the oil discharge rate. A larger OPD means that more fuel can be discharged from the control chamber into the low-pressure chamber. Thus, the pressure exerted on the upper surface of the control piston decreases quickly, which helps the needle valve open. In this case, a smaller valve opening delay is achieved. Additionally, a large pressure drop is seen in a large OPD case.

3.4.4. Comparison of the outcome of parametric study

The comparison of the outcome of parametric study is presented in Table 3-2. It can be seen that with the increase in the CPD or IPD, the opening delay increases, the closing delay and the injection mass decrease. However, with the increase in the OPD, the opening delay decreases, the closing delay keeps nearly the same and the injection mass increases. The details refer to chapters 3.4.1 to 3.4.3.

Table 3-2 Comparison of the outcome of parametric study

Increase in	Opening delay	Closing delay	Injection mass
CPD	increasing	decreasing	decreasing
IPD	increasing	decreasing	decreasing
OPD	decreasing	same	increasing

3.5. Multi-objective optimisation

3.5.1. Proposed optimisation routine

The multi-objective optimisation scheme is shown in Figure 3-19. An optimisation routine was built in modeFRONTIER, as is shown in Figure 3-20. Firstly, a random sequence for generating initial designs was adopted in the DOE type. Then, an

NSGA-II algorithm was selected. After that, an AMESim node was used to include the whole electronic fuel injector model, where the displacements of the control signal and the needle valve were generated. These data were firstly written into a text file, and to do this, appropriate writing and reading rules needed to be developed. The text file is read by MATLAB, where the control signal timings (t1, t2, t3 and t4) and needle valve lift timings (T1, T2, T3 and T4) are calculated. The valve opening delay and the valve closing delay can thus be obtained from the timings according to the definition shown in the previous section. Additionally, a constraint was set between the control oil inlet passage diameter and control oil outlet passage diameter so that the former should be smaller than the latter in each run to make sure the needle valve opens in the simulation.

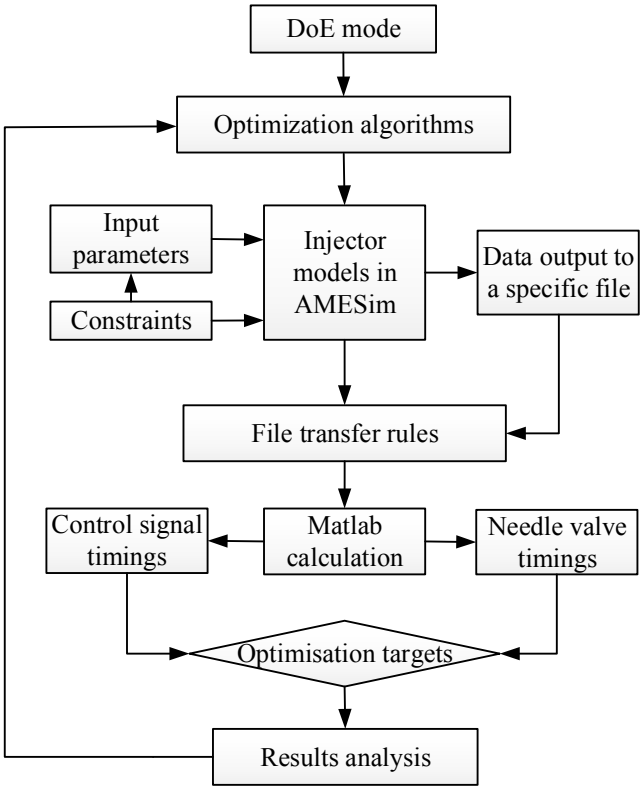

Figure 3-19 Optimisation scheme of the Type-I electronic fuel injector

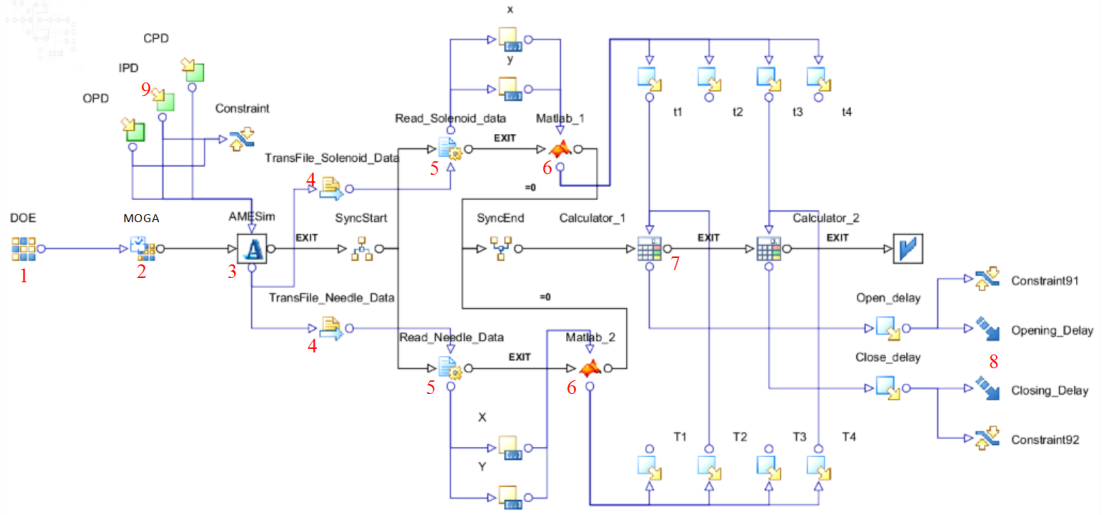

1: DOE type; 2: MOGA Algorithm; 3: AMESim node; 4: transfer the text files of the control signal and the needle valve displacement synchronously; 5: read the control signal data and the needle valve displacement data from files respectively; 6: MATLAB node; 7: calculation of the objectives; 8: objectives; 9: input parameters.

Figure 3-20 Optimisation routine of the Type-I electronic fuel injector

3.5.2. Input parameters and settings

The boundaries and resolutions of the input parameters are specified in Table 3-3. The step of the control piston diameter was set to 0.05 mm, while the steps of the control oil inlet passage diameter and control oil outlet passage diameter were set to 0.005 mm. These boundaries are set according to the results of parametric study in section 3.4.

Table 3-3 Input parameters for the Type-I electronic fuel injector model

Input parameter	Baseline	Lower boundary	Upper boundary	step
CPD (mm)	4.3	3.7	4.5	0.05
IPD (mm)	0.216	0.15	0.28	0.005
OPD (mm)	0.246	0.23	0.38	0.005

3.5.3. Calculation settings

Table 3-4 gives detailed information about the calculation settings for the NSGA-II method. The 50-initial random DOE (design of experiment) designs were each coordinated with 20 generations runs [81]. Thus, a total number of 1000 runs were carried out. In theory, the larger the numbers, the closer the optimal designs to the real Pareto frontier. Other parameters were set as default values in the modeFRONTIER [70]. The mutation probability for real-coded vectors and mutation probability for binary strings are set to the suggested default value 1.0. Explanations can be found in the modeFRONTIER help. It said that the maximum allowed value for this parameter is $p_m = 1/N$, where N is the number of the real-coded variables for real-coded vectors while it is the DNA string length of the binary-coded variables for binary strings. If an exceeding value is set (e.g. the default value 1), then the algorithm resets the parameter value to p_m, casting out a warning message. It is safe to use the default value, 1, and then let the reduction occur.

Table 3-4 Calculation settings

Item	Value
Number of initial designs	50
DOE scheme used	RANDOM
Optimisation algorithm used	NSGA-II
Number of generations run	20
Crossover probability	0.9
Mutation probability for real-coded vectors	default
Mutation probability for binary strings	default
Crossover type for binary-bode variables	simple
Total number of analyses	1000

3.5.4. Results and discussion

3.5.5.1. Effects of design parameters on the injector dynamic response

The effects of the control piston diameter (CPD), control oil inlet passage diameter (IPD) and control oil outlet passage diameter (OPD) on the injector dynamic response are shown in Figure 3-21 to Figure 3-23 respectively. These figures were generated through the RSM function. Only one parameter is changed at a time while the other parameters are kept at the baseline values. Thus, the way in which these important parameters affect the valve opening delay and valve closing delay can be easily seen. From Figure 3-21 (a) and Figure 3-22 (a), it can be seen that the valve opening delay increases with an increase in the CPD and IPD. However, the valve closing delay presents opposite trends to the valve opening delay, as shown in Figure 3-21 (b) and Figure 3-22 (b). These conclusions agree with the results obtained by the parametric study. The increase in the CPD indicates a larger force which delays needle valve opening, on the contrary, this larger force helps closing the needle valve quickly. The increase in the IPD slows down the pressure lose in the control chamber during the needle valve opening and restore the rail pressure fast during the needle valve closing. The valve opening delay and valve closing delay decrease with the increase in the OPD, as shown in Figure 3-23. However, the decreasing trend of the valve opening delay is much steeper than the valve closing delay, which decreases slightly and can hardly be spotted in the parametric study. Additionally, the RSM function figures also indicate the change rate to some extent, for example, in Figure 3-21 (b), the valve closing delay almost remain the same when the CPD exceeds 4.2 mm. This kind of information can be a significant supplement to the outcomes of the parametric study.

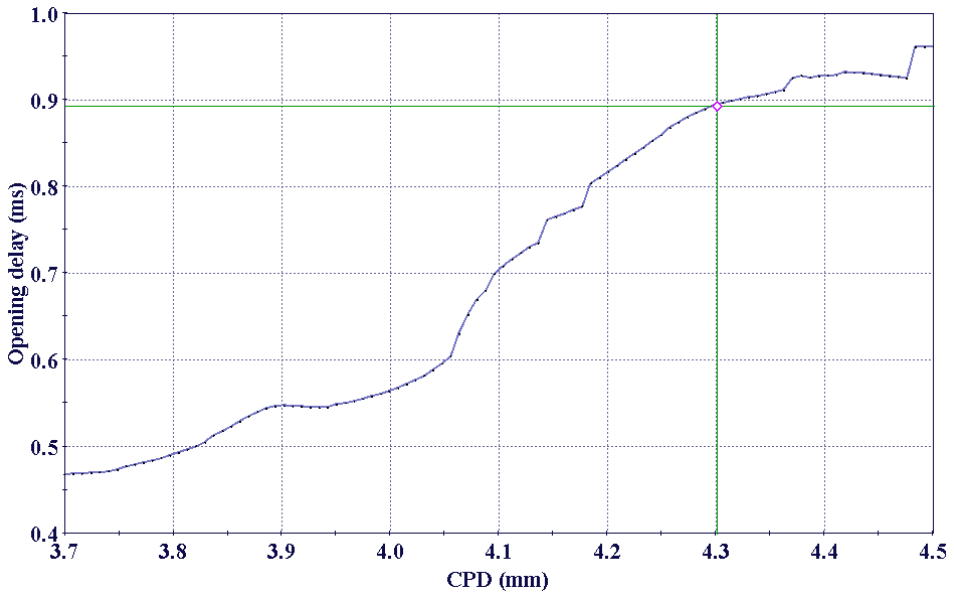

(a) Effects of the CPD on the valve opening delay

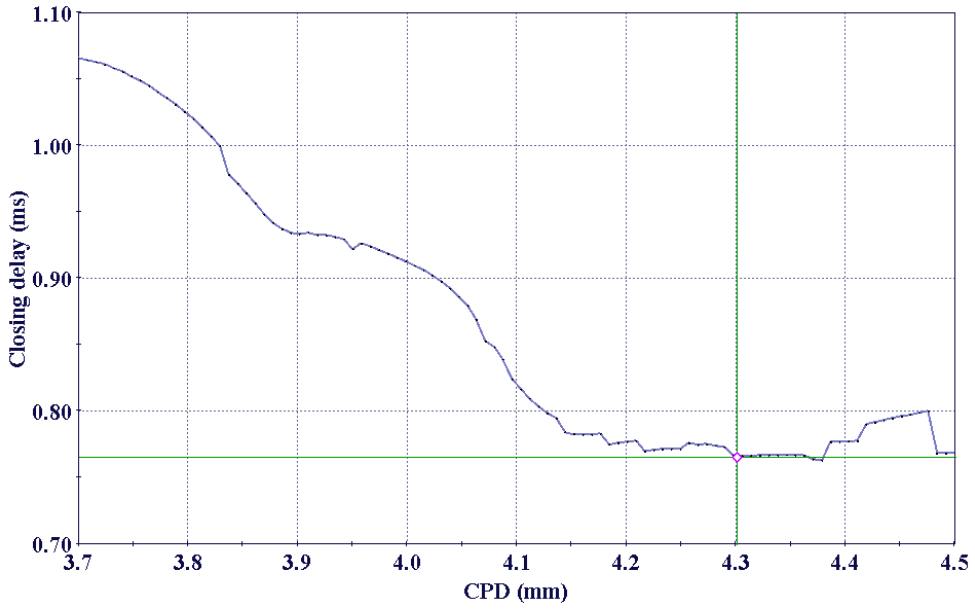

(b) Effects of the CPD on the valve closing delay

Figure 3-21 Effects of CPD on the injector dynamic response

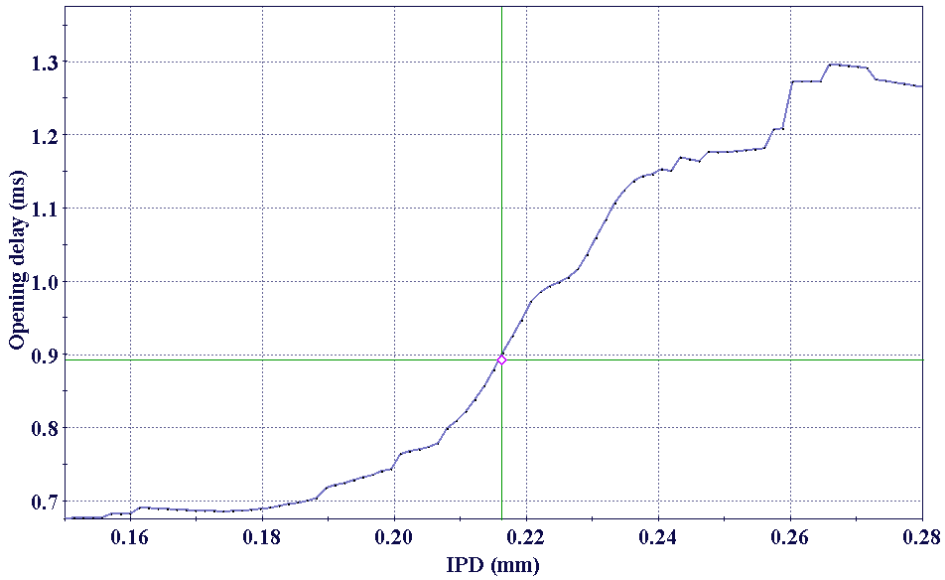

(a) Effects of the IPD on the valve opening delay

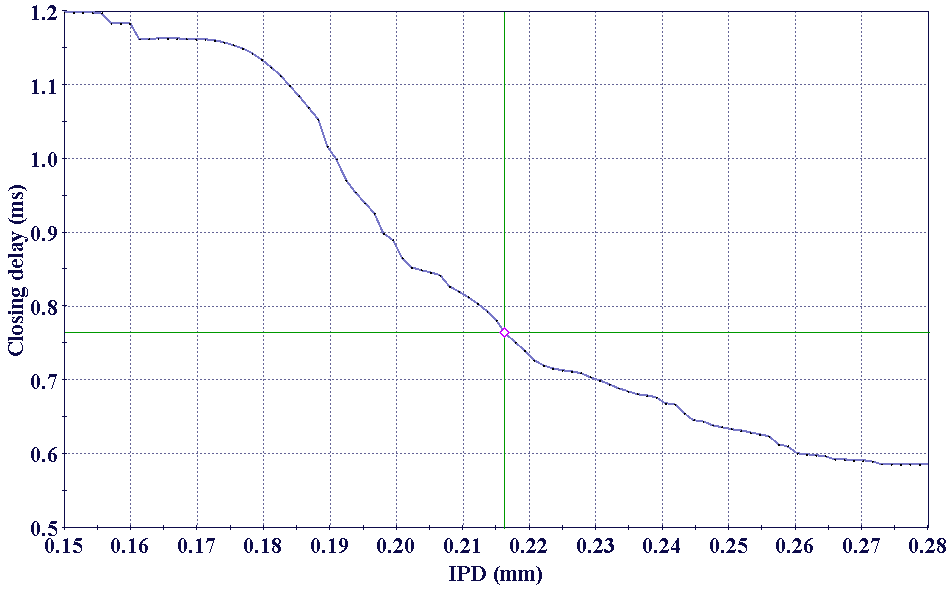

(b) Effects of the IPD on the valve closing delay

Figure 3-22 Effects of the IPD on the injector dynamic response

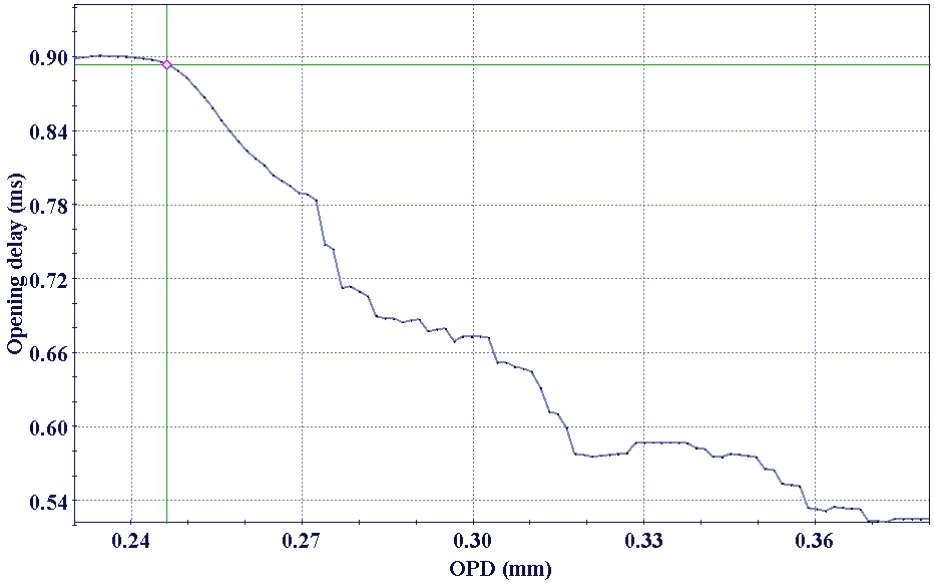

(a) Effects of the OPD on the valve opening delay

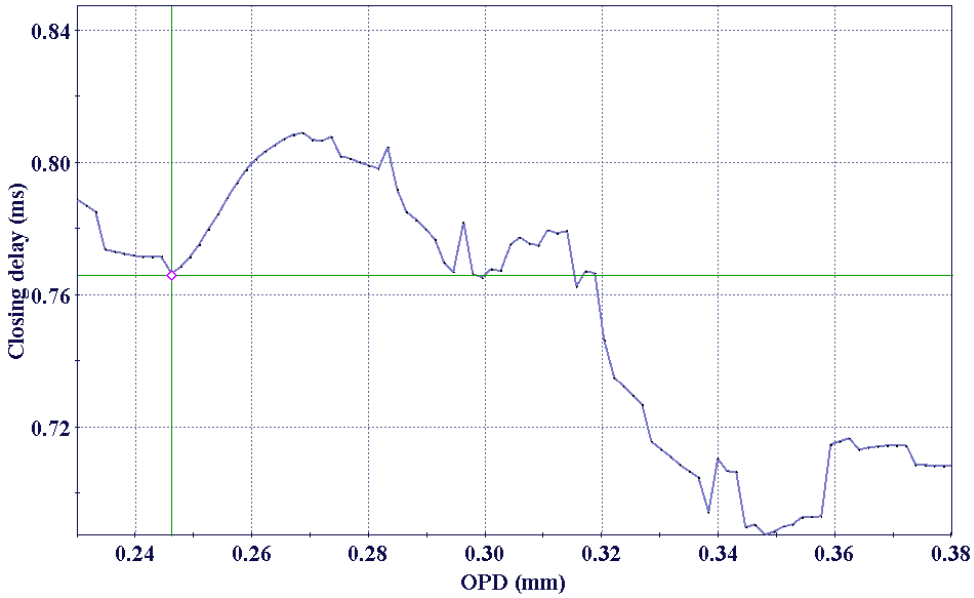

(b) Effects of the OPD on the valve closing delay

Figure 3-23 Effects of the OPD on the injector dynamic response

3.5.5.2. RSM contour maps

The previous section studied the effects of the design parameters on the injector dynamic response independently. However, the dynamic response of an injector is the reflection of the combined effects of all the design parameters; the interactions of them cannot be ignored and are highlighted in this section. The results are presented in Figure 3-24 to Figure 3-26. The cross points of blue lines and red lines in these figures indicate the performance of the baseline design.

Figure 3-24 (a) indicates that a large CPD together with a large IPD drastically increases the valve opening delay. However, it contributes to the decrease of the valve closing delay, in which the IPD has a larger influence than the CPD does, as shown in Figure 3-24 (b). As it is stated in the parametric study, a large CPD reduces the net force which pushes the needle valve upward and enlarges the valve opening delay. This is especially notable when a large IPD is applied, which decreases the pressure drop in the control chamber and increases the valve opening delay.

Figure 3-24 (b) shows that a small valve closing delay is achieved with a large IPD. A small CPD and a small IPD together lead to a significant increase in the valve closing delay. A small IPD decreases the control oil charge rate so that the control chamber needs a longer time to regain the rail pressure. Thus, a larger valve closing delay is the result. Combining this with a small CPD, which weakens the net force that pushes the needle valve downward, an extremely large valve closing delay is estimated.

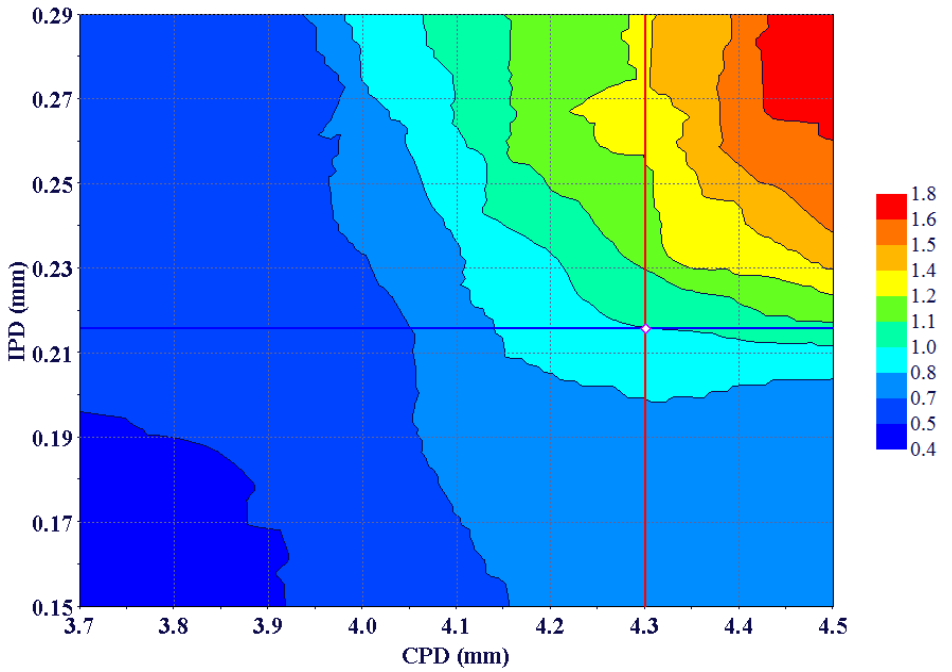

(a) CPD vs IPD on the valve opening delay

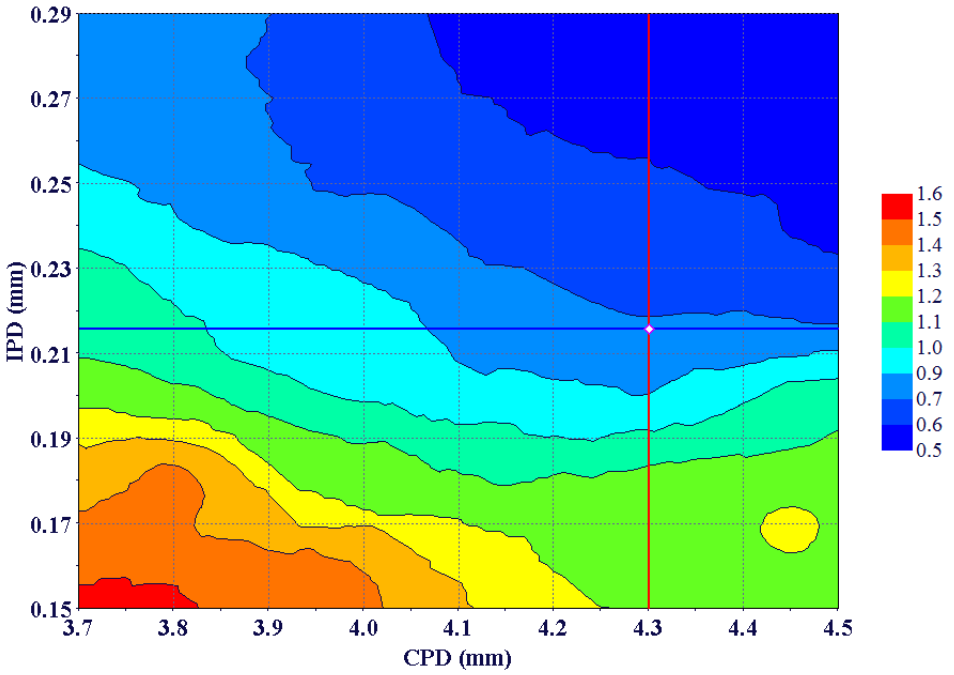

(b) CPD vs IPD on the valve closing delay

Figure 3-24 RSM contours maps of CPD and IPD

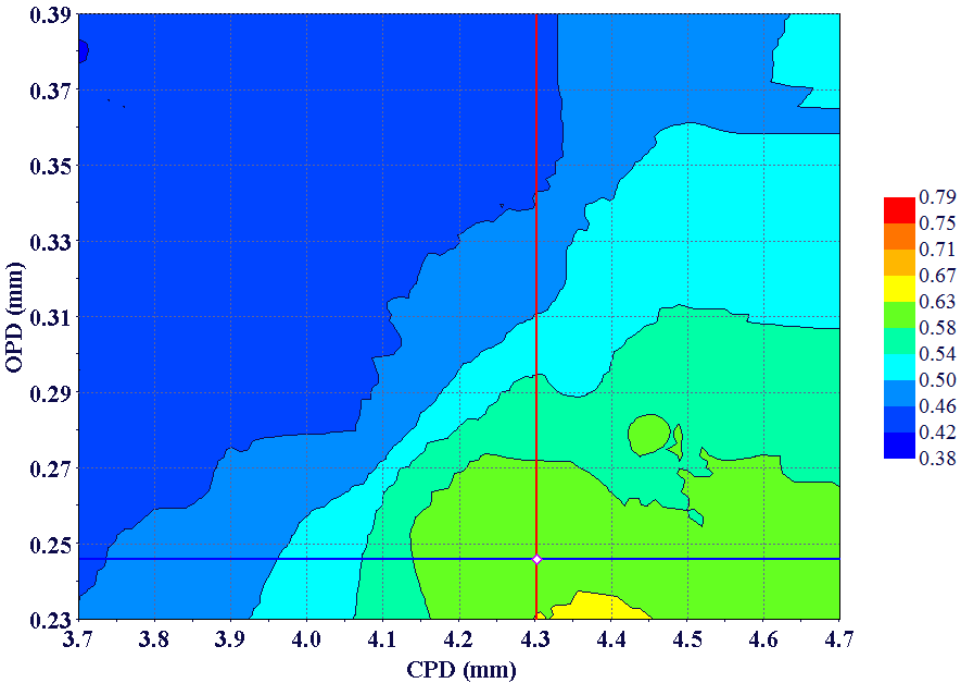

(a) CPD vs OPD on the valve opening delay

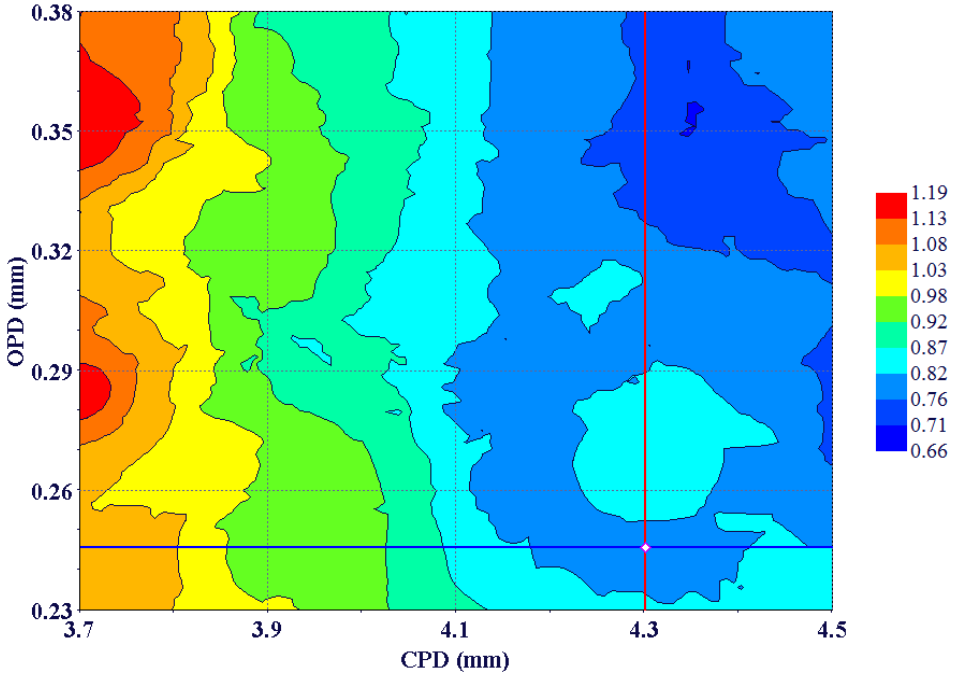

(b) CPD vs OPD on the valve closing delay

Figure 3-25 RSM contours maps of the CPD and OPD

Figure 3-25 (a) indicates that a small CPD along with a large OPD contributes to a small valve opening delay and vice versa. However, a small CPD significantly increases the valve closing delay. Evidence for this behaviour can be found in Figure 3-25 (b). A large OPD means a faster oil discharge rate; thus, when the solenoid valve is energised, a faster pressure drop occurs, as does the pressure drop on the upper surface of the control piston. In particular, an even smaller valve opening delay can be achieved with a larger upward net force generated in this case.

Figure 3-26 (a) demonstrates that a small IPD and a large OPD significantly reduces the valve opening delay, and vice versa. Figure 3-26 (b) reveals that the IPD has an greater effect on the valve closing delay than the OPD does. A small IPD slows down the control oil charge rate to the control chamber whist a large OPD increases the control oil discharge rate at the same time. In this case, an extremely small valve opening delay is obtained.

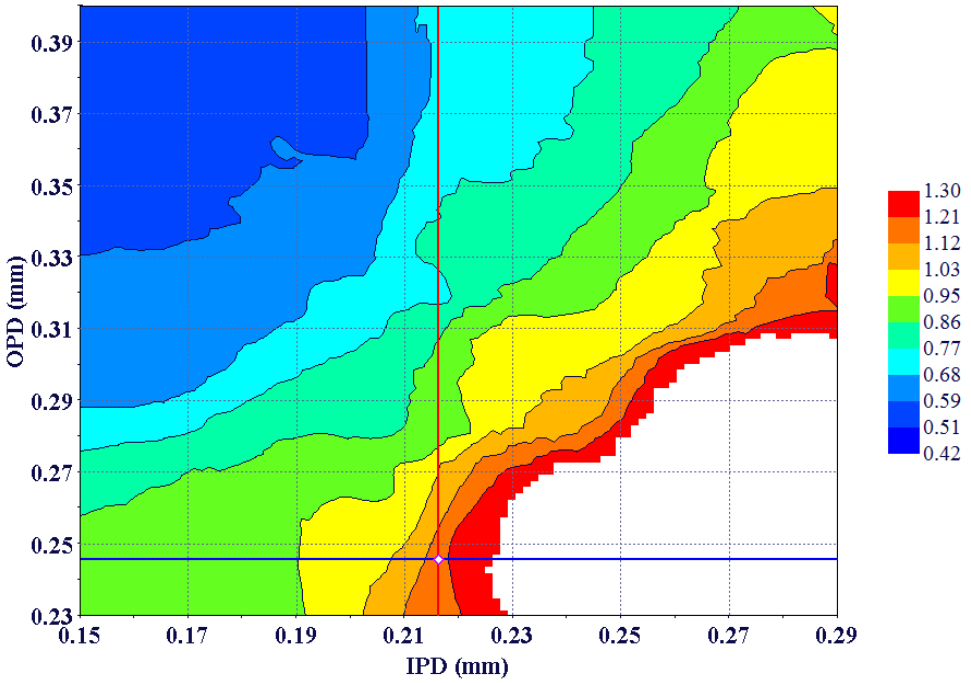

(a) IPD vs OPD on the valve opening delay

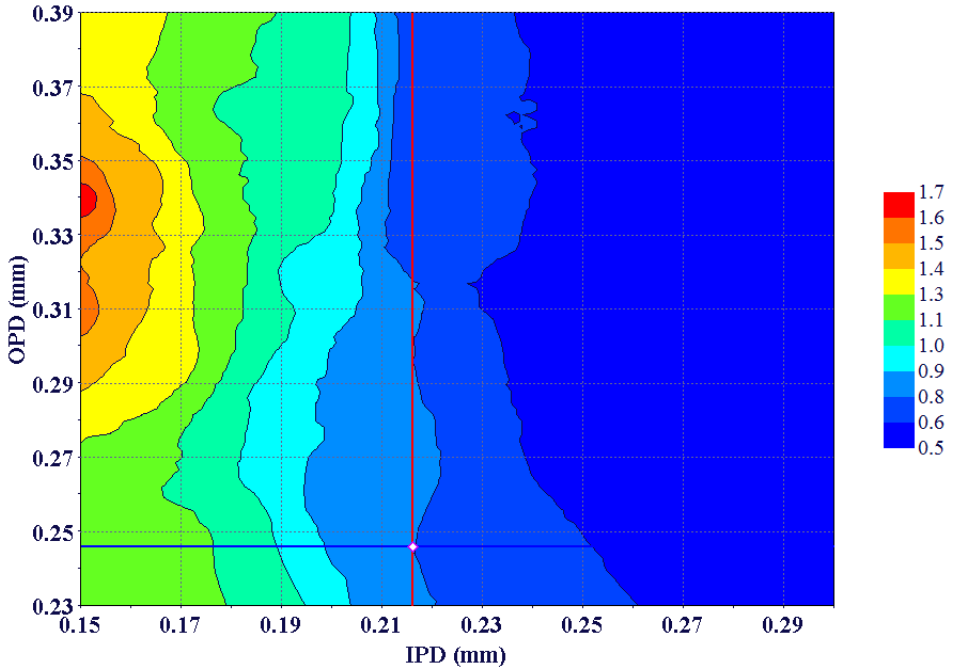

(b) IPD vs OPD on the valve closing delay

Figure 3-26 RSM contours maps of the IPD vs OPD

3.5.5.3. Pareto optimum

The meaning of Pareto optimum was presented in the Section 2.5.4. The trade-off between the valve opening delay and the valve closing delay is shown by a scattering chart, as presented in Figure 3-27. The black triangle points mark the Pareto designs. The blue square represents the baseline design, whilst the green hollow triangle represents the optimal design which has the shortest distance to coordinate origin. In this study, the optimal design has the best balance between the valve opening delay and the valve closing delay, it is Comparisons between the optimal design and the baseline design are given on both the dynamic response and design parameters (Table 3-4 and 3-6). The optimal design achieve reductions of 40% and 25% to the baseline design on the valve opening delay and valve closing delay respectively.

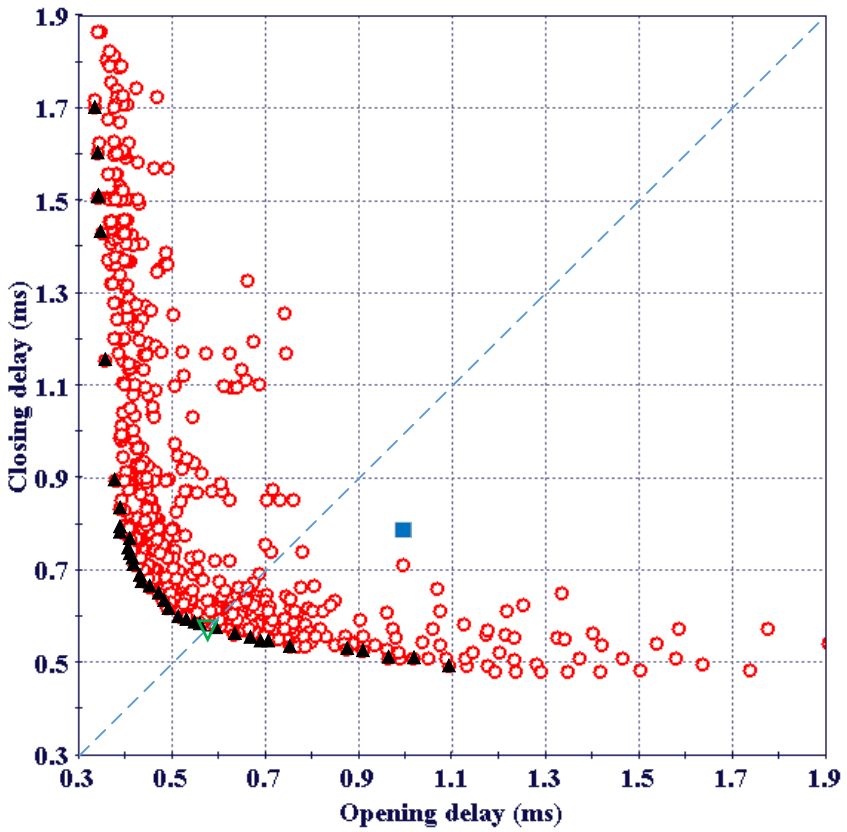

Figure 3-27 Scattering charts of the valve opening delay vs the valve closing delay

Table 3-5 Comparisons of the optimal design and the baseline design

Pressure (MPa)	Delay	Baseline design (ms)	Selected design (ms)	Status	Degree (%)
130	Opening	0.954	0.573	↓	39.94
	Closing	0.785	0.588	↓	25.10

Table 3-6 Comparison of structure parameter value before and after optimisation

Parameters	Baseline	Optimum
Control piston diameter (mm)	4.3	4.2
Control oil inlet passage diameter (mm)	0.216	0.255
Control oil outlet passage diameter (mm)	0.246	0.365

3.6. Summary

In this chapter, the effects of the control piston diameter (CPD), control oil inlet passage diameter (IPD) and control oil outlet passage diameter (OPD) on the injector characteristics and dynamic response were examined in depth through a parametric study and a multi-objective optimisation. In the multi-objective optimisation, a optimisation routine was proposed: one of the MOGA methods (the NSGA-II method) was used in the optimisation process. A total of 1000 runs were executed under 130 MPa rail pressure. The effects of these design parameters on the dynamic response were shown by RSM function charts. Subsequently, their interactions were investigated through RSM contour maps. Additionally, the trade-off relationship between the valve opening delay and the valve closing delay was investigated via a scattering chart, in which the Pareto designs and an optimum were highlighted.

The main outcomes are as follows:

(1) With an increase in control piston diameter and control oil inlet passage diameter, the valve opening delay increased and the valve closing delay reduced. However, the

control oil outlet passage diameter seems to only affect the valve opening delay, which decreases with the increase in control oil outlet passage diameter.

(2) NSGA-II is an effective way for optimising the key structural design parameters of the electronic fuel injectors. A clear trade-off was spotted between the valve opening delay and valve closing delay.

(3) A large control piston diameter together with a large control oil inlet passage diameter increases the valve opening delay. However, they contribute to an increase in the valve closing delay, in which the control oil inlet passage diameter has a larger influence than the control piston diameter does. A small control piston diameter and a small control oil inlet passage diameter together lead to a significant increase in the valve closing delay.

(4) A small control piston diameter along with a large control oil outlet passage diameter contributes to a small valve opening delay and vice versa. However, a small control piston diameter significantly worsens the valve closing delay.

(5) A small control oil inlet passage diameter and a large control oil outlet passage diameter significantly reduces the valve opening delay, and vice versa. The control oil inlet passage diameter has a much greater effect on the valve closing delay than the control oil outlet passage diameter.

(6) The optimum design shows a balanced dynamic response, which achieves considerable reductions of 40% and 25% compared with the baseline design on the valve opening delay and valve closing delay respectively.

Chapter 4. Optimisation of the Type-II fuel injector

The previous section studied the effects of three structural design parameters on the injection characteristics and on the dynamic response. An effective and validated routine was described for the optimisation of Type-I electronic fuel injectors. In this section, this optimisation routine is introduced for the optimisation of the Type-II electronic fuel injector, which is designed and manufactured by China Shipbuilding Industry Cooperation. It aims for the implementation on medium-speed marine diesel engines by the cooperation with HPCR fuel oil injection systems. Three more design parameters were considered in the optimisation, they are: the spring preload force, the nozzle orifice diameter and the nozzle orifice number. The additional parameters significantly increased the optimisation complexity and analysis difficulty. In this circumstance, the sensitivity of design parameters on dynamic response was investigated to exclude parameters which have little effect on the dynamic response.

4.1. 1D modelling of the Type-II fuel injector

The 1D simulation model of the Type-II fuel injector was also built in AMESim software. The whole model was divided into three parts, i.e., the solenoid assembly, the injector body and the nozzle assembly. The detailed modelling process is demonstrated below.

4.1.1. Assumptions of the model

In the model, some assumptions were made that all the variations are considered to be isothermal, so, the fuel oil temperature was assumed to be constant in the injector and equal to the one at the injector inlet, and the fuel properties were assumed to be constant [82]. Additionally, a constant pressure source was adopted here to simulate the pressure from common rail, which neglected the pressure fluctuations caused by the cyclical oil supply from high-pressure oil pumps. Moreover, the pressure wave propagation was not considered in the model too.

4.1.2. Modelling of the solenoid assembly

In Figure 4-1, C1 is the solenoid spring, C2 is the solenoid coil, C3 is the control valve, V1 is the low-pressure chamber and C4 is the ball valve. The left part of Figure 4-1 shows a physical sketch of the solenoid assembly. The right part of the figure is part of a model built according to the physical sketch. The control valve C3 is the moving element of the solenoid assembly, which is raised up when the solenoid coil C2 is energised to take the ball valve C4 off its seat, thus, opened the control oil outlet passage. The parameters for the solenoid assembly are shown in Table 4-1.

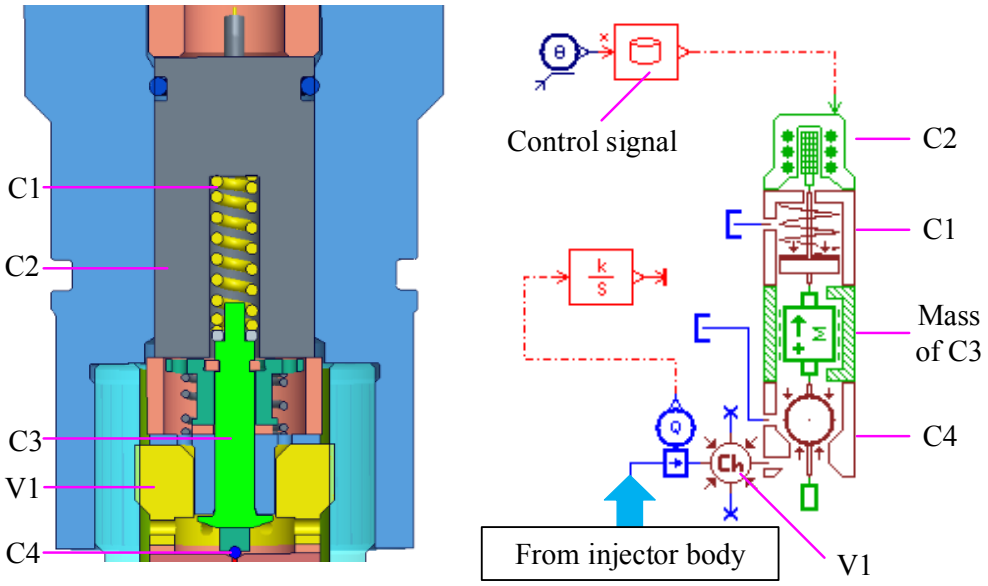

Figure 4-1 Modelling of the solenoid assembly

Table 4-1 Parameters for the solenoid assembly

Element	Diameter (mm)	Spring rate (N/m)	Volume (cm^3)	Mass (g)
C1	-	70	-	-
C3	-	-	-	4
V1	-	-	0.001	-
C4	1.2	-	-	-

4.1.3. Modelling of the injector body

In Figure 4-2, C5 is the control piston and C6 is the mandrel pushing rod. O1 and O2 stand for the control chamber control oil inlet passage and the control oil outlet passage respectively. L1-L5 represent oil lines. V0 is the rail volume and V2 is the control chamber volume.

A model of the injector body is shown on the right part of Figure 4-2. In the model, a constant pressure in V0 was adopted to simulate the pressure in the common rail. The common rail is connected to the injector through high-pressure pipes, i.e. L2 and L4. L2 leads to the control chamber via a short tube L3 and the control chamber control oil inlet passage O1. L4 leads to the nozzle part. The volume of V2 represents the volume of the control chamber. It is connected to the solenoid valve via the control oil outlet passage O2. The piston model C5 from the AMESim software includes a rod with a piston. However, there is no rod in the control chamber, therefore, the diameter of the rod is set to zero in the model. Moreover, the mass, leakage, piston surfaces and stiffness of the C5 are also included according to their physical characteristics. Lines L5 represent the control oil return lines. The parameters for the injector body are shown in Table 4-2.

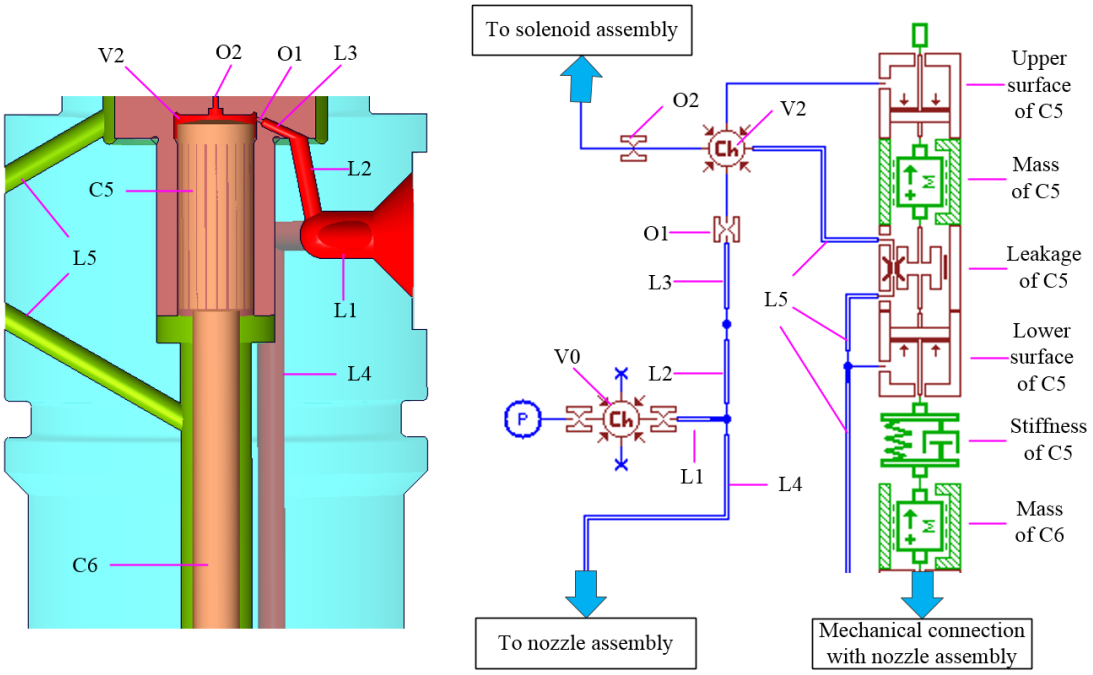

Figure 4-2 Modelling of the injector body

Table 4-2 Parameters for the injector body

Element	Length (mm)	Diameter (mm)	Spring rate (N/m)	Dumper rating (N/(m/s))	Volume (cm^3)	Mass (g)
V2	-	-	-	-	0.024	-
O2	-	0.45	-	-	-	-
O1	-	0.3	-	-	-	-
L3	2.55	0.8	-	-	-	-
L2	6.32	1.5	-	-	-	-
C5	12.5	6.5	4e+8	400	-	6.4
L1	4.2	4	-	-	-	-
L5	-	-	-	--	-	-
L4	94.6	2.3	-	-	-	-
C6	-	-	-	-	-	6.4

4.1.4. Modelling of the nozzle assembly

Figure 4-3 shows a cross-sectional view of the nozzle assembly and its model, where C7 is the needle valve spring, C8 is the needle valve body, and C9 is the nozzle. V3 is the return oil chamber while V4 is the accumulation chamber. L4 is the inlet of the high-pressure control oil to the accumulation chamber V4. The nozzle assembly connects to the injector body both hydraulically and mechanically. It has a cylindrical type of orifices. The needle valve stiffness and mass are considered in the modelling and simulation. A piston model from AMESim is used to simulate the hydraulic force acting on the lower part of the needle valve in the accumulation chamber. The nozzle orifice parameters and their layout are the import parts in the modelling of the nozzle assembly. Here, the group of parameters should be set accurately, for example, the needle valve diameter, the valve seat angle, the needle cone angle, the sac volume, the maximum flow coefficient of the orifices and the number of orifices. The parameters for the nozzle assembly are shown in Table 4-3.

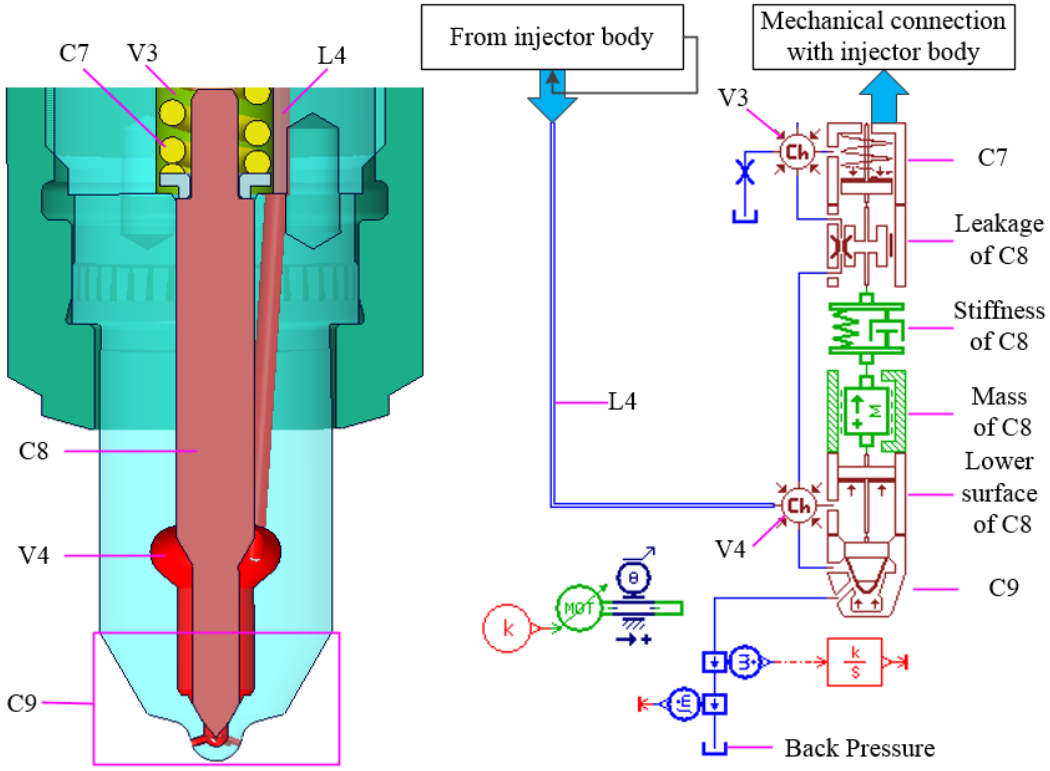

Figure 4-3 Modelling of the injector nozzle assembly

Table 4-3 Parameters for the injector nozzle assembly

Element	Orifice number	Diameter (mm)	Spring rate (N/m)	Dumper rating (N/(m/s))	Volume (cm^3)	Mass (g)
V3	-	-	-	-	0.2	-
C7	-	-	13000	-	-	2.58
C8	-	-	4e+8	400	-	8.6
V4	-	-	-	-	0.348	-
C9	9	0.27	-	-	-	-

4.1.5. Integration of the Type-II fuel injector model

A complete sketch of the injector model is shown in Figure 4-4. It is the integration of the solenoid assembly, injector body and the nozzle assembly.

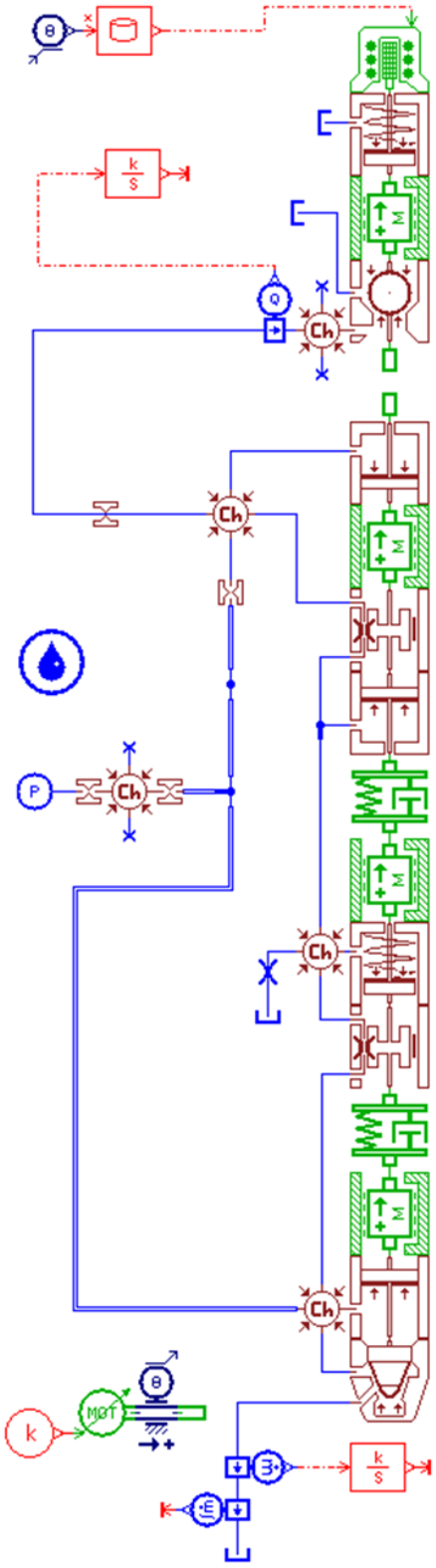

Figure 4-4 Complete sketch of the Type-II electronic fuel injector model

4.2. Model validation

4.2.1. Fuel properties

A common marine gas oil #0 diesel fuel was used in the study, the main properties of the fuel are shown in Table 4-4.

Table 4-4 Physical and chemical properties of the #0 diesel fuel

Properties	Value
Density at 20 ℃, kg/m^3	845
Viscosity at 20 ℃, mm^2/s	4.72
Cetane number	57.6

4.2.2. Experimental facilities

The experiments were carried out on a HIL (hardware in loop) test rig. HIL is used for semi-physical simulation, where some components in the loop are replaced by software models. A sketch of the HIL test rig is shown in Figure 4-5, in which the actual diesel engine was replaced by a diesel engine model built in LABCAR[1] [83]. Its working principle is as follows:

(1) A PID method is adopted to speed governing, i.e., the cycle injection quantity (⑥) is obtained in the ECU (⑤) by comparing the speed calculated from the

[1] A Hardware-in-Loop (HiL) simulator built by ETAS company. LABCAR's main differentiator is its open, modular architecture, which allows the testing system to be easily adapted and functionally extended to suit future requirements. The strict separation of the system-specific hardware and the PC-based computing engine provides a high degree of investment protection. It contains the following functions: (1) Compact real-time testing system for automotive Embedded Control Units (ECUs); (2) Open, modular system architecture for simulation models, software, hardware, test automation, and time-synchronous ECU access; (3) PC-based simulation with extensive possibilities (Dual-Core, Quad-Core, etc.)

camshaft signal (⑭) and crankshaft signal (⑮) with a given speed.

(2) The width of the control signal (⑧) to fuel injectors is decided by the cycle injection quantity.

(3) Rail pressure (⑬) is obtained by the ECU and is set as one of the input parameters to the diesel engine model. The feeding pumps of the common rail system are controlled by proportional valves to match with the fuel quantity injected.

(4) Engine speed is calculated in the diesel model by combining the cycle injection quantity (⑥) and load settings (③). This engine speed is transformed into signals to control the servo motor, which drives the camshaft (⑳) to simulate the engine operation.

(5) All of the signals including temperatures, pressures and I/O status are monitored through the Compact RIO (②) and displayed in the computer (①).

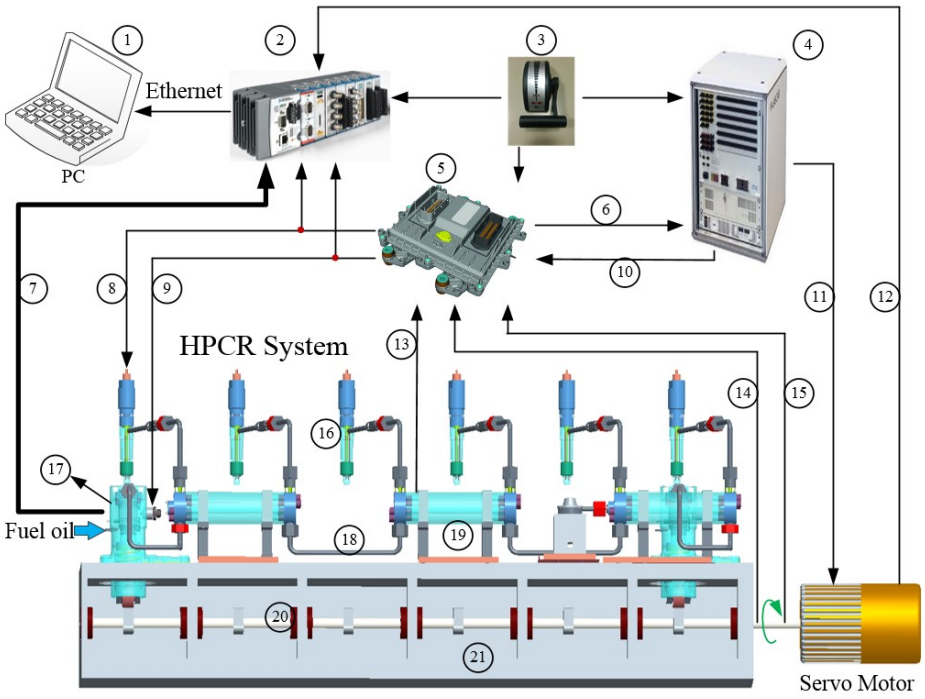

①: computer; ②: Compact RIO (a real-time embedded industrial controller made by National Instruments); ③: engine telegraph; ④: LABCAR system (a flexible test system developed by ETAS); ⑤: ECU; ⑥: cycle fuel oil injection quantity; ⑦: sensor signals of the HPCR system; ⑧: ECU injection signal; ⑨: ECU control signal for the proportional valve; ⑩: correction signal from the LABCAR; ⑪: control signal for the servo motor; ⑫: encoder speed signal; ⑬: pressure signal of rails; ⑭: camshaft angle signal; ⑮: crankshaft angle signal; ⑯: injector; ⑰: high pressure pump; ⑱: high pressure oil tub; ⑲: common rail; ⑳: camshaft; ㉑: oil pan.

Figure 4-5 Systematic configuration of the HIL test rig

4.2.2.1. Injection quantity measurement

One of the most important parts of the HIL test rig is the injection quantity measurement device, as shown in Figure 4-6. Fuel oil injected from the injector (①) flows through the demister (②) and cooler (④) successively, then flows to the fuel weighting device. Two weighting methods are available: one measures the fuel volume via a measuring glass (⑧), the other weighs the fuel mass via an electronic scale (⑨). The two methods can be switched between by using a PLC (⑫) controlled electronic three-way valve (⑤).

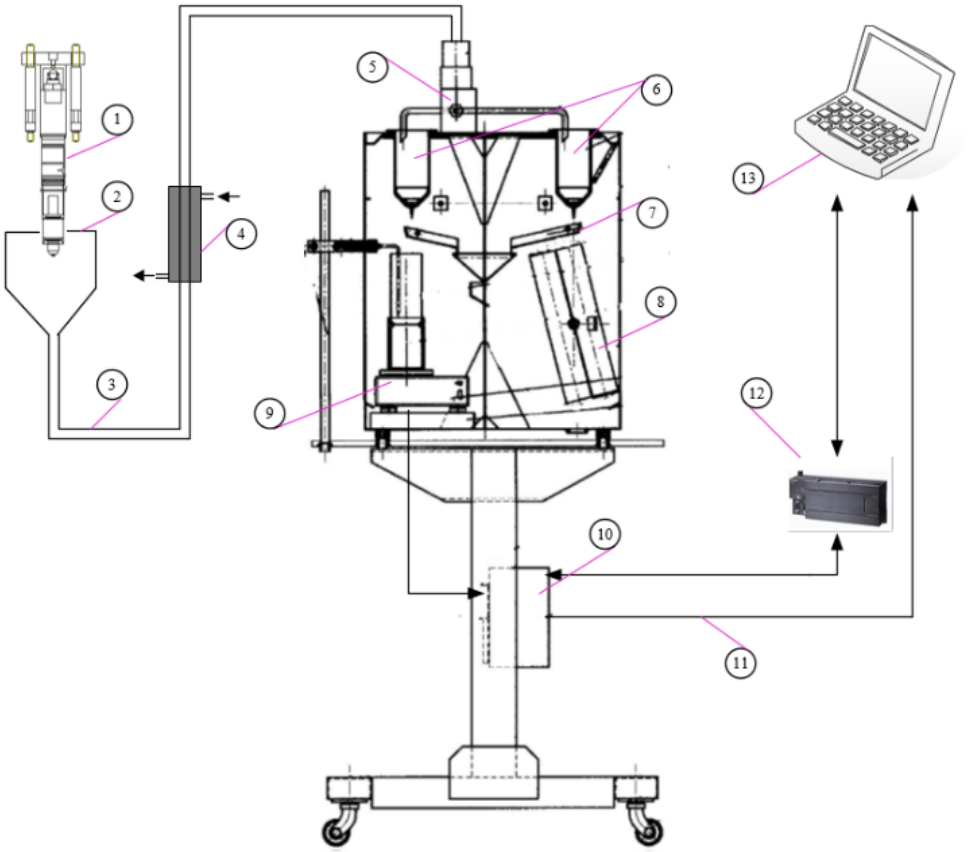

①: electronic fuel injector; ②: demister; ③: oil tube; ④: cooler; ⑤: three-way valve; ⑥: collector; ⑦: oil baffle plate; ⑧: measuring glass; ⑨: electronic scale; ⑩: junction box; ⑪: cables; ⑫: PLC.

Figure 4-6 Fuel oil measurement device

The test rig is shown in Figure 4-7.

Figure 4-7 Image of the HIL test rig

Figure 4-8 Front view of the HPCR system in the HIL test rig

Figure 4-9 Side view of the HPCR system in the HIL test rig

Figure 4-10 Fuel mass measuring device (left) and console desk (right)

4.2.3. Simulation validation

Limited by the experimental conditions, only the injection quantity data were obtained for validating the Type-II electronic fuel injector model from the HIL test rig. The injection quantity was measured at room temperature and under four different rail pressures, i.e., 80 MPa, 100 MPa, 120 MPa and 140 MPa. Under each pressure, four different fuel oil injection duration widths were applied, i.e., 1 ms, 1.5 ms, 2 ms and 2.5 ms. At each injection duration, the injection quantity was obtained by calculating the average of 100-time injection. The injection quantity comparison of simulation results and experimental results are shown in Figure 4-11. Errors may be caused by the fuel oil measurement device or the invalidated flow coefficient of the nozzle orifice. However, the main trend in simulation data for average injection quantity shows an agreement with the experiment data under all four different rail pressures.

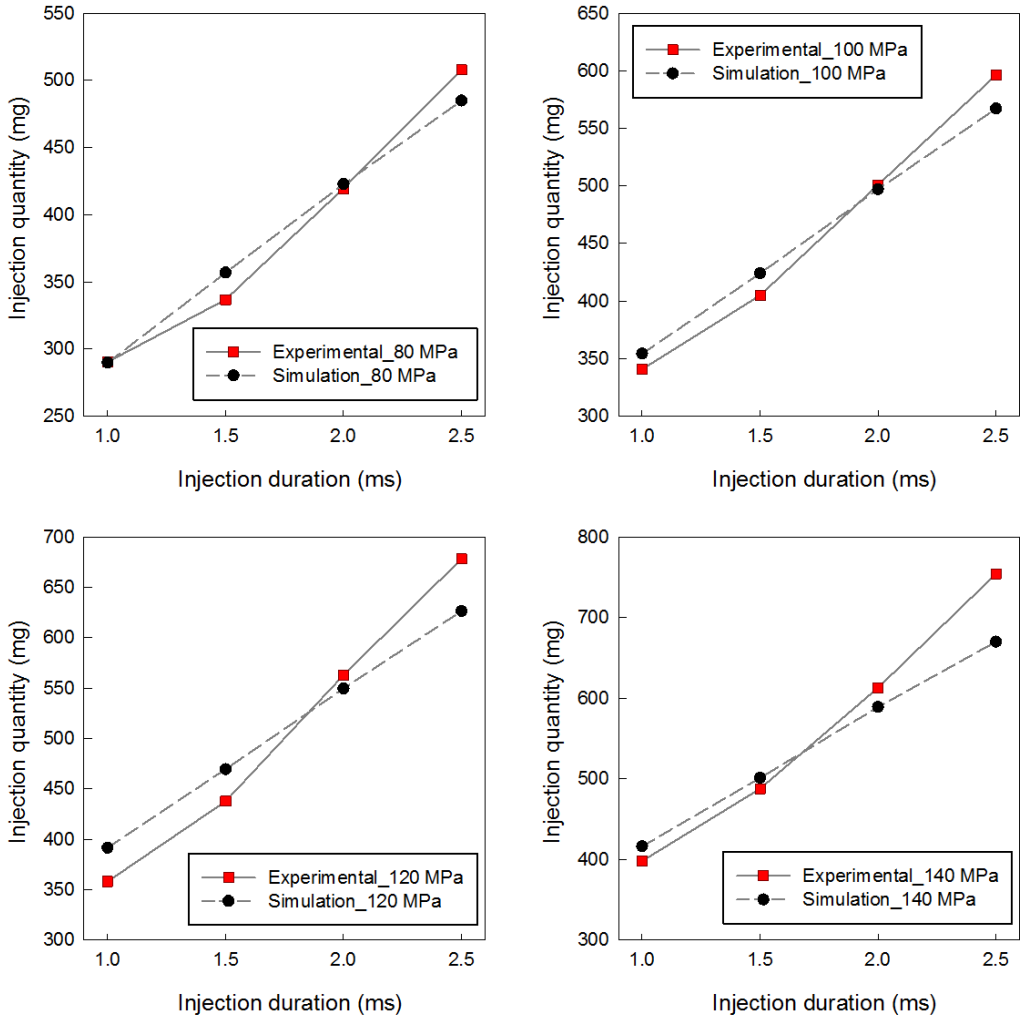

Figure 4-11 Injection mass comparisons of experimental data and simulation data

4.3. Multi-objective optimisation of the Type-II electronic fuel injector

4.3.1. Optimisation routine

In Section 3.5.1, the proposed optimisation routine for the Type-I fuel injector was presented. In this section, the proposed optimisation routine is extended to the optimisation of the Type-II electronic fuel injector, as shown in Figure 4-12. Compared to the optimisation routine of the Type-I fuel injector, the optimisation

routine for the Type-II fuel injector was similar, except for the addition of three more design parameters, the nozzle orifice number, the nozzle orifice diameter and the spring preload force were included.

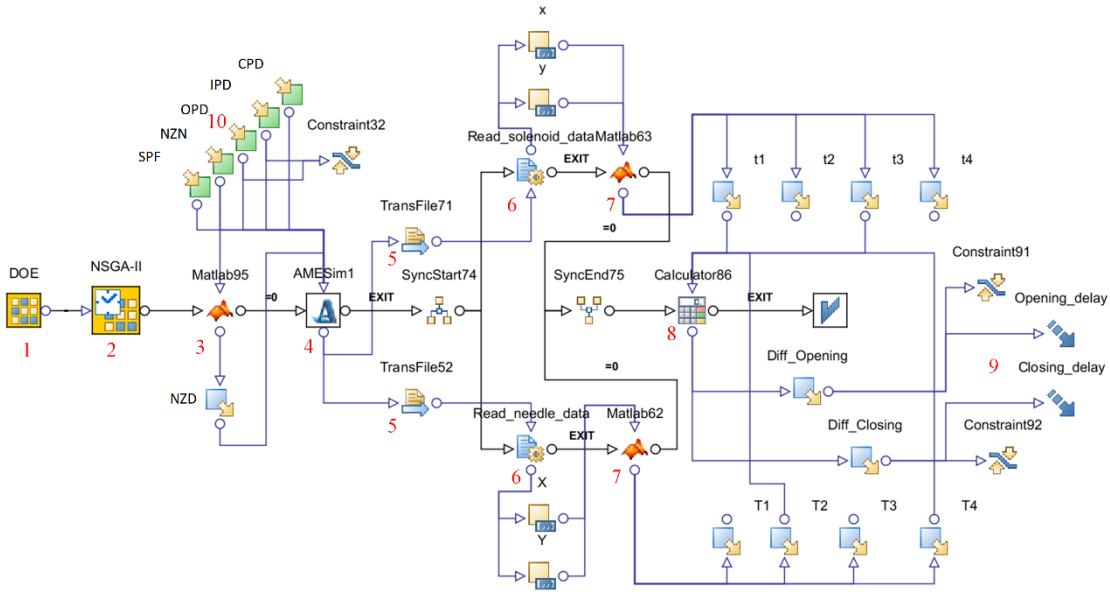

1: DOE type; 2: MOGA Algorithm; 3: MATLAB node; 4: AMESim node; 5: transfer the text files of the control signal and the needle valve displacement synchronously; 6: read the control signal data and the needle valve displacement data from files respectively; 7: MATLAB node; 8: calculation of the objectives; 9: objectives; 10: input parameters.

Figure 4-12 Multi-objective optimisation routine the Type-II fuel injector

4.3.2. Design parameters and boundaries

The boundaries and resolution of input parameters are specified in Table 4-5. Five input parameters, including the control piston diameter (CPD), control oil inlet passage diameter (IPD), control oil outlet passage diameter (OPD), nozzle number (NZN) and spring preload force (SPF) are presented. Another input parameter nozzle orifice diameter (NZD) was set according to the NZN, as shown in Figure 4-13. This is mainly for the purpose of keeping the cross-sectional area within a certain range. Here, the parameter NZD was set to five values according to the NZN; they were chosen randomly in the MATLAB node. A total of six design parameters were considered in the optimisation. The specific lower and upper boundaries were

selected according to a trial experience study.

Table 4-5 Input parameter for the optimisation routine

Input parameter	Lower boundary	Upper boundary	Resolution
Control piston diameter (mm)	5.8	8.0	0.1
Control oil inlet passage diameter (mm)	0.2	0.45	0.01
Control oil outlet passage diameter (mm)	0.36	0.9	0.02
Nozzle number (-)	6	10	1
Spring preload force (N)	60	360	10

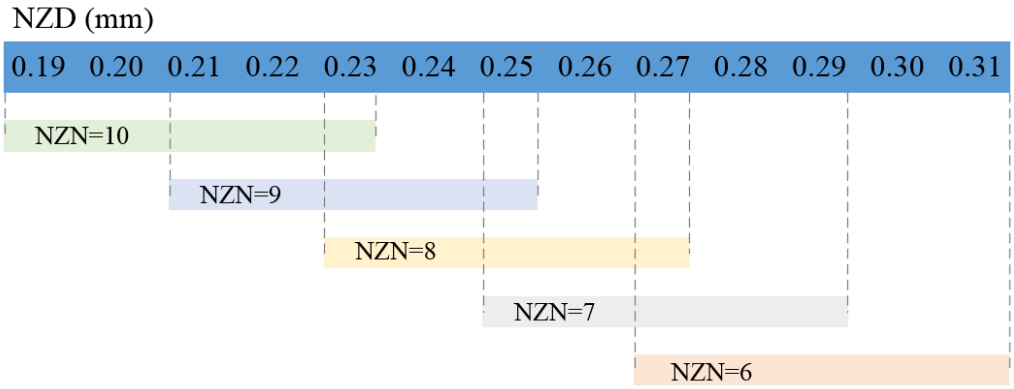

Figure 4-13 The description of the NZD under various NZN values

4.3.3. Calculation parameters' settings

Table 4-6 gives information about the basic calculation settings. A random DOE scheme was adopted. The number of initial designs was 100, and that of the generations was 20. Therefore, that the total number of analyses was 2000. The larger the number, the closer the simulation optimums are to real Pareto front of optimum results. The algorithm used here is NSGA-II, which is described in Section 2.5.3.

Table 4-6 Calculation settings

Item	Value
Number of initial designs	100
DOE scheme	RANDOM
Optimisation algorithm	NSGA-II
Number of generations runs	20
Crossover probability	0.9
Mutation probability for real-coded vectors	default
Mutation probability for binary strings	default
Crossover type for binary-Code variables	simple
Total number of analyses	2000

4.4. Results and discussion

4.4.1. Influential factors analysis

As six design parameters (see Section 4.3.2) are involved in the optimisation, it is necessary to the sensitivity of design parameters on the dynamic response. Based on this, the importance of the structural parameters and their interactions with the objectives (the valve opening delay and valve closing delay) were studied through a second order Smoothing Spline Analysis of Variance (ANOVA) algorithm. Here, the structural parameters and their interactions refer to the factors. The sensitivity of design parameters on the dynamic response is shown in Figure 4-14. All of the weights of the factors add up to 1 and only the six most influential factors are reported in the figure. The left column and the right column in the figure reflect the importance of the factors in affecting the valve opening delay and valve closing delay,

respectively. The first row, the second row and the third row demonstrate the results under rail pressures of 80 MPa, 120 MPa and 160 MPa, respectively.

The left column of Figure 4-14 indicates that the parameters control piston diameter (CPD), the control oil inlet passage diameter (IPD), the control oil outlet passage diameter (OPD) and their interactions are the most influential factors on the valve opening delay of all three rail pressures. Although the CPD and IPD and their interactions rank as the first three factors, other factors such as the OPD, and interactions between the CPD & IPD and between the IPD & OPD are not negligible. The right column of Figure 4-14 shows that the IPD has a dominant influence on the valve closing delay, which is nearly three times larger than that of the CPD, which is the second largest influential factor. The influence of the nozzle orifice number (NZN) and nozzle orifice diameter (NZD) on dynamic response are much less than that of the IPD and CPD. The effects of these important factors on the dynamic response were demonstrated by RSM function charts at 160 MPa pressure, which is shown in Figure 4-15. It can be seen that the main trends of the CPD, IPD and OPD are consistent with that of the Type-I fuel injector, as shown in Section 3.6.1. The change of the control piston diameter changes the upper surface area to change the pressure on it. The change of control oil inlet passage diameter changes the control oil charge rate to the control chamber. The change of control oil outlet diameter alters the fuel oil discharge rate from the control chamber to the low-pressure chamber. The detailed influences of these important factors are documented in Section 3.4.

The left column of Figure 4-14 indicates that the CPD is the most influential factor in the valve opening delay at 80 MPa and 120 MPa pressure, but its position is replaced by the IPD at 160 MPa pressure. This is because, in high-pressure conditions, a larger oil charge rate can be seen than that in low-pressure conditions, even if the IPD remains the same. A larger control oil charge rate means a larger valve opening delay and a smaller valve closing delay. Another phenomenon that the CPD is relevant to the valve closing delay under a low-pressure condition, and the relevance decreases at medium pressure and increases again under a high-pressure condition, as shown in the right column of Figure 4-14. A possible reason is the different samples

used for the analysis since these different samples were generated by three different runs under three different pressures.

From the third row of Figure 4-15, it can be seen that the valve closing delay decreases with the increase in SPF. It can be easily understood that a larger SPF pushes the needle valve upward faster. In other words, a larger spring preload force (SPF) increases the downward net force so that the movement of the needle valve is accelerated to shorten the valve closing delay. From the right column of Figure 4-14, it can be seen that the SPF affects objectives under a low-pressure condition but its influence diminishes at high-pressure condition. This is due to the reason that the rates of the SPF to the pressures under a low-pressure condition are larger than those under a high-pressure condition. Therefore, the SPF is more comparable to the small hydraulic forces at low-pressure condition; however, it becomes outweighed by the large hydraulic forces when the pressure increases.

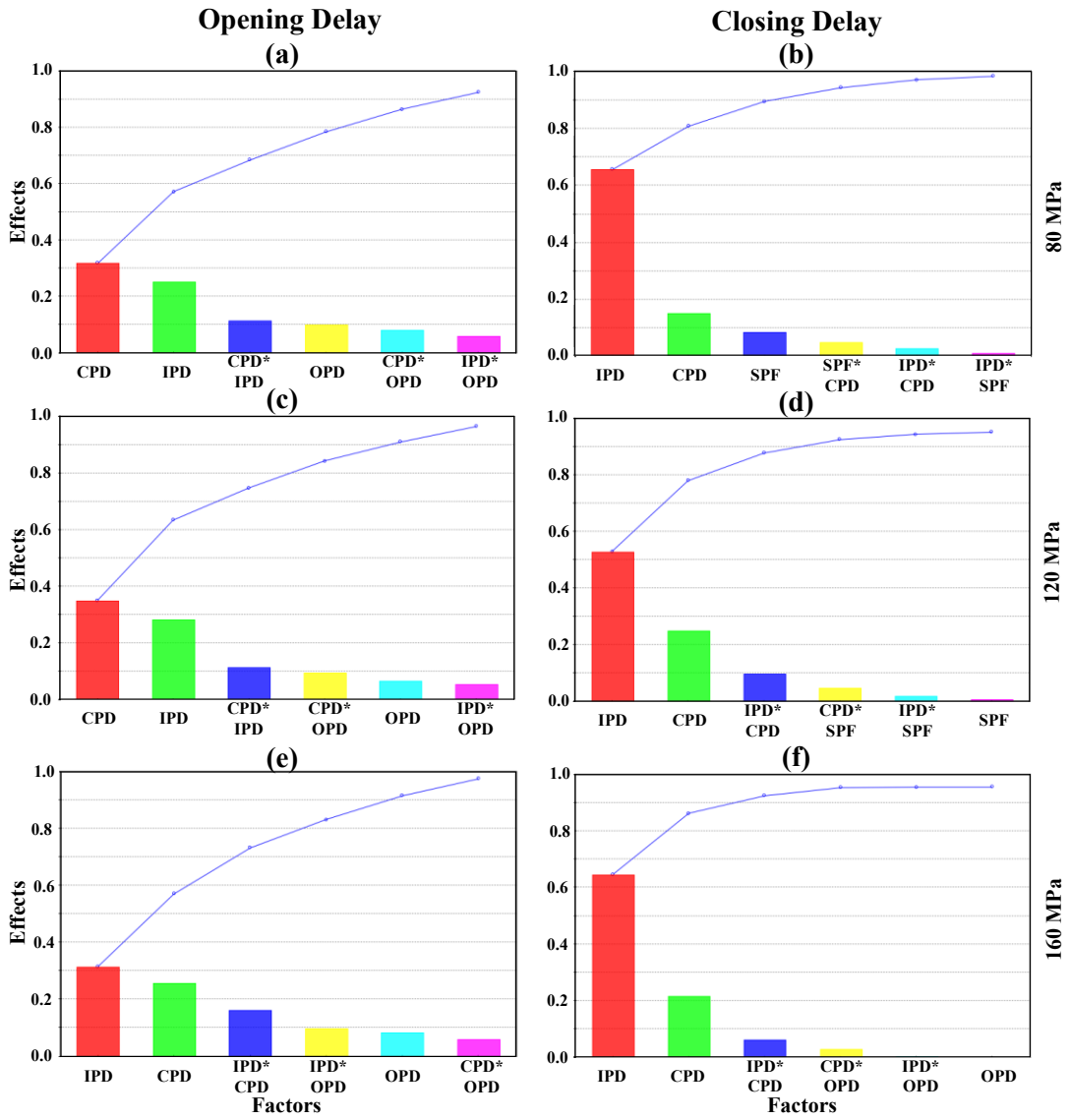

Figure 4-14 Sensitivity of structural parameters to the objectives. (a) Sensitivity of structural parameters to the opening delay at 80 MPa rail pressure; (b) Sensitivity of structural parameters to the closing delay at 80 MPa rail pressure; (c) Sensitivity of structural parameters to the opening delay at 120 MPa rail pressure; (d) Sensitivity of structural parameters to the closing delay at 120 MPa rail pressure; (e) Sensitivity of structural parameters to the opening delay at 160 MPa rail pressure; (f) Sensitivity of structural parameters to the closing delay at 160 MPa rail pressure.

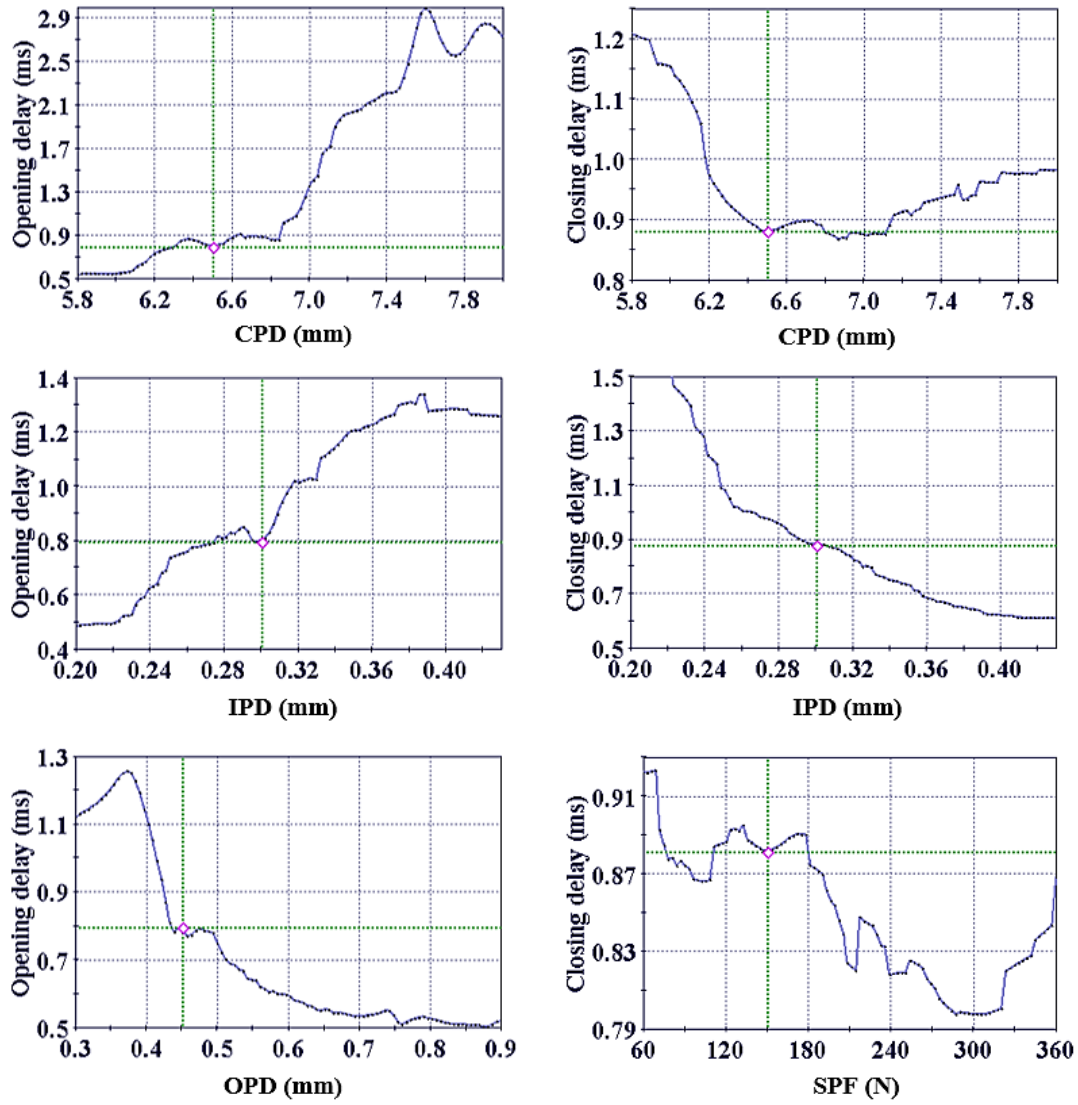

Figure 4-15 RSM function charts at 160 MPa rail pressure

4.4.2. Response surface analysis

Figure 4-14 highlighted the fact that CPD and IPD and their interactions are of greatest significance to the valve opening delay and the valve closing delay. The dynamic response of design parameters to the objectives were shown through RSM contour maps, and the dynamic response at 80 MPa and 120 MPa are almost the same as that of 160 MPa; therefore, only the dynamic response at 160 MPa was generated and demonstrated in Figure 4-16 and Figure 4-17. In both figures, the cross points of red lines and blue lines present the performance of the baseline design.

These RSM contour maps are also consistent with that of the Type-I fuel injector.

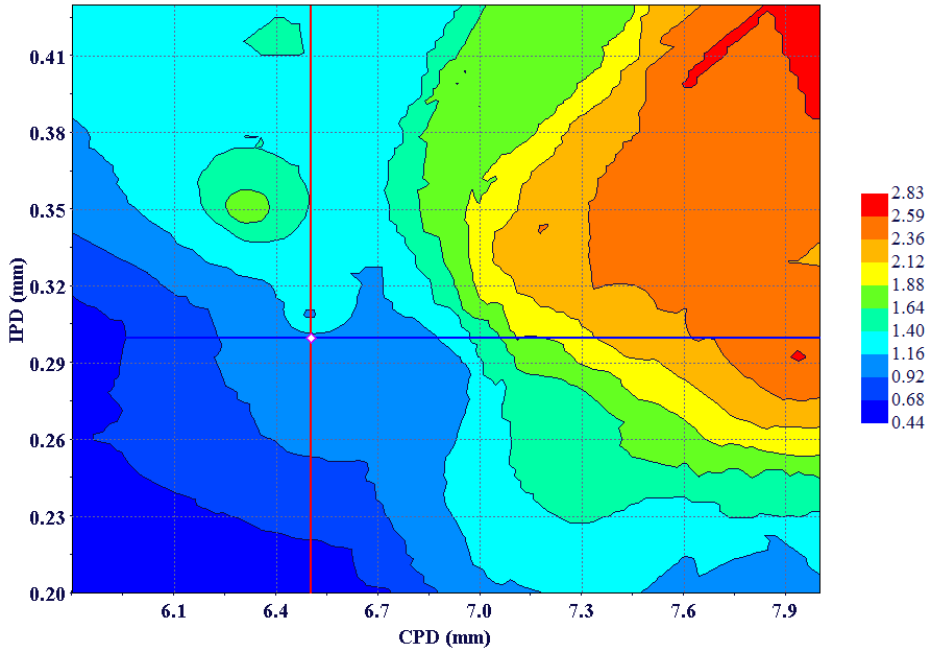

Figure 4-16 RSM contour map of the valve opening delay under 160 MPa rail pressure

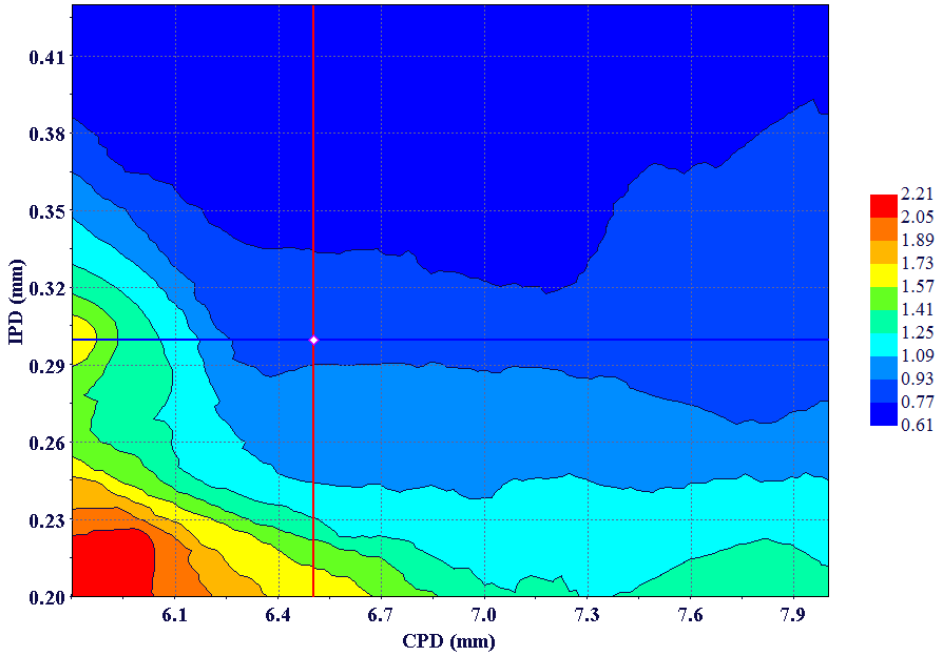

Figure 4-17 RSM contour map of the valve closing delay under 160 MPa rail pressure

4.4.3. Pareto optimum

Figure 4-18 (a), (b) and (c) are the optimisation results for three different rail pressures (80 MPa, 120 MPa and 160 MPa respectively). The Pareto optimums are marked with black solid triangles. The baseline design is marked with a blue square and the optimal design is shown as a green hollow triangle. The optimal design was selected from the Pareto results at 160 MPa (see Figure 4-18 (c)) and it performance was evaluated at the other two pressures (see Figure 4-18 (a) and (b)). Compared to the baseline design, both the valve opening delay and the valve closing delay of the optimal design have witnessed a huge reduction in all three rail pressures by 29.8%, 29.2% and 20.9% in the valve opening delay and 25.6%, 24.5% and 30.1% in the valve closing delay under the pressures of 80 MPa, 120 MPa and 160 MPa, respectively. The detailed information about the valve opening delay and valve closing delay of the optimum are listed in Table 4-7. In addition, the structural parameters of the baseline design and the optimal design are reported in Table 4-8. It can be seen that the control piston diameter reduces by 0.3 mm and the nozzle orifice diameter decreases by 0.4 mm. However, the control oil inlet passage, control oil outlet passage diameter and spring preload force increased to 0.39 mm, 0.9 mm and 290 N respectively.

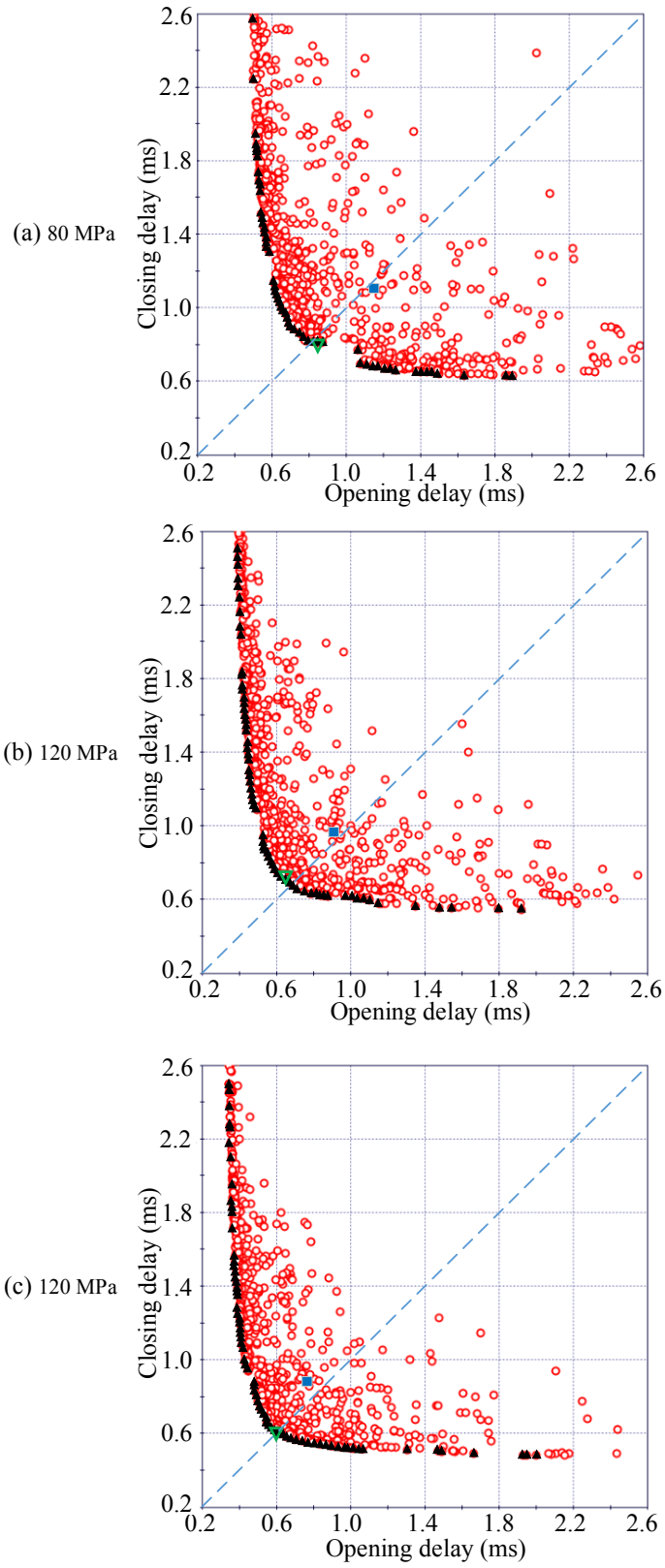

Figure 4-18 Pareto citizens and the selected designs under various rail pressures

Table 4-7 Detailed objective comparisons of the optimal and the baseline designs

Pressure (MPa)	Delay	Baseline (ms)	Optimum (ms)	Status	Degree （%）
80	Opening	1.197	0.840	↓	29.82
	Closing	1.097	0.816	↓	25.62
120	Opening	0.908	0.643	↓	29.19
	Closing	0.974	0.735	↓	24.54
160	Opening	0.767	0.607	↓	20.86
	Closing	0.880	0.615	↓	30.11

Table 4-8 Comparison of structure parameter values before and after optimisation

Parameter	Baseline	Optimum
Control piston diameter (mm)	6.5	6.2
Control oil inlet passage diameter (mm)	0.3	0.39
Control oil outlet passage diameter (mm)	0.45	0.90
Nozzle orifice number	9	9
Nozzle orifice diameter (mm)	0.27	0.23
Spring preload force (N)	149	290

The optimal design reaches the maximum boundary of the OPD, which implies the upper boundary for the OPD might be set too low. Thus, a further study on the OPD was carried out to examine its effects on injector dynamic response independently at the three rail pressures respectively. The results (see Figure 4-19) show that the valve closing delay remained almost unchanged, while the valve opening delay decreased monotonously with the increase in the OPD, but the trend became gentler when the OPD was larger than 0.6 mm. Therefore, extending the upper boundary of the OPD would be meaningless.

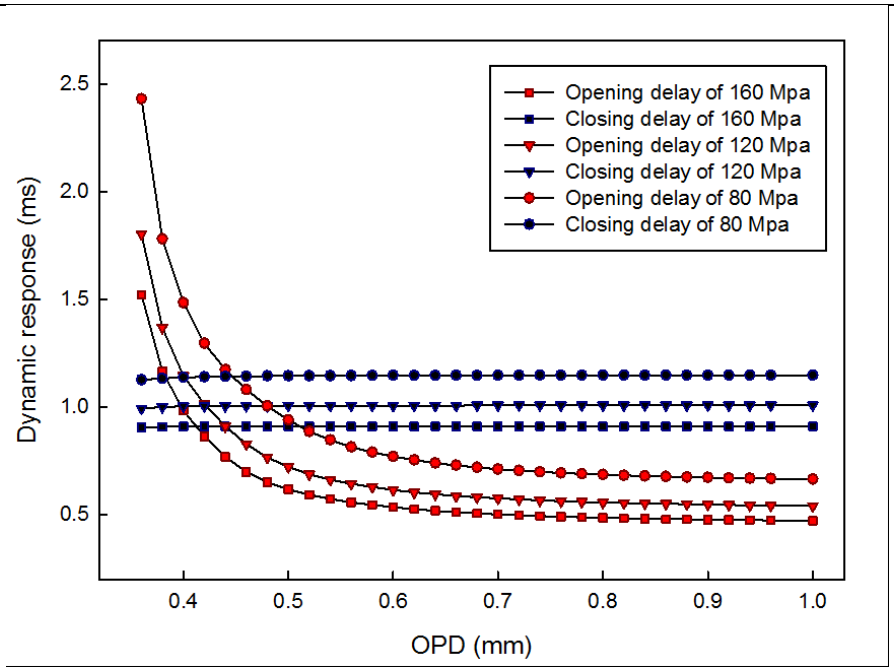

Figure 4-19 The effect of the OPD on injector dynamic response

The solenoid valve displacement and needle valve displacements of both the baseline design and the optimal design were compared under three different rail pressures, as shown in Figure 4-20. The injection rate is shown in Figure 4-21. In both figures, the needle valve displacements of the baseline design under different rail pressures are represented by black lines, while the needle valve displacements of the optimal design under various rail pressures are shown by red lines. Different rail pressures are distinguished by line types: 160 MPa, 120 MPa and 80 MPa are represented by solid lines, dashed lines and dotted lines respectively. The control signal, marked by blue lines, is also drawn in both Figure 4-20 and Figure 4-21 for reference. Since the nozzle orifice diameter of the optimal deign is smaller than that of the baseline design, the maximum injection rate is much less under the same activation time, as shown in Figure 4-21. Therefore, a larger rail pressure needs to be applied to retain the same injection mass for a specific engine with a fix periodical injection quantity.

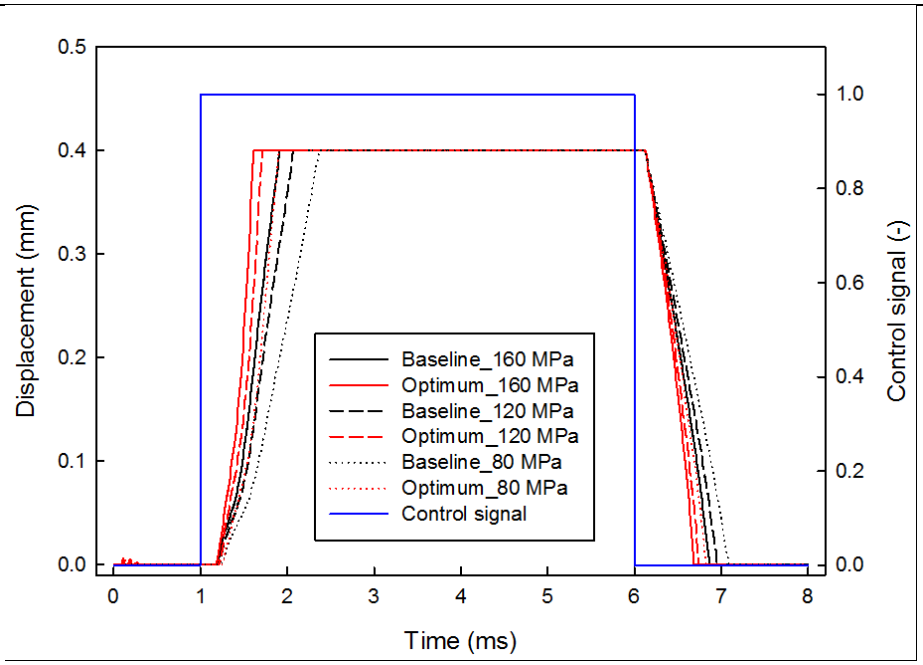

Figure 4-20 Needle valve displacement comparisons of the baseline and the optimal designs

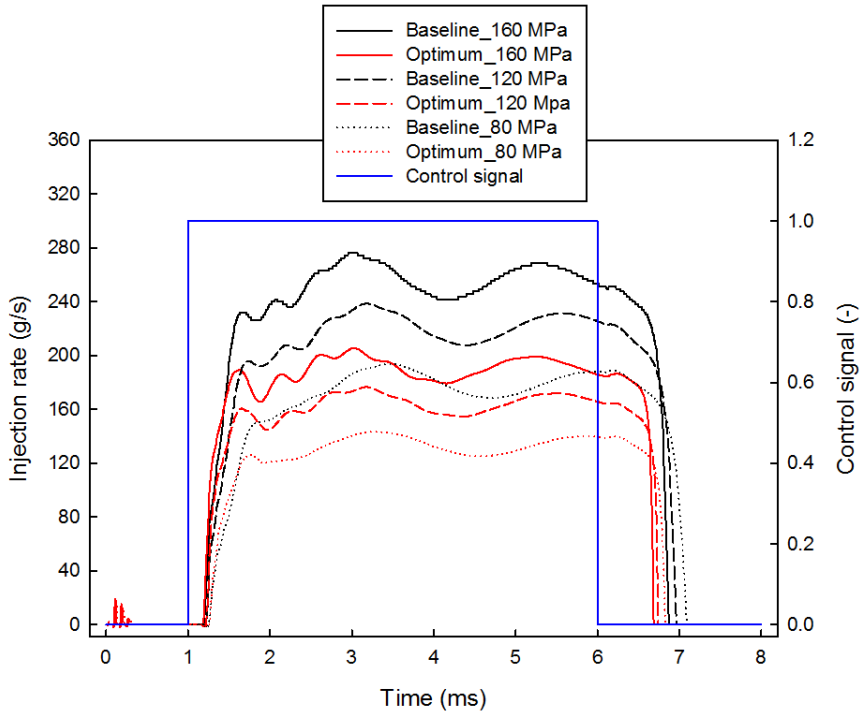

Figure 4-21 Injection rate of the baseline and the optimal designs under various rail pressures

4.5. Summary

The above discussion presented the modelling and optimisation of the structural parameters of the Type-II electronic fuel injector. A complete and detailed model of the electronic fuel injector was built using AMESim software. The model was validated by the experimental injection quantity data and average steady-state mass flow rate (if test condition permits, it is better to validate the injector model by injection quantity together with transient injection rate) obtained from a HIL test rig. Then, an optimisation routine was applied by using modeFRONTIER, and the optimisation was carried out through the MOGA method. The importance of the structural parameters of the dynamic response was examined. RSM function charts disclosed how these important structural parameters affect the dynamic response. Then, RSM contour maps were applied to study the interactions between the CPD and IPD. Finally, a Pareto optimal design with the best trade-off between the valve opening delay and the valve closing delay was singled out.

The main conclusions are below:

(1) The sensitivity analysis shows that the control piston diameter, control oil inlet passage diameter, control oil outlet passage diameter and their interactions are influential factors for the valve opening delay, while the control oil inlet passage diameter has a dominant effect on the valve closing delay. If the same circulation area is guaranteed, the nozzle orifice diameter and nozzle orifice number have less impact on the dynamic response than the control piston diameter, control oil inlet passage diameter and control oil outlet passage diameter.

(2) The RSM function charts and the RSM contour maps disclosed that the influence of the control piston diameter, control oil inlet passage diameter and control oil outlet passage diameter of the Type-II fuel injector on the dynamic response is consistent with that of the Type-I fuel injector (see Section 3.6). In addition, they also indicated that the effects of the spring preload force on the valve closing delay are surprising noticeable under low rail pressure conditions. The valve closing delay decreases with

the increase in the spring preload force.

(3) The dynamic response of the optimal design achieves a considerable reduction for three different rail pressures (80 MPa, 120 MPa and 160 MPa). More specifically, the valve opening delay was reduced by 29.8%, 29.2% and 20.8%, and the valve closing delay was reduced by 25.6%, 24.5% and 30.1% respectively.

Chapter 5. CFD simulation models and verification

The previous chapters presented the first part of the thesis, which studied the effects of the structural parameters of Type-I and -II fuel injectors on their dynamic response. One of the fuel injectors, the Type-II fuel injector, was selected for a match study with a combustion chamber of a medium-speed marine diesel engine. This chapter introduces the mesh generation, calculation step and simulation models at the CFD engine model. Finally, this model was validated by using pressures and NO_x emissions under four typical engine loads.

5.1. Engine specification

The marine medium speed engine to be modelled is the MAN 6L 16/24, its main geometric specifications are presented in Table 5-1. It is an in-line, 6-cylinders, 4-stoke diesel engine. Its rated operating point at 1000 rpm produces power of 540 kW respectively. The spray orifice distribution of the original mechanical fuel injector is 9*0.28 mm; when the mechanical fuel oil injection system is replaced by an HPCR fuel oil injection system with a new electronic fuel injector, it changes to 9*0.23 mm the optimum obtained from the study of Chapter 4.

Table 5-1 Specifications of the engine and fuel injector

Feature	Value
Engine name	MAN 6L16/24
Cylinder arrangement	In-line
Number of stroke	4
Bore(mm)	160
Stroke(mm)	240
Number of cylinders	6
Rated speed (r/min)	1000
Rated power (kW)	540
SFOC (g/(kW•h))	189
Compression ratio	15.2
Original mechanical injector	9 X 0.28 mm
Electronic fuel injector	9 X 0.23 mm

5.2. Mesh generation and validation

There are two basic grid types of mesh: the structured grid and the unstructured grid. A structured grid means that its adjacencies obey the rule that each surface grid is quadrilateral and each volume grid is a hexahedron. However, an unstructured grid's adjacencies are uncertain: they can be triangles or quadrilateral for surfaces, and tetrahedrons, hexahedrons or triangular prisms for volumes. An irregular and random unstructured grid increases the computer's search time. A structured grid is more time and memory saving than an unstructured grid because fewer hexahedral cells are needed to fill a volume. Moreover, it is easier to generate high quality cells on a hex grid than on a highly stretched tetrahedral grid; thus, a more accurate resolution can be realised on a structured grid. A structured grid is also beneficial for its alignment, which provides a better converge and accuracy for CFD solvers. Based on the above details, a structured grid was generated in the CFD calculation in this paper [84,85].

The independency of the mesh and cell number was shown in Figure 5-1. Three mesh resolutions including a coarse mesh of 75 K cells, a medium mesh with 125 K cell and a fine mesh with 175 K cells were applied. It can be seen that the medium mesh with a total of 125 K cells gives similar results with the fine mesh without taking too much computational time.

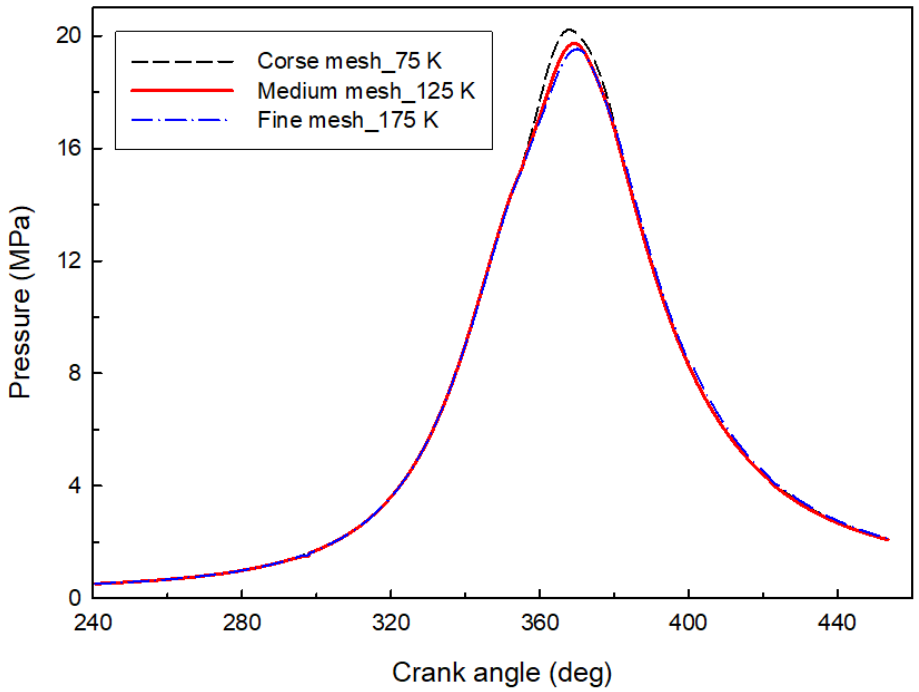

Figure 5-1 Mesh independency

The mesh of the combustion chamber was divided into eight groups: 0 deg CA-18.8 deg CA, 18.8 deg CA-24.4 deg CA, 24.4 deg CA-64.5 deg CA, 64.5 deg CA-180 deg CA, 180 deg CA-295.5 deg CA, 295.5 deg CA-335.6 deg CA, 335.6 deg CA-341.2 deg CA and 341.2 deg CA-360 deg CA. In each group, mesh was stretched to every calculation point. Figure 5-2 shows the mesh cuts for the calculation at 0 deg CA, 64.5 deg CA and 180 deg CA. The number of cells are 4,063, 6,329 and 15,833, respectively.

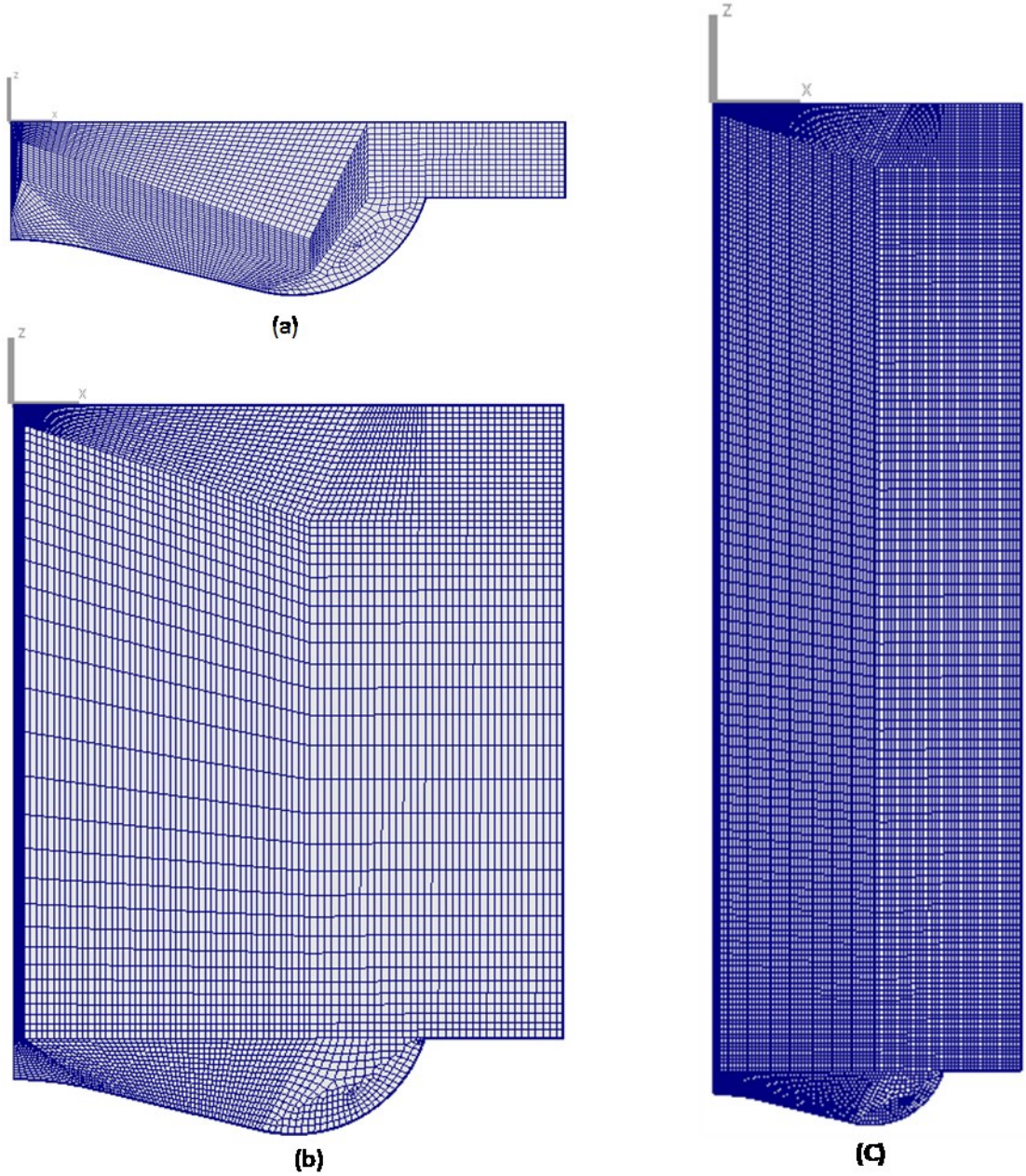

Figure 5-2 Mesh generation demonstration, (a) 0 deg CA, (b) 64.5 deg CA, (c) 180 deg CA

5.3. Simulation modelling of in-cylinder process

The simulation of the in-cylinder process was carried out from the moment of intake valve closing to the moment of the exhaust valve opening.

5.2.1. Basic conservation equations

(1) Mass conservation equation:

$$\frac{\partial \rho}{\partial t} + \frac{\partial}{\partial x_j}(\rho u_i) = 0 \tag{5.1}$$

Where: ρ is density, u_i is the velocity component on x_i, and t is time.

(2) Energy conservation equation:

$$\frac{\partial \rho h}{\partial t} + \frac{\partial}{\partial x_j}(\rho h u_j + F_{hj}) = \frac{\partial p}{\partial t} + u_j \frac{\partial p}{\partial x_j} + \tau_{ij} \frac{\partial u_i}{\partial x_j} + s_h \tag{5.2}$$

$$h = \overline{c_p} T - c_p^0 T_O + \sum Y_m H_m = h_t + \sum Y_m H_m \tag{5.3}$$

Where: h is the sum of heat enthalpy and chemical reaction enthalpy, T is the temperature, Y_m is the mass fraction of component m, H_m is the heat generated by component m, $\overline{c_p}$ is the average specific heat under constant pressure while temperature is T, c_p^0 is the specific heat when temperature is T_O, F_{hj} is the enthalpy diffusion flux on x_j direction, s_h is the energy source component, and h_t is the heat enthalpy.

(3) Momentum balances equation:

$$\rho \frac{\partial u_i}{\partial t} + \frac{\partial}{\partial x_j}(\rho u_j u_i - \tau_{ij}) = -\frac{\partial p}{\partial x_i} - s_i \tag{5.4}$$

Where: p is the pressure, s_i is the momentum source component, and τ_{ij} is the tensor component.

(4) Gas state equation:

$$P = \rho R_u T \sum_{m=1}^{N} \frac{Y_m}{M_m} \tag{5.5}$$

Where: M_m is the molecular molar mass of composition m, and Y_m is the mass fraction of m.

5.2.2. Simulation modelling

The modelling of the target marine diesel engine was applied in FIRE ESE Diesel software. In it, the k-zeta-f [86, 87] turbulent model for high Reynolds numbers is adopted to describe the flow field inside a combustion chamber. The computations run with MINMOD relaxed scheme for the momentum equation and the central differencing is applied for the continuity. Stand wall function was supposed to be appropriate to describe heat transfer of wall. Piso algorithm [88, 89] is adopted here to solve the highly unsteady-state flow of the combustion problem. In terms of the fuel spray model, the Dukowicz model [90] with assumption that the droplet evaporation is in a non-condensable gas was applied for handling the heat-up and evaporation of the fuel oil droplets. Moreover, the droplet breakup was described by Wave break-up model [91, 92]. The wall interaction was described by Walljet1[93, 94], in which sliding and rebound of the spray particles are determined by the critical Weber number of We_c=80. The Eddy break-up model [95, 96] is introduced in the calculation of combustion. Regarding emission models, an extended Zeldovich [97] mechanism was adopted for the NO_x emission model while a Kinetic mechanism was used for the soot emission model [98, 99, 100].

5.2.3. Calculation step settings

In order to improve the convergence at the beginning of the simulation, the initial calculation step is set to be at 0.2 deg CA. Then, 1 deg CA is adopted at compression stoke to accelerate the calculation and save time. However, at injection stage,

precision is emphasized, so the step is reduced to 0.2 deg CA again. In afterburn stage, 0.5 deg CA is adopted.

5.4. Model verification

Model verification was executed at four different engine loads, i.e. L25, L50, L75 and L100 loads, respectively. The comparisons of the cylinder pressures and rate of heat release between the simulation data and test data under four loads are shown in Figure 5-3. In the figure, the experimental cylinder pressure data were represented by black circles, the simulation pressure date were represented by red lines, the experimental ROHR is represented by blues circles, and the simulation ROHR is represented by purple lines. It can be seen that a good agreement of simulation data and experimental data is achieved, especially cylinder pressures at the stage of combustion. In the stage of compression and expansion, cylinder pressure simulation data were a slightly greater than test data, that's because the pressure losses by leakage were not considered in this simulation model, while these losses do exist in authentic diesel engines.

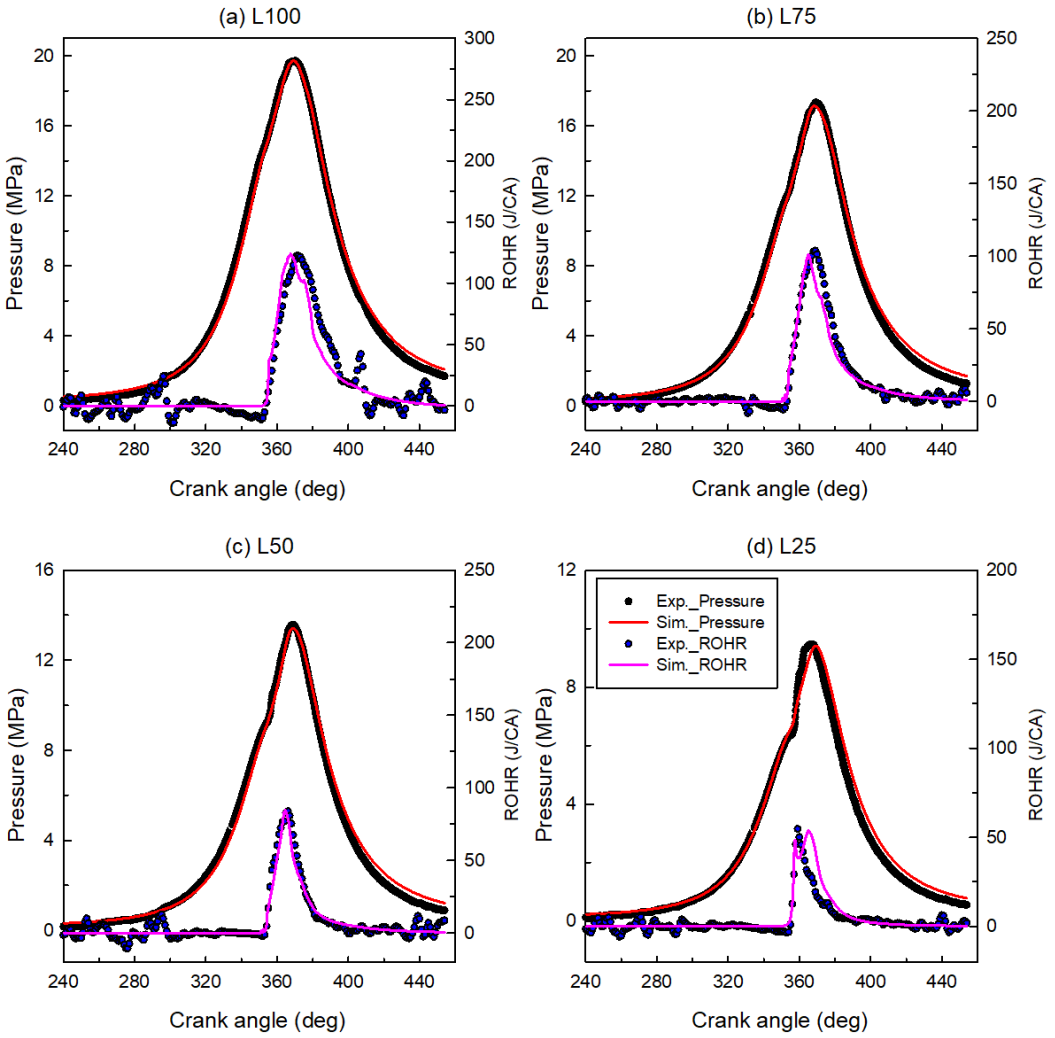

Figure 5-3 Pressure and ROHR comparisons of experimental data and simulation data under four engine loads

The NO_x emissions are also examined and compared at each engine load. The NO_x experimental data was provided by an engine producer, who performed the test under the standard D2 test cycle. Results comparisons were shown in Figure 5-4, the main trend of simulation results corresponds to the experimental data. The maximum error occurred at full load which is less than 6.5%.

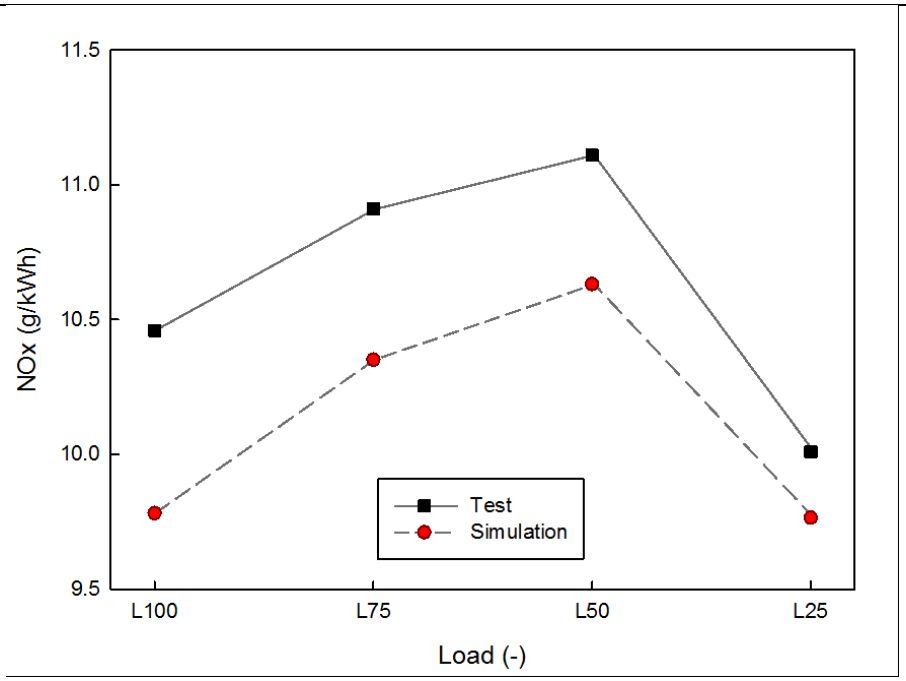

Figure 5-4 NO_x emission comparison of test data and simulation data under four engine loads

The validation process indicates that the model can be used to simulate and predict the engine performance when replacing the original mechanical fuel oil injection by a high-pressure common rail injection system. The engine body with the high-pressure common rail fuel oil injection system is defined as the baseline engine, which kept the match parameters the same as the original one.

5.5. Summary

In this chapter, mesh generation was briefly introduced. Equations and models used in the FIRE simulation model were presented in detail. The developed model was verified by cylinder pressure, ROHR and NO_x emissions under four engine loads. The simulation data show good agreement with experimental data; thus, the model can be used to predict engine emission and performance.

Chapter 6. Parametric study of injection-related parameters and combustion chamber geometries

Simulations were conducted using the AVL FIRE software. Firstly, a combustion chamber at the TDC moment was drawn in FIRE 2D Sketcher according to the shape of the upper surface of the piston and the clearance distance between the piston surface and the cylinder head. Secondly, the design combustion chamber geometries were loaded in the FIRE ESE Diesel software in order to build a CFD model. Once the CFD model in FIRE ESE Diesel is validated, it can be used for the parametric study and the multi-objective study. In the parametric study, the selected design parameters were varied with five values under three different engine loads. In the multi-objective study, the CFD model was loaded into the FIRE DVI, where the calculation settings were specified. Then, the FIRE Design Explorer was included, where the design variables and their variation ranges, objectives, constraints and algorithms were defined or selected. Finally, the combustion images were processed in FIRE Workflow Manager. The complete scheme of the software used in the study is shown in Figure 6-1.

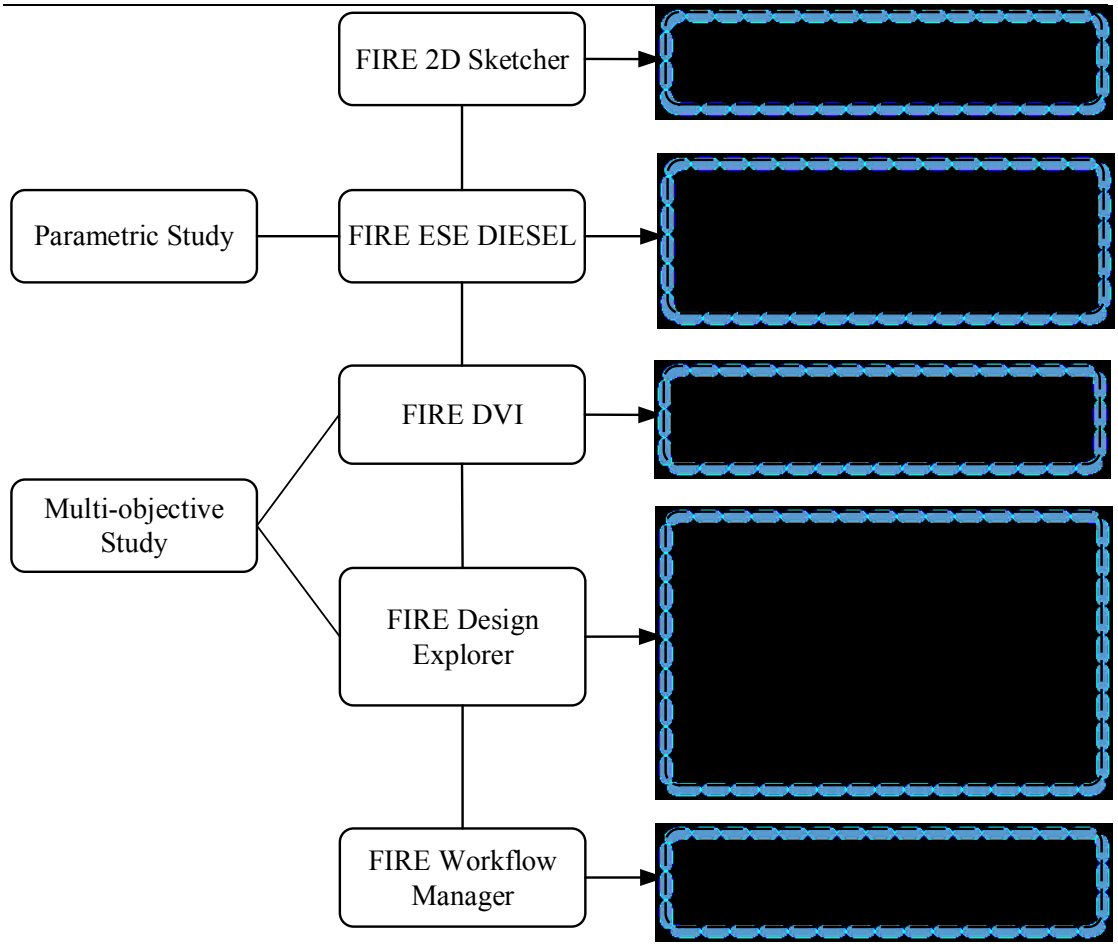

Figure 6-1 Scheme of the optimisation process

In the parametric study, four injection-related parameters (the spray angle, nozzle protrusion length, injection timing and swirl ratio), plus three combustion chamber geometries (the bowl diameter, centre crown height and toroidal radius) are selected for analysis. The lower and upper boundaries of these parameters are listed below, they were chosen via a trial study.

Table 6-1 Variation ranges of parameters used for independent parameter analysis and optimisation

Parameters	Code	Baseline	Lower boundary	Upper boundary	Step
Injection timing, deg BTDC	SOI	10	20	0	5
Swirl ratio	SR	1	0.5	2.5	0.5
Spray angle, deg	SA	143	131	155	6
Nozzle protrusion length, mm	NPL	2.5	1.0	4.0	0.75
Toroidal radius, mm	r002	20	18	22	1
Centre crown height, mm	v003	6	5	9	1
Bowl diameter, mm	h001	120	108	132	6

In the parametric study, only one parameter changes at a time, while the other parameters remain with the baseline values. Each parameter was assessed under three common loads. For the change of combustion chamber parameters, it is impossible to keep the compression ratio the same when changing one combustion chamber geometry without changing another parameter, so TDC clearance is changed automatically to maintain the same volume and consequently keep the combustion ratio the same. Additionally, the unit of NO_x emissions, soot emissions and SFOC are converted from mass fraction to g/kWh, in which process the total injection mass and indicated power are used.

6.1. Spray angle

The demonstration of the spray angle variation is shown in Figure 6-2. The blue line and the purple line indicate the lower boundary and the higher boundary of the spray angle respectively; the red line indicates the baseline spray angle.

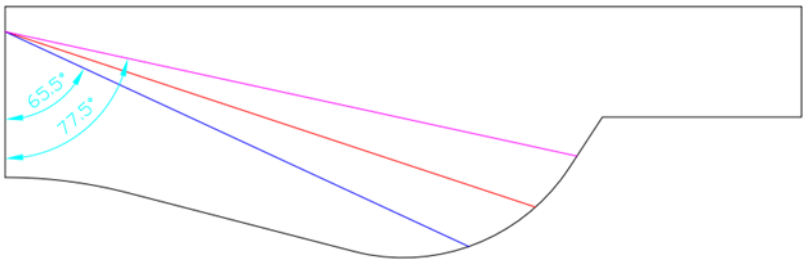

Figure 6-2 Demonstration of the spray angle variation range

The results of spray angle variation are shown in Figure 6-3. NO_x emissions, soot emissions and SFOC were distinguished by line types, i.e., dashed lines for NO_x emissions, solid lines for soot emissions and dotted lines for SFOC. The NO_x emissions, soot emissions and SFOC under L50, L75 and L100 loads were represented by blue triangles, yellow diamonds and red circles, respectively. The same rules apply in figures of following sections. From Figure 6-3, it can be inferred that NO_x emissions increase in line with the increase in the spray angle, while soot and SFOC reduce at the same time. The reasons can be derived by using the results shown in the Figure 6-4, Figure 6-5 and Figure 6-6. The equivalence ratio in Figure 6-6 is the fuel-air ratio, which indicates the density of fuel. From Figure 6-6, it can be seen that when the spray angle is at 131 degrees, most of the fuel was injected into the bowl area and adhered to the surface of the piston. This is unfavourable for the NO_x formation, particularly when the piston is going downward and the volume of the combustion chamber expands and the temperature reduces. Most of the fuel did not burn completely and was exhausted in the form of soot emissions, which explains the higher soot emissions and the deteriorated fuel economy, as opposed to the results obtained at any angles. This alleviates with the increase in the spray angle,

particularly when the injection angle increases to 155 degrees, where the fuel is effectively distributed between the bowl area and the clearance area. A reduced fuel density and an enhanced fuel vaporisation contribute to a more homogeneous fuel distribution. On the one hand, this is the main reason for the low soot emissions and SFOC; on the other hand, the homogeneous fuel oil distribution leads to a higher rate of heat release (as shown in Figure 6-4) and a resulting higher temperature (as shown in Figure 6-5) also results in higher NO_x emissions.

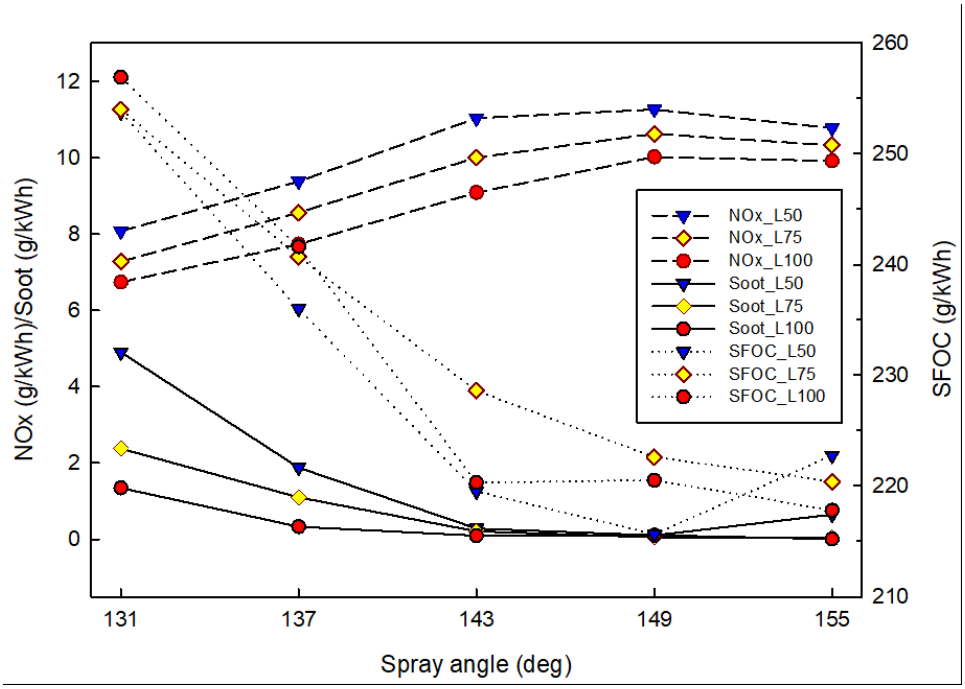

Figure 6-3 Influence of various spray angles on NO_x emissions, soot emissions and SFOC

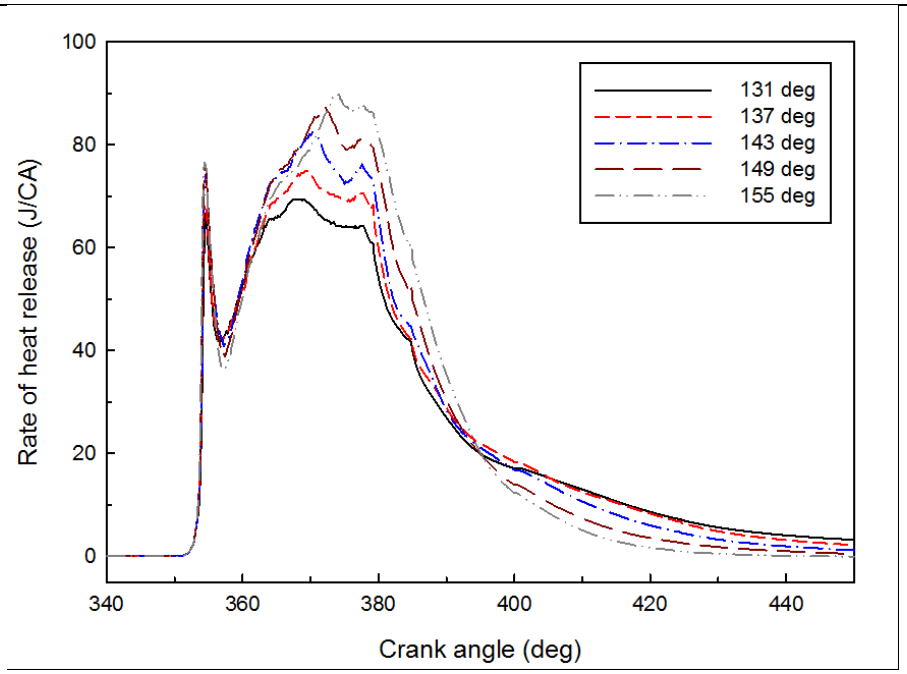

Figure 6-4 Influence of various spray angles on rate of heat release

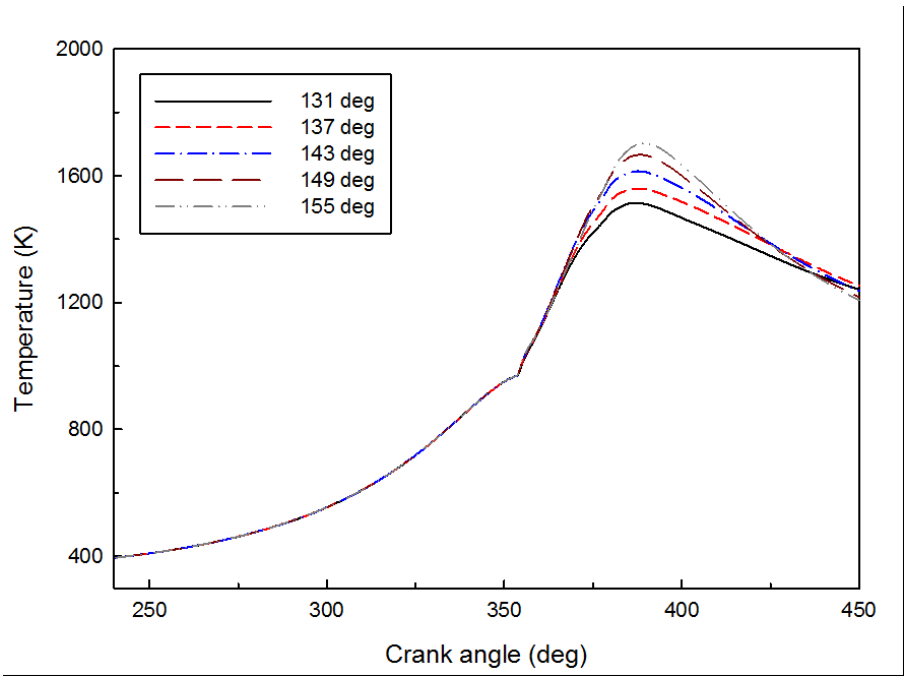

Figure 6-5 Influence of various spray angles on temperature

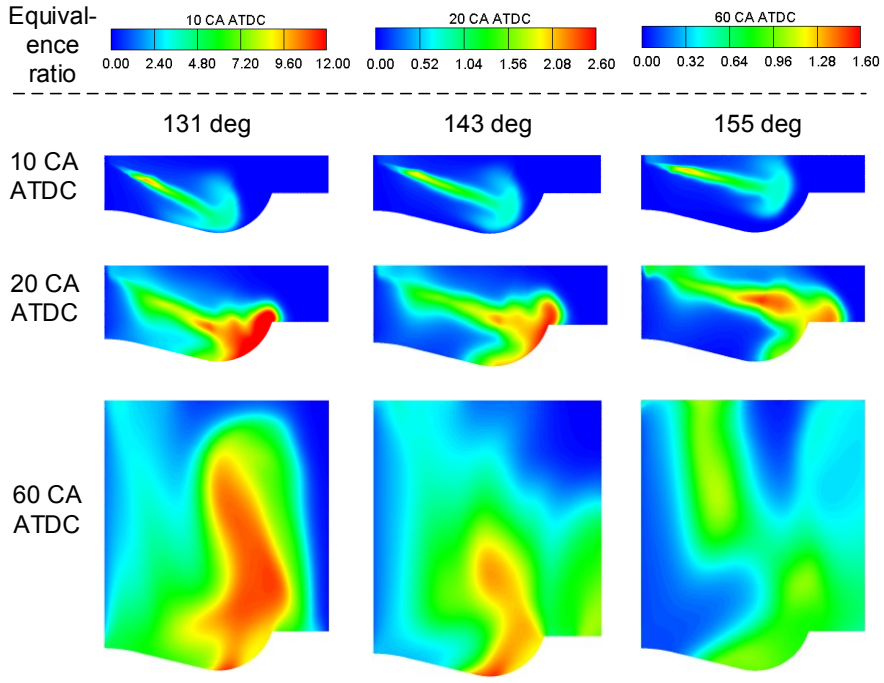

Figure 6-6 Influence of various spray angles on combustion

6.2. Nozzle protrusion length

From Figure 6-7, it can be seen that the NO_x emissions decrease with an increase in the nozzle protrusion length. In addition, a larger drop is seen at L50 engine load with an increase in the nozzle protrusion length than that at high engine loads (L75 and L100). In contrast, soot emissions and SFOC increase with an increase in the nozzle protrusion length. This is because with the injection spray then targets the bottom area of the bowl, as shown in Figure 6-10. From this point, the effect of increasing the nozzle protrusion length is identical to decreasing the injection angle. More specifically, the distance between the injector and the piston surface exposed to the injection direction becomes shorter, which means that more liquid fuel hits and adheres to the surface of the piston bowl. This can be proved by Figure 6-10. The liquid fuel on the piston surface is difficult to burn completely resulting in soot emissions. Therefore, increasing the nozzle protrusion length increases the soot emissions and the SFOC. In contrast, a low rate of heat release (as shown in Figure 6-8) was resulted from the incomplete combustion and led to a low temperature (as

shown in Figure 6-9), which suppressed NO_x formation in the combustion process. This explains the low NO_x emissions when the nozzle protrusion length is large.

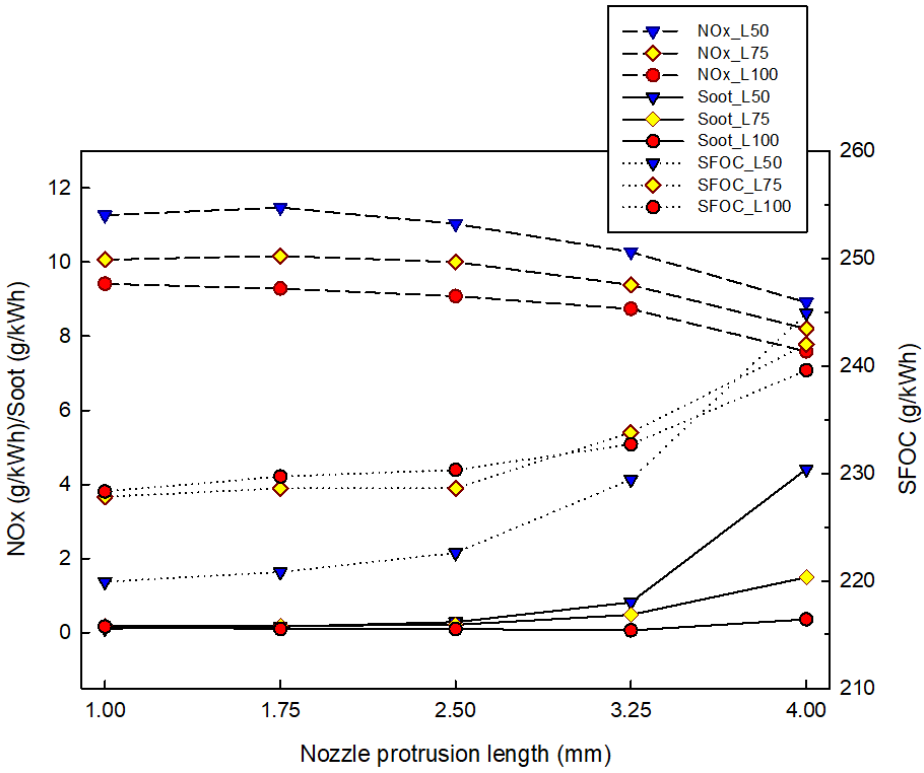

Figure 6-7 Influence of various nozzle protrusion lengths on NO_x emissions, soot emissions and SFOC

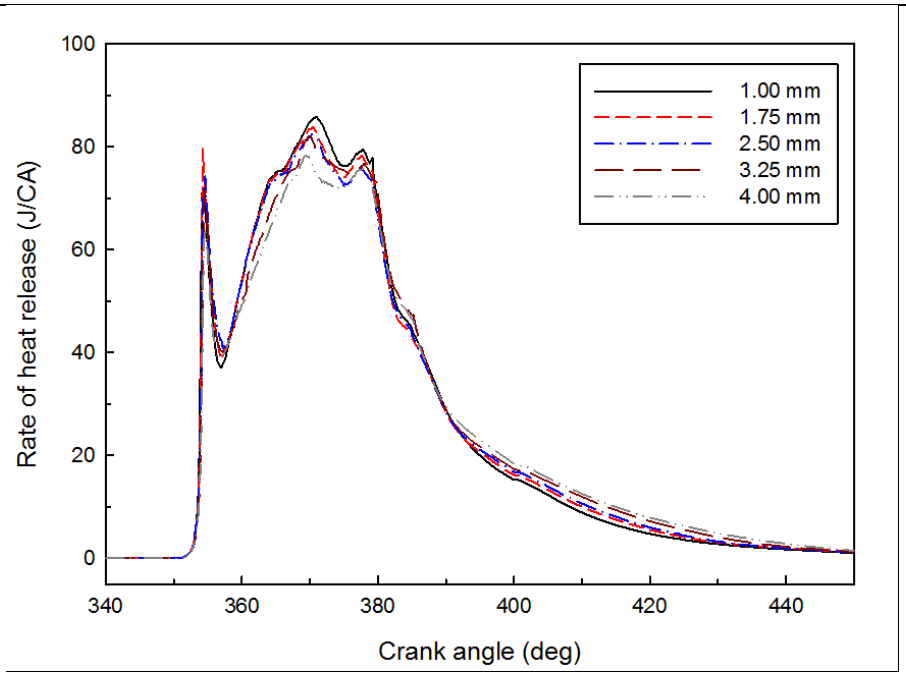

Figure 6-8 Influence of various nozzle protrusion lengths on rate of heat release

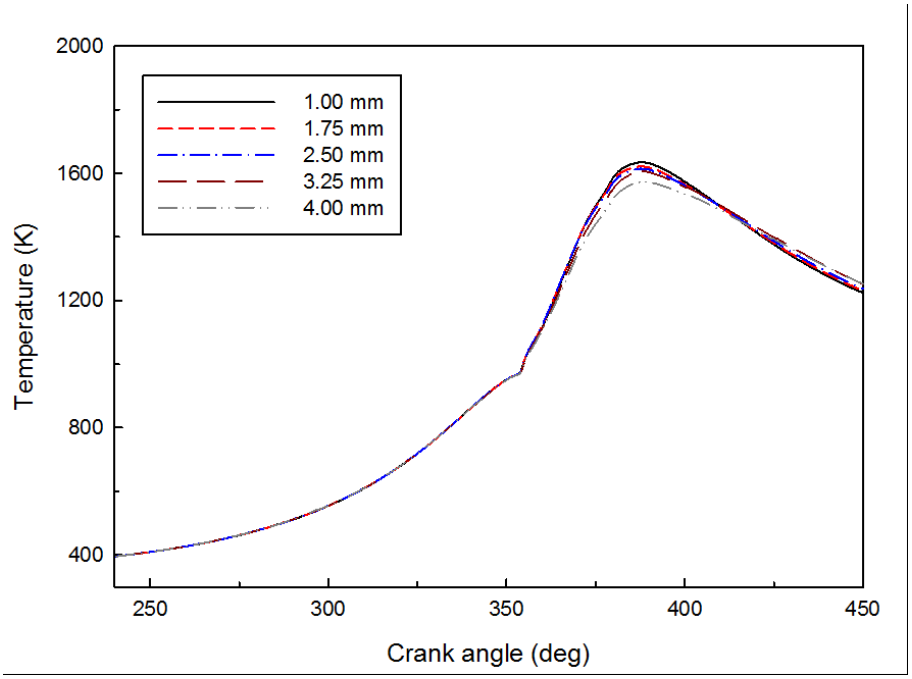

Figure 6-9 Influence of various nozzle protrusion lengths on temperature

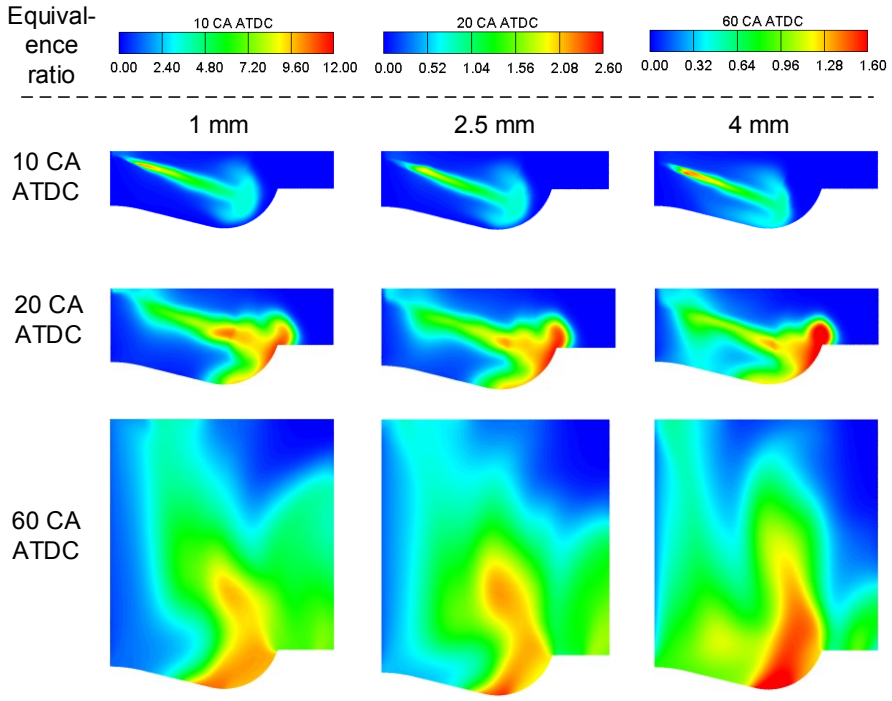

Figure 6-10 Influence of various nozzle protrusion lengths on combustion

6.3. Injection timing

From Figure 6-11, it can be seen that the injection timing has the most significant influence on the NO_x emissions, soot emissions and SFOC. Specifically, with an increase in injection timing (referring to the start of injection BTDC), a consistently increasing trend of the NO_x emissions is observed. In contrast, an opposite decreasing trend is observed in the case of the SFOC. The NO_x emissions at an injection timing of 20 degrees BTDC are approximately three times higher than that at the TDC. The SFOC decreases by nearly 20% from the TDC to 20 degrees BTDC. For soot emissions, they decrease slightly with an increase in the injection timing. The details and reasons can be derived from Figure 6-12, Figure 6-13 and Figure 6-14. When the injection occurs at 20 degrees BTDC, the time for fuel vaporisation and fuel-air mixing is increased which results in fierce combustion and a high temperature, as shown in Figure 6-12 and Figure 6-14. A high temperature leads to a high amount of NO_x emissions, as shown in Figure 6-13. More time for mixing is

beneficial for a complete combustion, which is helpful to achieve a high fuel economy and a low SFOC. On the contrary, soot emissions decrease in line with the increase in injection timing, due to the fact that a complete combustion helps reduce soot formation.

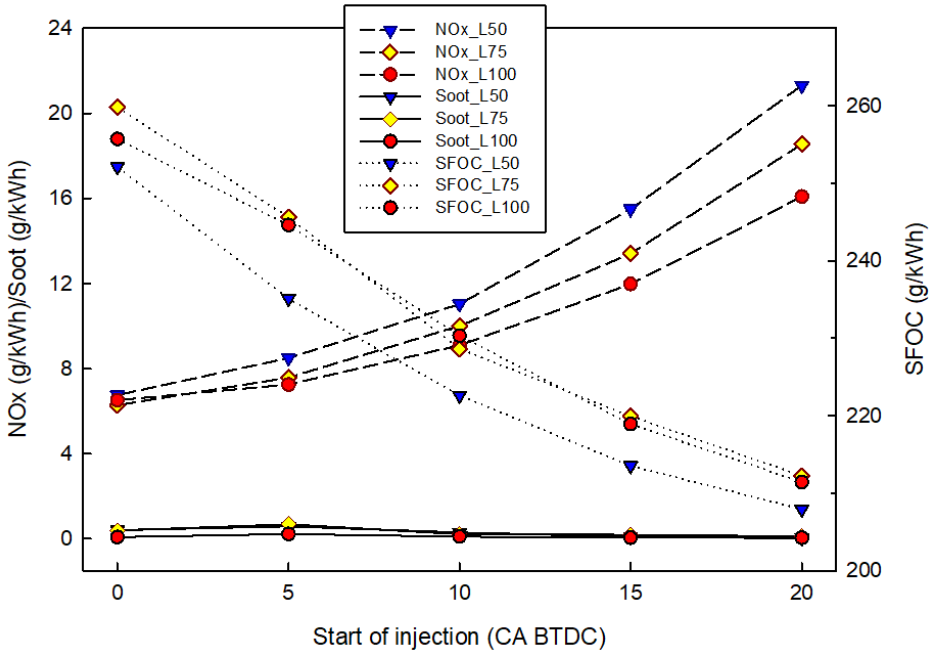

Figure 6-11 Influence of various values of start of injection on NO_x emissions, soot emissions and SFOC

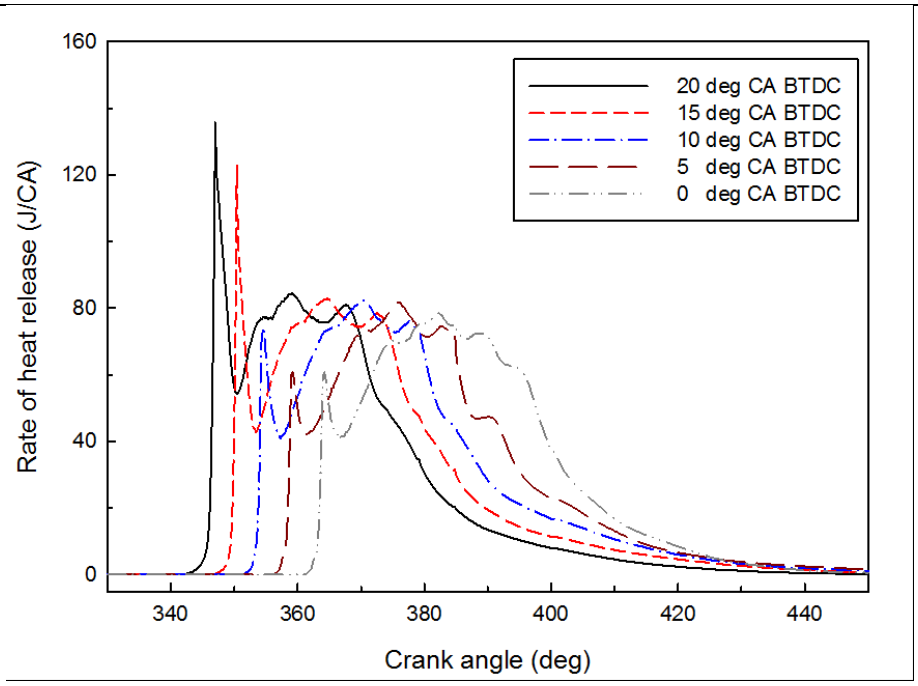

Figure 6-12 Influence of various values of start of injection on rate of heat release

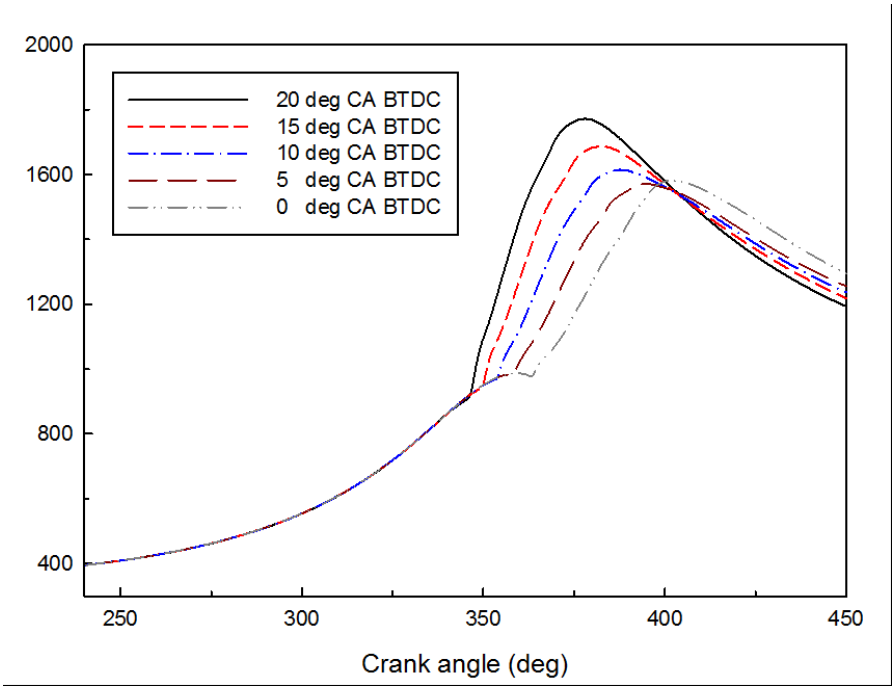

Figure 6-13 Influence of various values of start of injection on temperature

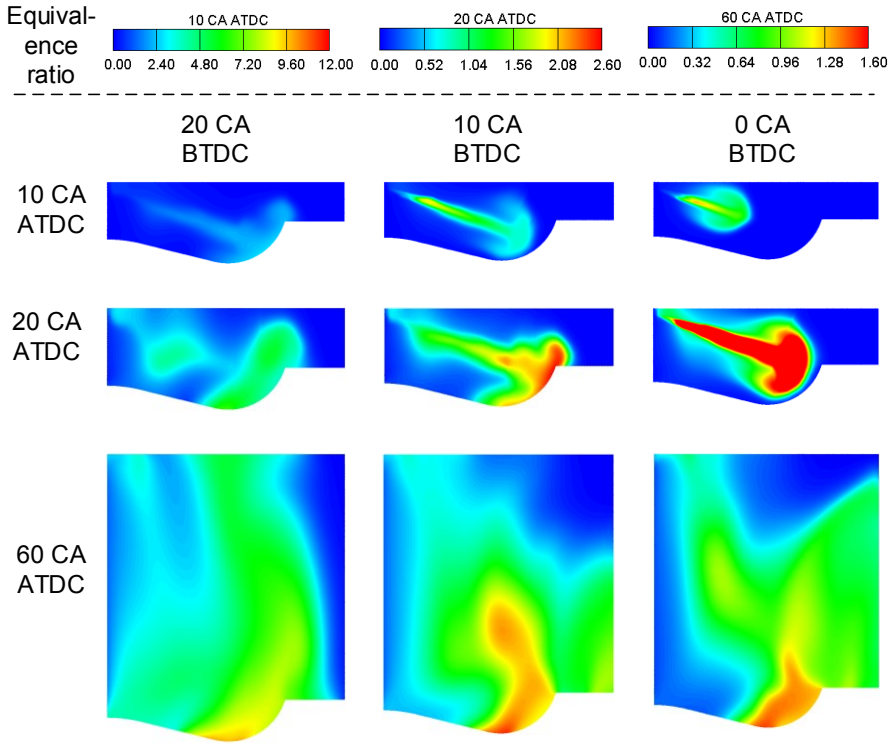

Figure 6-14 Influence of various values of start of injection on combustion.

6.4. Swirl ratio

The effects of swirl ratio on the emissions and fuel consumption are also not negligible. From Figure 6-15, the NO_x emissions increase in line with an increase in the swirl ratio at high loads (L75 and L100 loads). For soot emissions and SFOC, increasing trends are observed as the swirl ratio increases. From the first row of Figure 6-18, it can be seen that a strong swirl will reduce fuel penetration, i.e. the swirl ratio of 0.5 has the longest fuel penetration while the 2.5 has the least. This is explained that on 20 CA ATDC, a large amount of fuel hit the surface of the piston bowl in the low swirl case. In contrast, high swirl contributes to better mixing at the early stage of combustion. This leads to a higher rate of heat release and temperature, as shown in Figure 6-16 and Figure 6-17. High temperatures promote the formation of NO_x. This explains the slightly higher NO_x emissions in the high swirl case. However, there is still a high density of fuel at 60 CA ATDC. The liquid fuel adhered

to the surface of piston cannot be burned, and is exhausted as soot, which also leads to high soot emissions. Since the liquid fuel were not burned completely, a high SFOC was found.

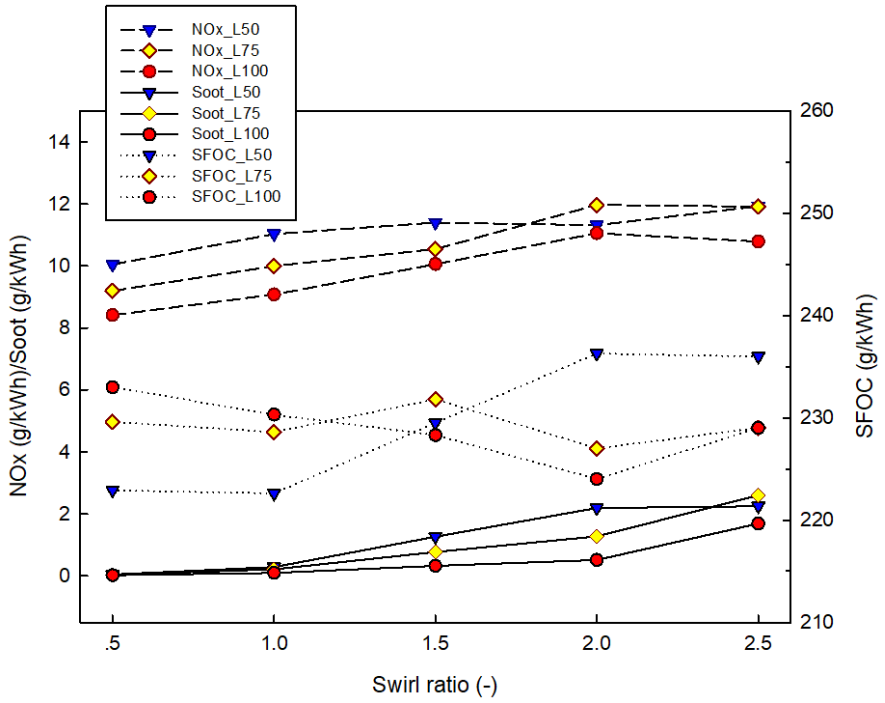

Figure 6-15 Influence of various swirl ratios on NO_x emissions, soot emissions and SFOC

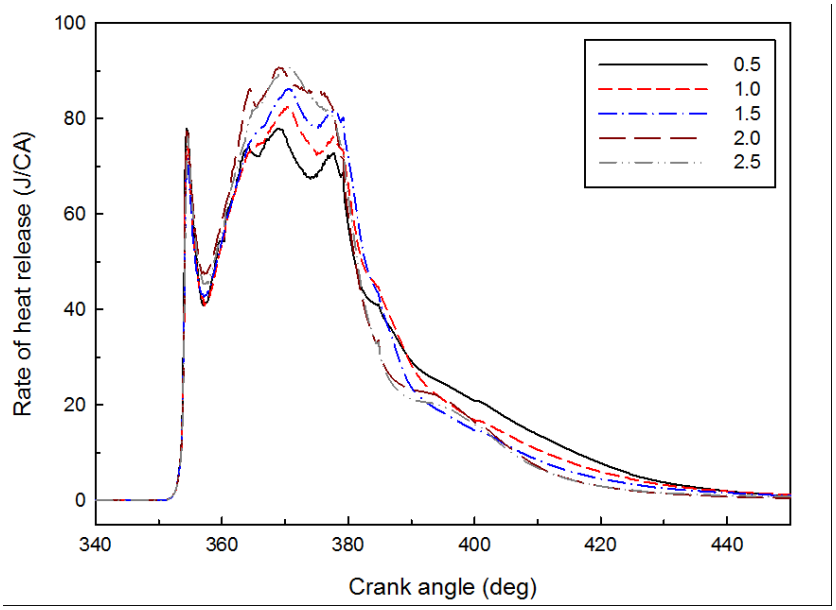

Figure 6-16 Influence of various swirl ratios on rate of heat release

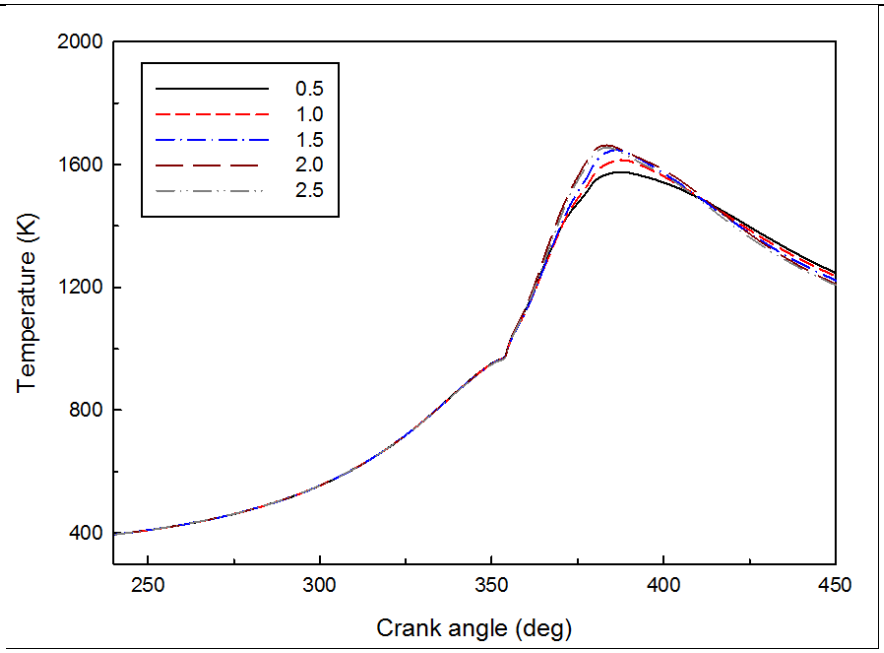

Figure 6-17 Influence of various swirl ratios on rate of temperature

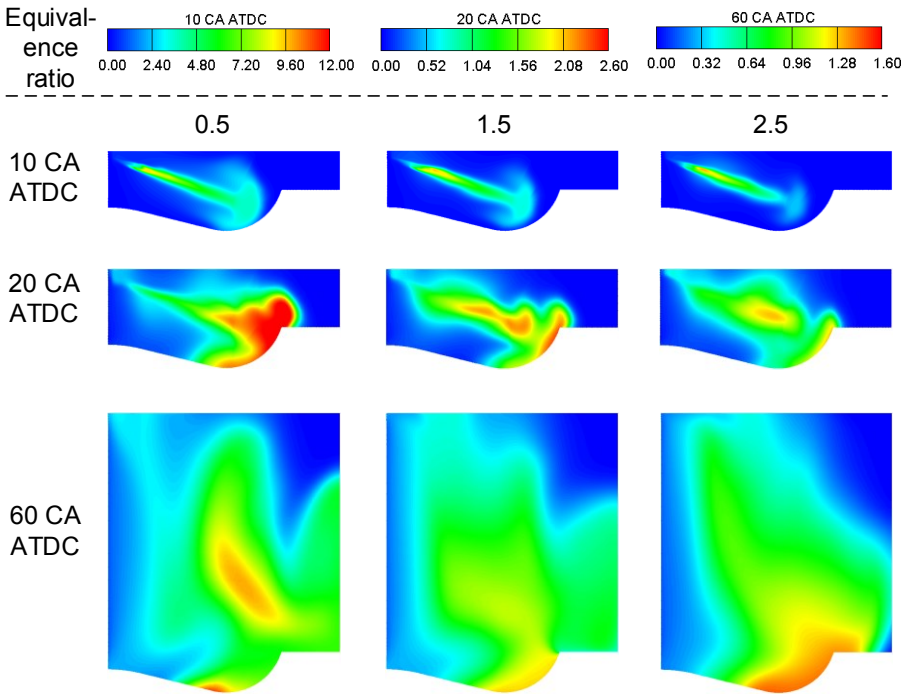

Figure 6-18 Influence of various swirl ratios on combustion

6.5. Bowl diameter

The variation of the bowl diameter is shown in Figure 6-19. The black line indicates the shape of the baseline combustion chamber, the blue line and the purple line represent the lower boundary and the higher boundary of the bowl diameter respectively.

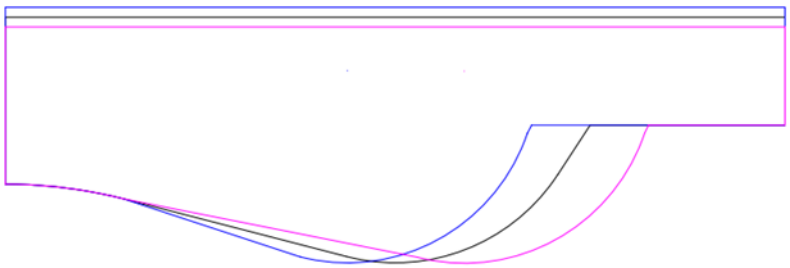

Figure 6-19 Demonstration of bowl diameter variation range

From Figure 6-20, it can be seen that the bowl diameter mainly affects the NO_x emissions, soot emissions and SFOC under L50 load, whereas the NO_x emissions increase in line with an increase in the bowl diameter and reach a peak when the bowl diameter is 120 mm, before they gradually decline. An opposite trend is witnessed for the SFOC. The soot emissions only slightly affected by the bowl diameter at the L100 load. The possible reasons that the bowl diameter has a greater influence on the emissions and SFOC at L50 is connected to the penetration length of the fuel oil injection. At L50 engine load, the injection penetration length is much lower than that at high engine loads. However, it is more suitable to be matched with the bowl diameter of 120 mm. In this circumstance, it makes the combustion more complete at L50 engine load, which explains the higher NO_x emissions and lower SFOC when the bowl diameter is 120 mm. The soot emissions decrease in line with

an increase in the bowl diameter and remain constant when the bowl diameter is 120 mm, then increase to nearly three times of their original value.

The emissions and SFOC change with the bowl diameter under each engine load can be explained through Figure 6-21, Figure 6-22 and Figure 6-23. As shown in Figure 6-23, a small bowl diameter means that more liquid fuel hits the surface of the piston and adheres thereto; thus, some amount of liquid fuel is not able to evaporate and atomise in time, which leads to an incomplete combustion. This explains why the soot emissions and SFOC were high when the bowl diameter was small. At the same time, the low maximum temperature of the incomplete combustion is unfavourable for the formation of NO_x. When the bowl diameter increases, the incomplete combustion phenomenon alleviates, the temperature rises, soot emissions and SFOC decrease and NO_x emissions increase at the same time. This trend reverses when the bowl diameter is larger than 120 mm. A large bowl diameter implies a longer distance between the fuel injector and the piston bowl surface. Most of the fuel is injected targeting solely the piston bowl surface in order to form a high-density mixture, which is not favourable for a complete combustion. Meanwhile, it encourages soot formation and leads to high levels of SFOC. At the same time, a slightly lower maximum temperature is achieved in order to generate a reduced number of NO_x emissions, by making a comparison with the moderate bowl diameter case.

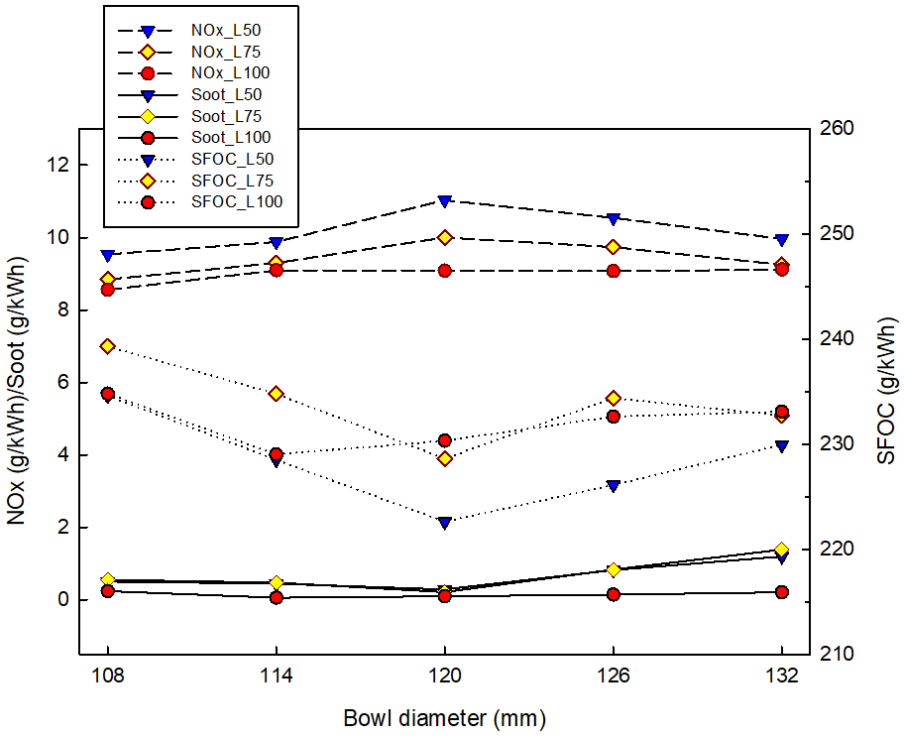

Figure 6-20 Influence of various bowl diameters on NO_x emissions, soot emissions and SFOC

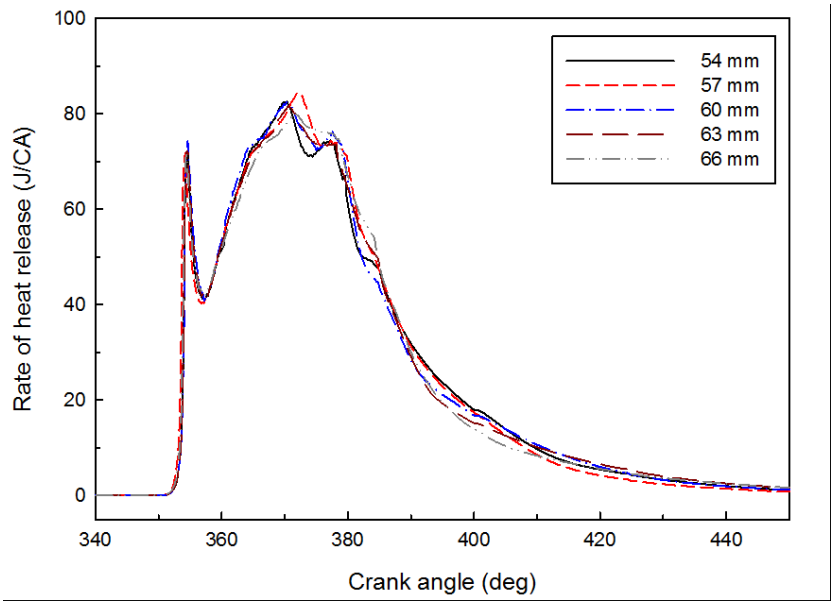

Figure 6-21 Influence of various bowl diameters on rate of heat release

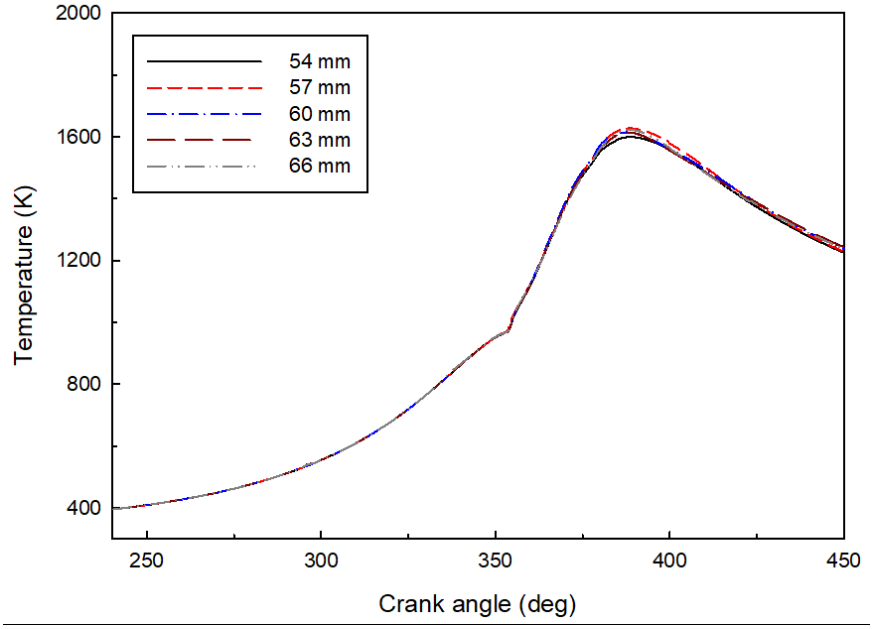

Figure 6-22 Influence of various bowl diameters on temperature

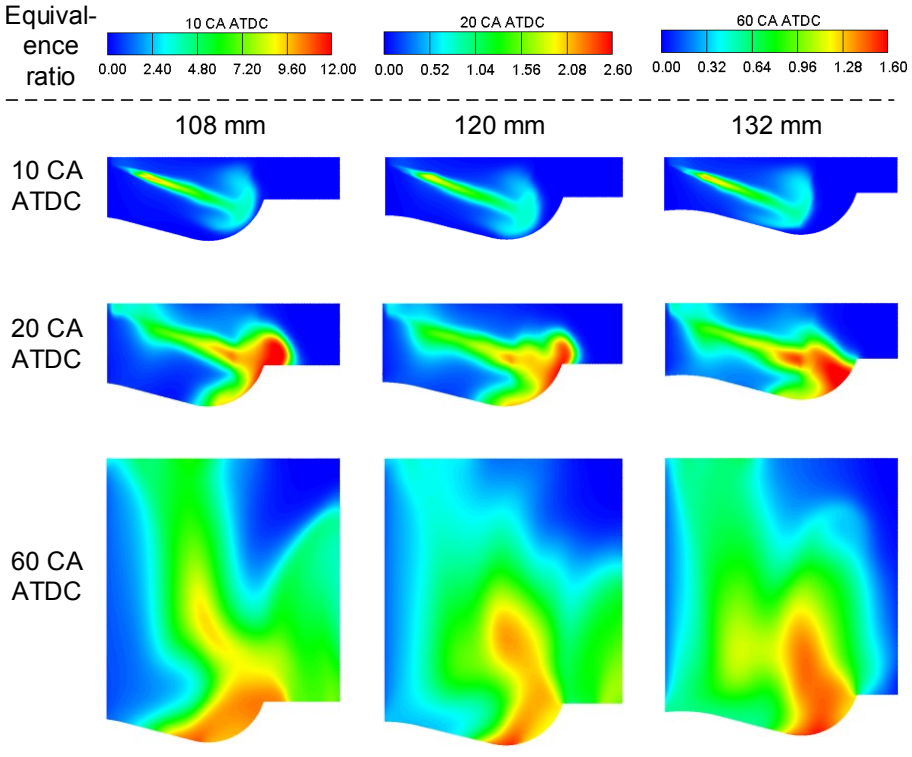

Figure 6-23 Influence of various bowl diameters on combustion

6.6. Centre crown height

The centre crown height variation range is shown in Figure 6-24. The black line is the baseline shape, the blue line and the purple line indicate the lower boundary and the higher boundary of the centre crown height.

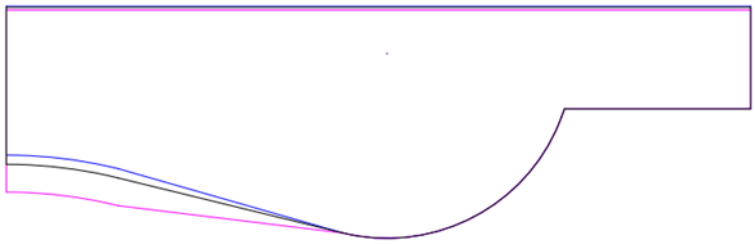

Figure 6-24 Demonstration of centre crown height variation range

From Figure 6-25, there are no obvious trends for the influences of the centre crown height on the NO_x emissions, soot emissions and SFOC at each engine load. It can be proved from Figure 6-26, Figure 6-27 and Figure 6-28 that there are small differences in the rate of heat release, temperature and combustion. This is because with an increase in the centre crown height, the volume around the centre crown is increased. However, it seems to have no effect on the fuel-air mixing.

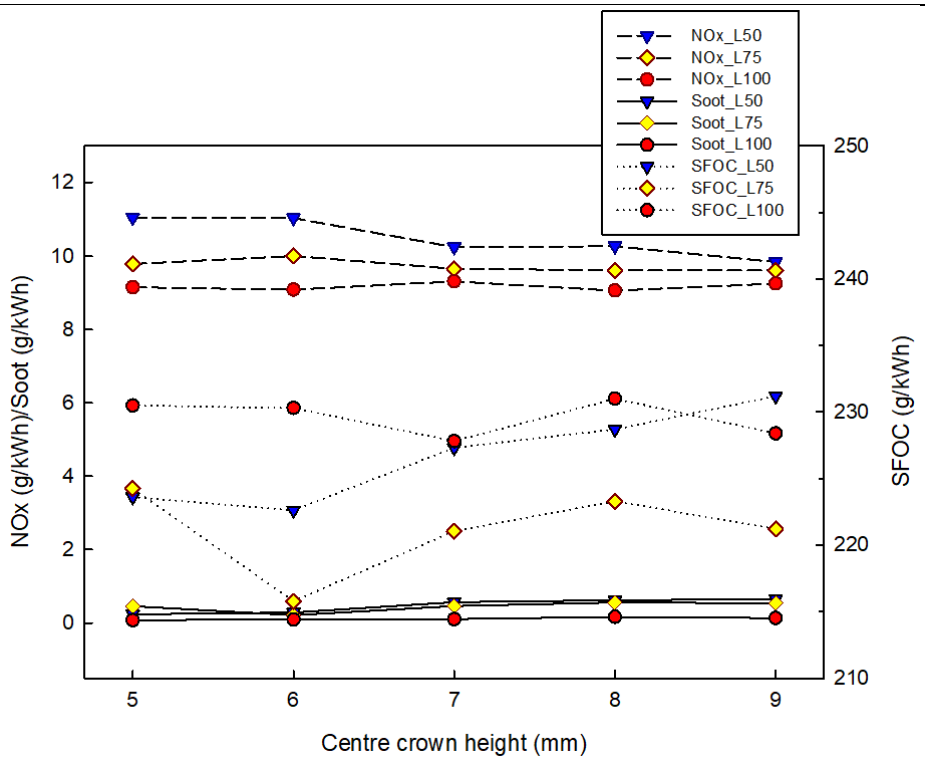

Figure 6-25 Influence of various centre crown heights on NO_x emissions, soot emissions and SFOC

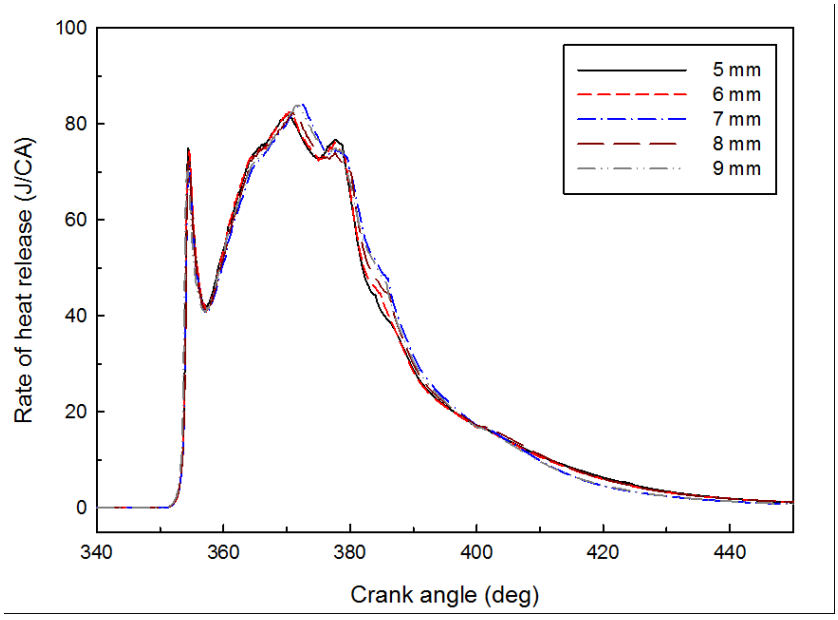

Figure 6-26 Influence of various centre crown heights on rate of heat release

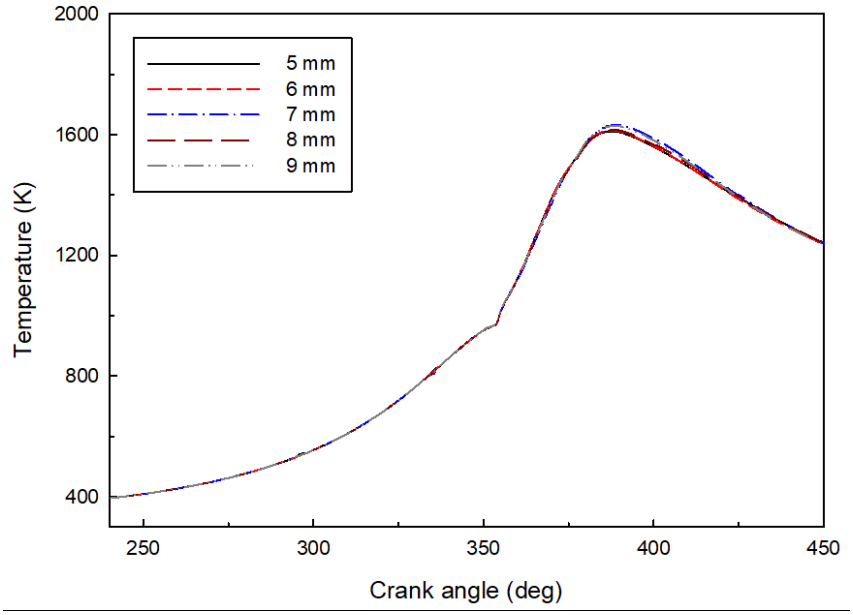

Figure 6-27 Influence of various centre crown heights on temperature

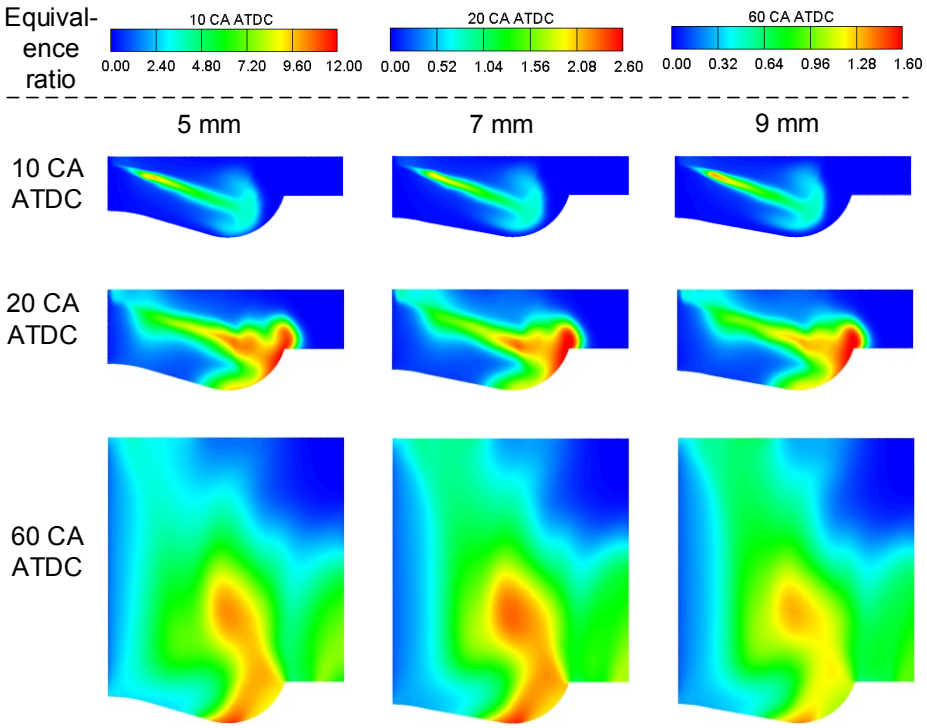

Figure 6-28 Influence of a various centre crown heights on the combustion

6.7. Toroidal radius

The variation range of the bowl diameter is shown in Figure 6-29. The black line indicates the shape of the baseline combustion chamber, the blue line and the purple line present the lower boundary and the higher boundary of the bowl diameter respectively.

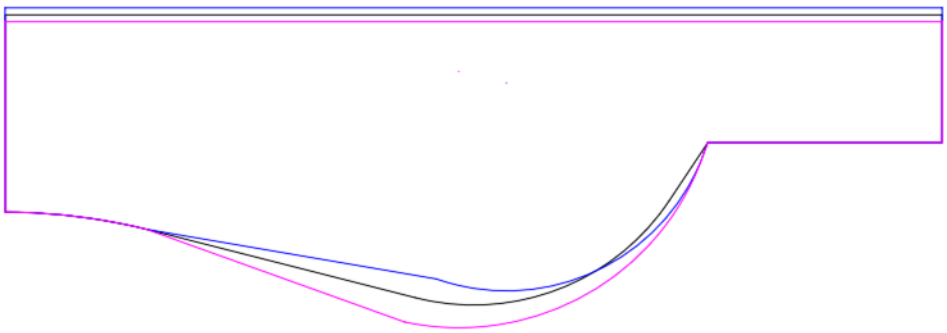

Figure 6-29 Demonstration of the toroidal radius variation range

From Figure 6-30, it can be seen that NO_x emissions slightly increased with an increase in the toroidal radius. Soot emissions drop slightly and SFOC declines as the toroidal radius increases on all loads. The above can be explained from Figure 6-33: it can be seen that the space at the piston bowl increases with an increase in the toroidal radius, which provides more room for the fuel-air mixing and avoids the fuel impingement with the bowl surface. Thus, a more homogenous mixing can be achieved, this can be proved in Figure 6-33 at 60 degree CA ATDC. A more homogenous mixing means that a more complete combustion was achieved, which lead to a high rate of heat release (as shown in Figure 6-31) and high temperature (as shown in Figure 6-32). The complete combustion helps reduce soot formation and improves fuel economy, but a high temperature encourages NO_x generation.

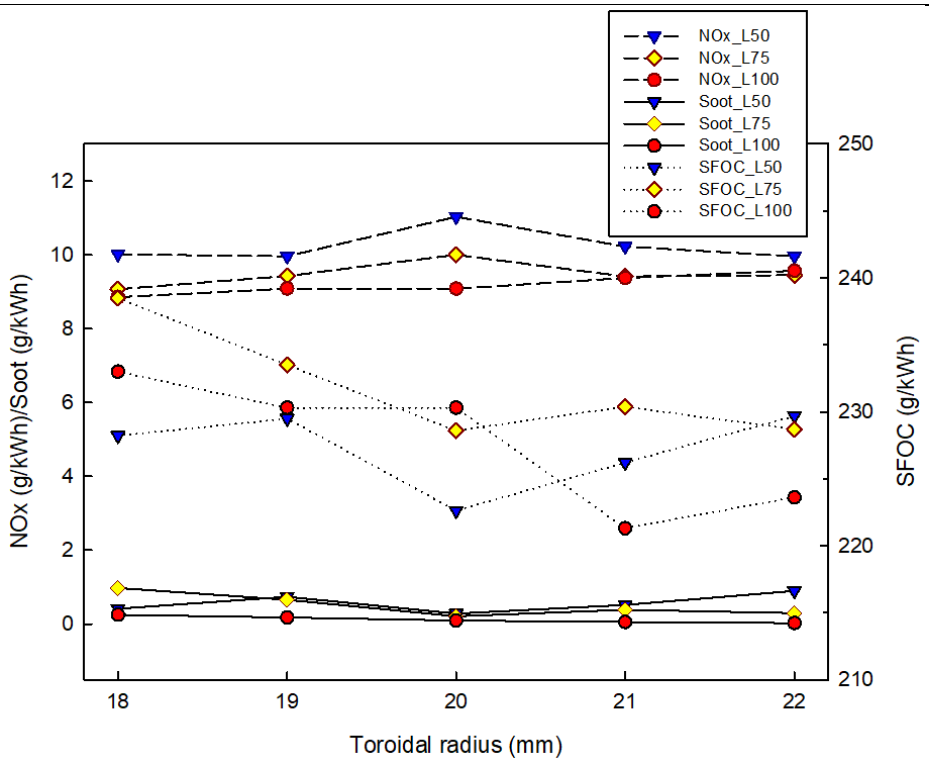

Figure 6-30 Influence of various toroidal radii on NO_x emissions, soot emissions and SFOC

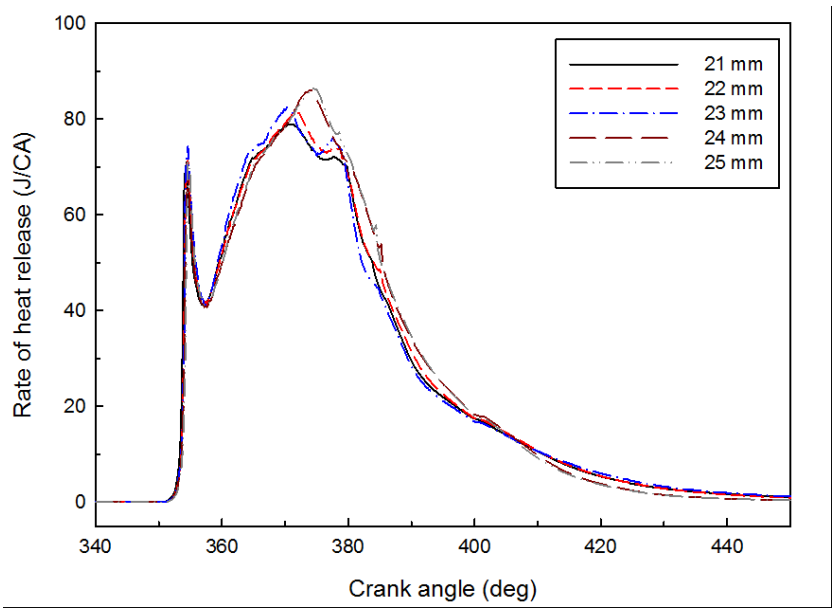

Figure 6-31 Influence of various toroidal radii on rate of heat release

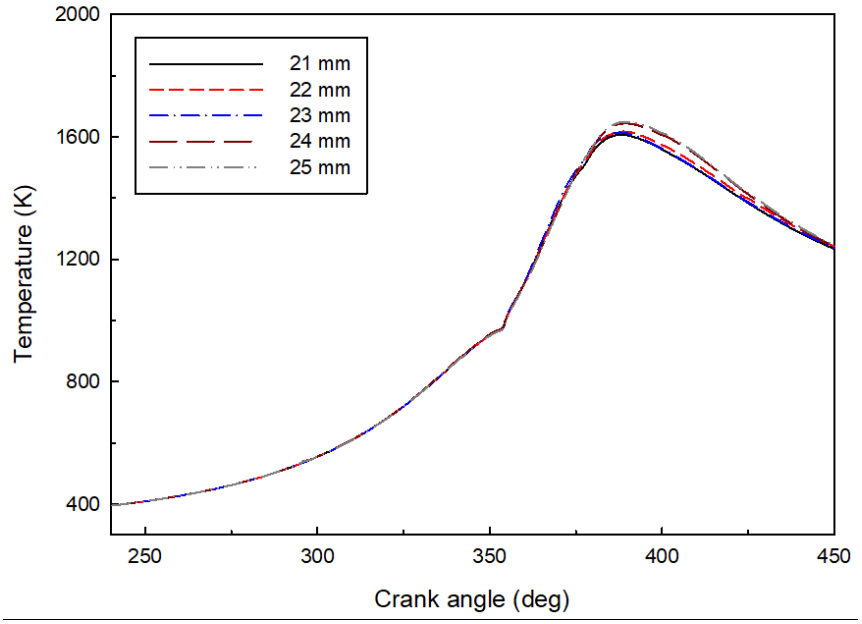

Figure 6-32 Influence of various toroidal radii on temperature

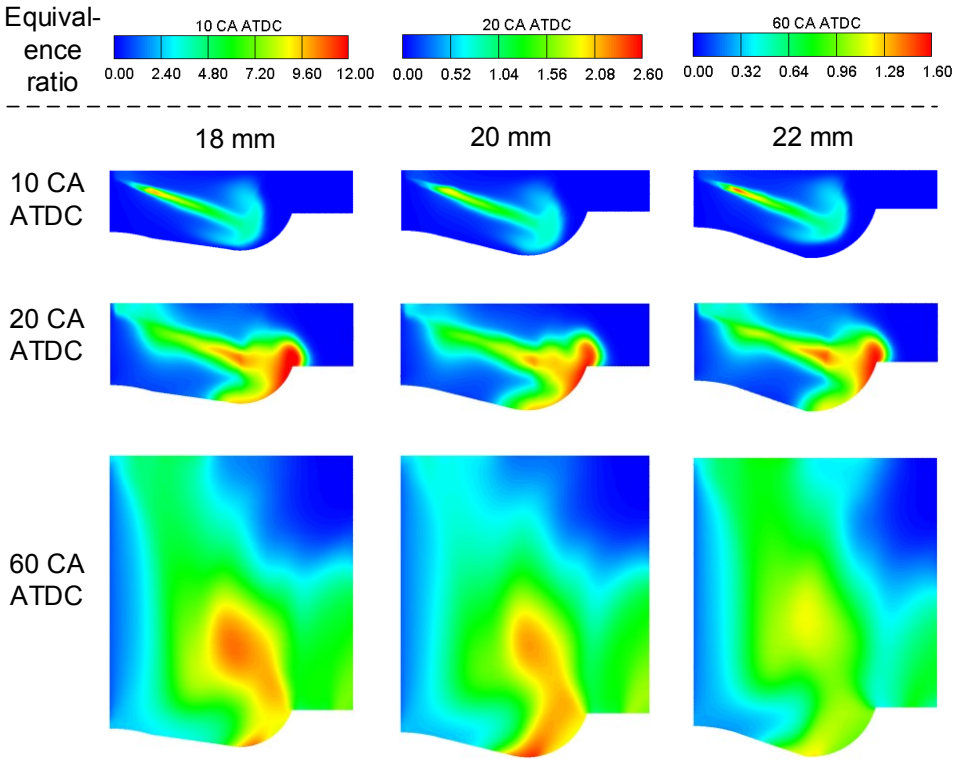

Figure 6-33 Influence of various toroidal radii on combustion

6.8. Summary

In this chapter, a parametric study was undertaken to understand how the parameters of the electronic fuel injector match with a combustion chamber affect emission and fuel economy. The study was conducted using three engine loads where only one parameter varied with each specified step each time. More details were also presented by the rate of heat release, temperature and combustion process. In general, injection-related parameters were more influential on emissions and SFOC than the combustion chamber geometries, and the injection timing seems to be the most influential one of all.

The main conclusions are below:

(1) NO_x increases with an increase in the spray angle, while both the soot emissions and SFOC decrease.

(2) NO_x emissions decrease with an increase in the nozzle protrusion length. In contrast, soot emissions and SFOC increase with an increase in the nozzle protrusion length.

(3) With the increase in injection timing BTDC, a consistent increasing trend of the NO_x emissions is observed. In contrast, an opposite decreasing trend is observed in the case of the SFOC. The NO_x emissions at 20 degrees BTDC are approximately three times higher than at the TDC. The SFOC decreased by nearly 20% from the TDC to 20 degrees BTDC. Soot emissions decrease slightly with an increase in the injection timing.

(4) The NO_x emissions increase with an increase in the swirl ratio at high loads. However, the NO_x emissions remain nearly the same at low loads. For soot emissions, an increasing trend is observed as the swirl ratio increases. The SFOC reports an increasing trend at low loads. However, the SFOC is not affected much by the swirl ratio at high loads.

(5) The NO_x emissions increase with an increase in the bowl diameter and reach a peak when the bowl diameter is about 120 mm before they gradually decline. An opposite trend is witnessed for the SFOC. Soot emissions decrease in line with an increase in the bowl diameter and reach lowest value when the bowl diameter is 120 mm, then increase to nearly three times of their original value.

(6) The centre crown height has little effect on emissions and fuel consumption.

(7) NO_x emissions slightly increase with an increase in the toroidal radius. Soot emissions and SFOC decrease with an increase in the toroidal radius.

Chapter 7. Multi-objective study of injection-related parameters and combustion chamber geometries

7.1. Introduction

The literature has shown an increase in the use of advanced algorithms for the optimisation of diesel engines. Some meaningful work on the comparisons of these algorithms used for engine optimisation were also investigated. Shi et al. [81] assessed μGA, NSGA II and ARMOGA incorporating with a KIVA code for the optimisation of a combustion chamber under certain conditions. The derived results indicated that the NSGA II algorithm with a large population of 32 performed the best by considering the optimal solutions' optimality and diversity. Navid et al. [101] compared the GA and the NLPQL algorithms used for the optimisation of a Ford 1.8 L DI engine. Four factors, including injection angle, half spray cone angle, inner distance of bowl wall and bowl radius were selected to be optimised. Results showed that NLPQL approaches an optimal design faster than GA. It would be interesting to know whether NLPQL algorithm would still be efficient when used for the optimisation of seven engine design parameters of a medium-speed marine diesel engine.

In principle, the NLPQL algorithm is a local optimisation algorithm. Whether an optimal design can be reached or not relies heavily on the starting point, because once the NLPQL algorithm reaches a local optimum, there is no mechanism to get away from it [102]. So, a good starting point is crucial for the NLPQL algorithm. However, MOGA is a global algorithm that is not affected by a starting point. A better method is that the optimal design achieved by MOGA is set as the starting point of the NLPQL algorithm. To the best knowledge of the author, this kind of study has never been conducted in the optimisation of a medium-speed marine diesel engine with seven design parameters.

In this chapter, the NO_x emissions, soot emissions and SFOC are the three

sub-objectives to be optimised. The NLPQL algorithm and MOGA were compared for the optimisation of seven match parameters of the injector and combustion chamber for a medium-speed marine diesel engine. The seven parameters were: injection timing, spray angle, nozzle protrusion length, swirl ratio, bowl diameter, centre crown height and toroid radius. Then, the optimal design of MOGA was set as the starting point of the NLPQL algorithm for seeking a possible improved optimum. Finally, the influences of design parameters on objectives were discussed by RSM.

7.2. Optimisation settings

7.2.1. Optimisation settings of the NLPQL algorithm

The optimisation settings of the NLPQL algorithm are listed in Table 7-1. The Latin hypercube method was used before the NLPQL algorithm to generate start designs during the optimisation process.

Table 7-1 Optimisation setting of the NLQPL algorithm

Property	Value
Max. Number of Function Evaluations	5
Max. Number of Iterations	20
Step Size for Finite Difference Step	0.001
Accuracy	1e-05

If the NLPQL algorithm is used to solve a multi-objective problem, a merit function with a weighted sum method must be adopted to transfer it to a single objective optimisation problem. The formula of the weight sum method is

$$Objective = \sum_{i=1}^{k} \mu_i O_i(x) \tag{7.1}$$

In(7.1), μ_i is the weight of each objective, which is decided by researchers

according to their experiences and O_i are the objectives.

The general rule for selecting the weights is to make sure the sub-objectives are in the same magnitude, however, in this paper, the NO_x emissions are emphasised. The merit function is built into (7.2) to reduce the NO_x and soot emissions, and to also minimise the fuel consumption rate. The weights are given according to experience and the literature [55].

$$\text{Objective} = \left(\frac{NOx}{NOx\_b}\right)\times 5 + \left(\frac{Soot}{Soot\_b}\right)\times 1 + \left(\frac{SFOC}{SFOC\_b}\right)\times 3 \qquad (7.2)$$

Where: NOx_b, $Soot\_b$ and $SFOC\_b$ are the values of the baseline design.

7.2.2. Optimisation settings of the MOGA

The optimisation settings of the MOGA are listed in Table 7-2. Distribution for crossover probability and for mutation probability are both set to the default value of 10. A generation number of 10 and population size of 20 are adopted here. Usually, crossover probability and mutation probability are set to 0.7 and 0.1 respectively.

Table 7-2 Optimisation setting of MOGA

Property	Value
Distribution for crossover probability	10.0
Distribution for Mutation Probability	10.0
Number of Generations	10
Population size	20
Crossover Probability	0.7
Mutation Probability	0.1

All of the simulations in this chapter were carried out at L100 engine load.

7.3. Comparison of NLPQL and MOGA

7.3.1. Optimisation history comparison

Figure 7-1and Figure 7-2 report the optimisation history with the NLPQL algorithm and MOGA respectively. The red vertical dash line indicates the Run ID 17 has the minimum objective. The red circles identify the history of objectives. The ratios of NO_x, soot and SFOC to the baseline design are represented by black diamond, blue triangle and reversed yellow triangle, respectively.

In Figure 7-1, the first 30 results were the Latin hypercube designs. The rest of the runs were the searching history of the NLPQL algorithm. The best objective is located at Run 17. The total runs of the NLPQL algorithm end at 90, the complete calculation takes nearly five days on a computer with four-core Intel i7-4790 CPU@ 3.6 GHz. In Figure 7-2, the total runs ends at 240, the simulation lasted eleven days and on the same computer. Usually, MOGA optimisation is much more time consuming than NLPQL optimisation.

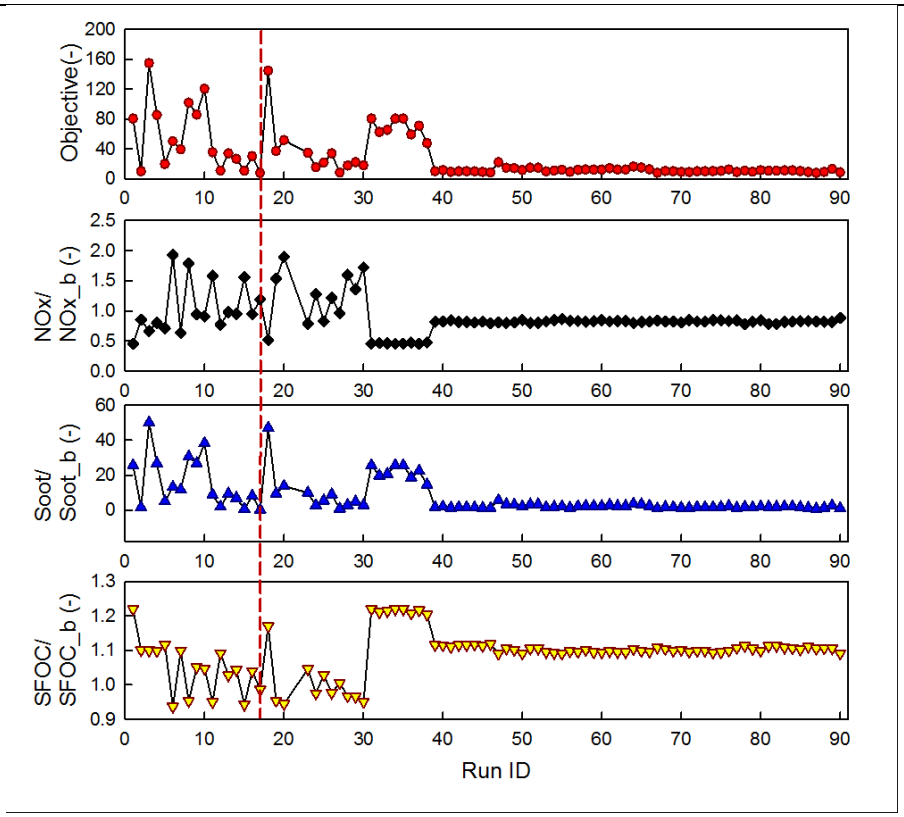

Figure 7-1 Optimisation history with the NLPQL algorithm

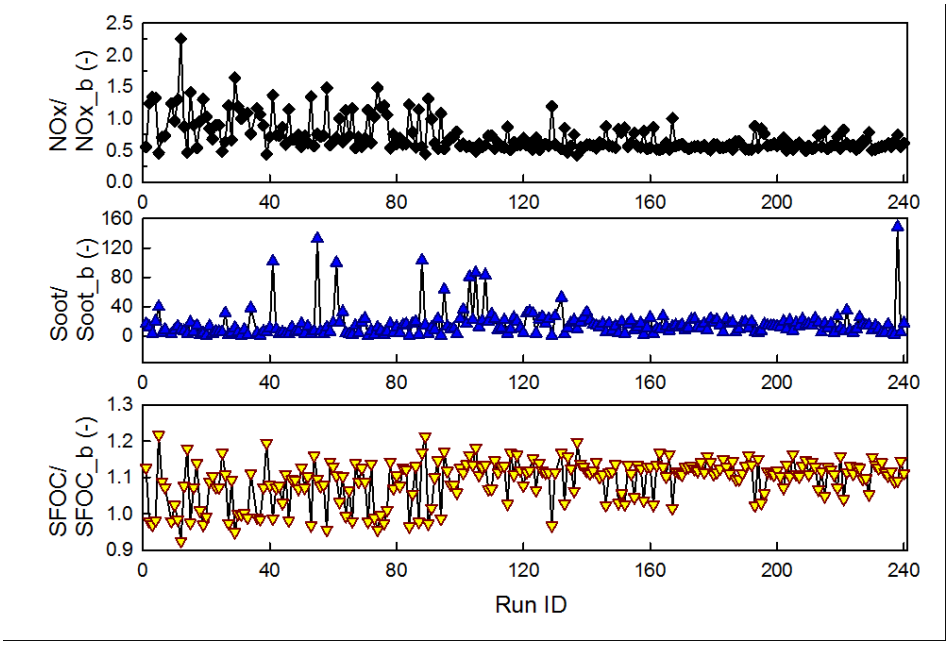

Figure 7-2 Optimisation history with the MOGA

7.3.2. Objective comparison

Figure 7-3 and Figure 7-4 show the scattering maps of NO_x versus soot and NO_x versus SFOC for the NLPQL algorithm and MOGA, respectively. The optimal Run ID 17 yielded by the NLPQL algorithm is defined to OPT_N, and is also represented by the blue triangle. The black rectangular points stand for the baseline design and the black hollow triangle points represent Pareto solutions. The OPT_N achieved a huge reduction of soot emissions by 94.8% and a slight drop of SFOC by 3.9%. Details are shown in

Table 7-3. The soot emissions for the baseline engine are already ultra-low, thus, a further reduction of soot seems not worth pursuing. A more prominent issue is to cut down NO_x emissions. However, the OPT_N failed to reduce NO_x emissions but increased them by 18.7% instead. From the scattering maps, there surely exists a better trade-off point between NO_x emissions and soot emissions, but the objective function failed to spot it. This kind of failure may be linked to non-appropriate selection of weights in the merit function of the NLPQL algorithm.

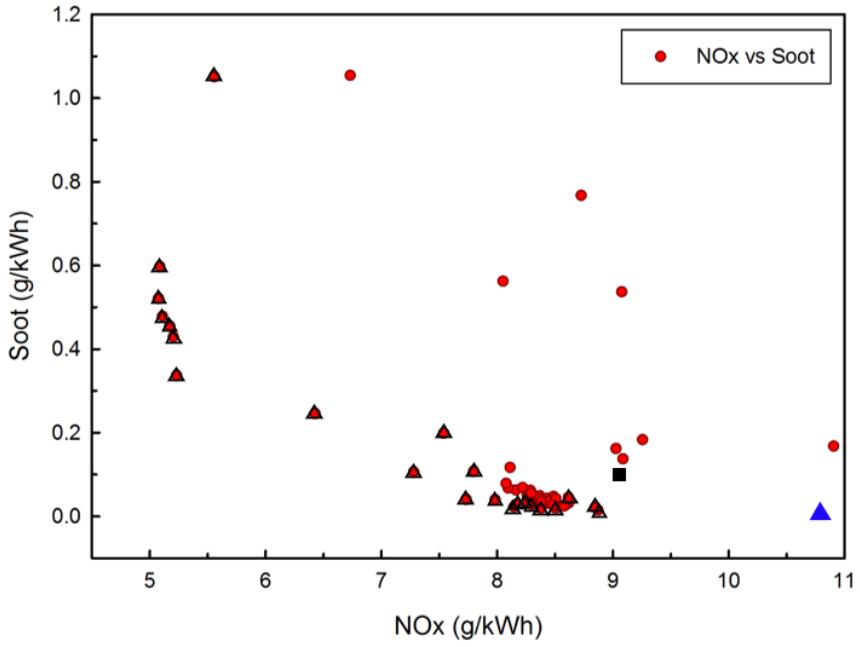

Figure 7-3 NO_x vs soot of the NLPQL algorithm

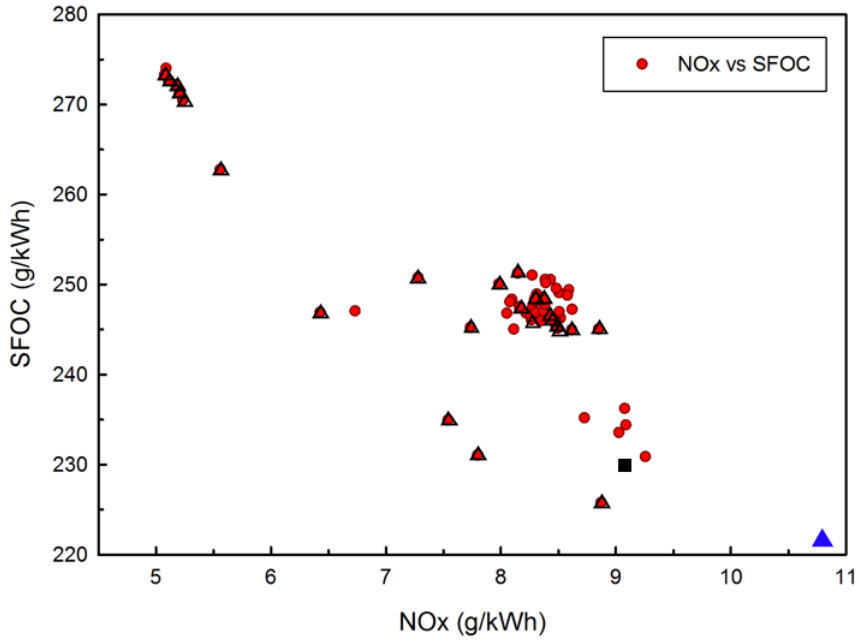

Figure 7-4 NO_x vs SFOC of the NLPQL algorithm

Figure 7-5 and Figure 7-6 show the optimisation results obtained with MOGA. In the scattering charts, all the Pareto designs are feasible solutions for the multi-objective design. The Pareto design with the best trade-off between NO_x and soot was selected as the optimal design. Here the optimal design is Run ID 14, which was also represented by OPT_M and marked with a blue diamond point. Compared to the baseline design, the optimal design achieves a reduction of NO_x emissions by approximately 44% and soot emissions by 33%, whereas it gets a penalty of an SFOC increase of nearly 15% (see

Table 7-3).

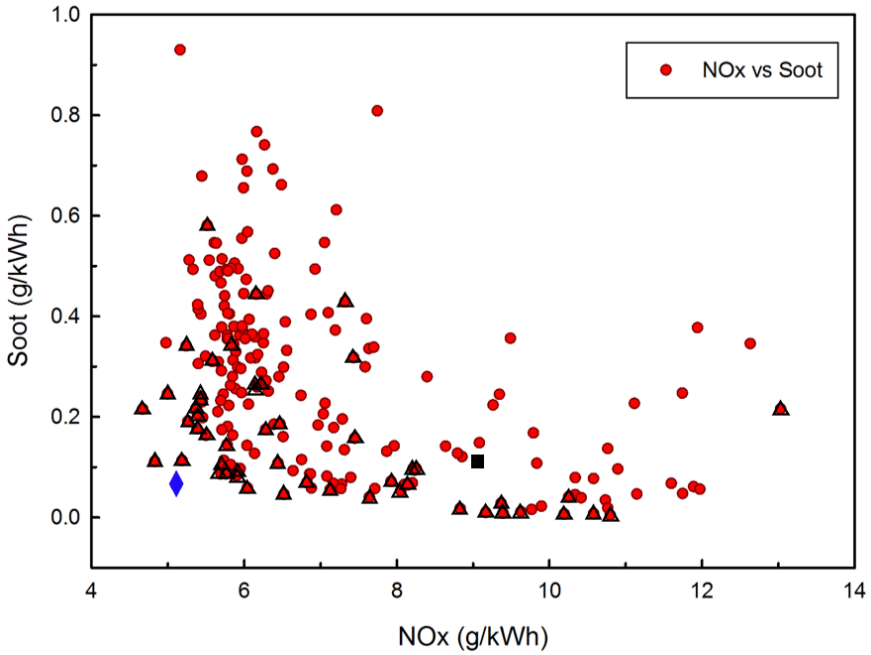

Figure 7-5 NO_x vs soot of MOGA

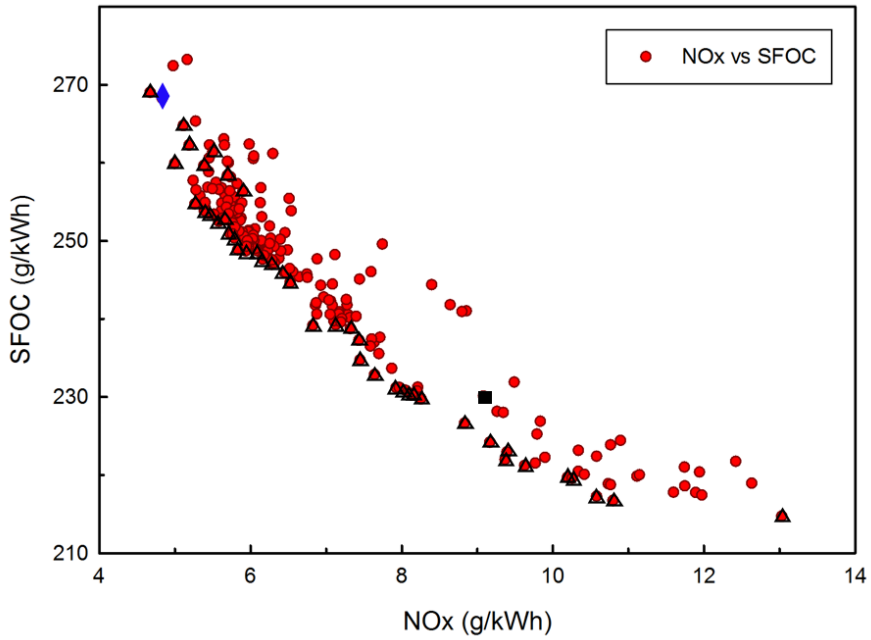

Figure 7-6 NO_x vs SFOC of MOGA

Table 7-3 Details of the objectives

Designs	NO_x (g/kWh)	Soot (g/kWh)	SFOC (g/kWh)
Baseline	9.09	0.096	230
OPT_N	10.79	0.005	221
OPT_M	5.11	0.064	264

Table 7-3 also indicates that both the baseline and OPT_N fail to meet the IMO Tier II regulations, which require NO_x emissions to be lower than 8.98 g/kWh for the specific MAN 16/24 diesel engine. However, OPT_M meets the IMO Tier II regulations.

7.3.3. Sub-objective comparison

Table 7-4 gives the details of the best sub-objectives of the NLPQL algorithm and MOGA. The light blue background in Table 7-4 highlights the minimum values that each best sub-objective case can achieve. Compared to the baseline design, regardless of the huge reduction achieved by both algorithms, more attention is paid to the differences between these best sub-objectives obtained by the NLPQL algorithm and MOGA. It can be seen that NO_x_M shows a superb lower sub-objective than that of the NLPQL algorithm. The sub-objectives of the lowest soot designs were approximately the same. The best SFOC cases of both algorithms were reported to have approximate the same SFOC and extremely heavy NO_x emissions. However, slightly lower soot emissions were obtained by SFOC_M.

Table 7-4 Best sub-objective comparisons of the NLPQL algorithm and MOGA

Designs	NO_x (g/kWh)	Soot (g/kWh)	SFOC (g/kWh)
Baseline	9.09	0.096	230
NO_x_N	5.08	0.5213	273
NO_x_M	4.67	0.2153	269
Soot_N	10.79	0.0050	221
Soot_M	10.78	0.0044	217
SFOC_N	16.59	0.2372	210
SFOC_M	19.17	0.1416	208

7.3.4. Design parameter comparison

Table 7-5 shows the design parameters of the best sub-objective designs. Some commonalities were apparent in that low NO_x designs prefer late injection and low swirl, while low SFOC designs relate to early injection, high swirl and large nozzle protrusion length. Detailed explanations will be given later.

Generally, MOGA is more time consuming, but achieves a better design in each sub-objective and offers more feasible Pareto designs. A design with the best balance between sub-objectives can be achieved effectively by MOGA. From the mechanism of the NLPQL algorithm, a better starting point is crucial to the results. If the optimal design provided by MOGA was set to the starting point of the NLPQL algorithm, a design with lower NO_x emission may turn up.

Table 7-5 Design parameters comparisons of designs with best sub-objectives

Designs	SOI (CA)	Swirl ratio	Spray angle (deg)	Nozzle protrusion length (mm)	Bowl diameter (mm)	Centre crown height (mm)	Toroidal radius (mm)
Baseline	710.0	1.0	143.0	2.5	120	6.0	20.0
NO_x_N	717.9	0.5	154.2	1.1	132	8.9	18.4
NO_x_M	719.0	0.6	143.8	3.2	109	6.5	20.3
Soot_N	713.1	1.7	145.9	2.5	120	5.7	20.1
Soot_M	704.3	1.0	145.8	2.2	123	5.5	20.3
SFOC_N	702.1	1.7	152.5	4.0	129	7.1	19.4
SFOC_M	719.3	1.9	131.7	4.0	121	7.5	20.0

7.4. Sequential use of NLPQL and MOGA

Since the starting point provided by MOGA is supposed to be a good starting point, a smaller scope for each design parameter was defined, as shown in Table 7-6.

Table 7-6 Variation ranges of parameters used for optimisation

Parameters	Code	OPT_M	Lower boundary	Upper boundary
Injection timing, deg	SOI	719	716	720
Swirl ratio	SR	0.6	0.3	0.9
Spray angle, deg	SA	148	141	155
Nozzle protrusion length, mm	NPL	1.4	1.0	1.8
Toroidal radius, mm	r002	21.3	20	22
Centre crown height, mm	v003	8.2	7	9
Bowl diameter, mm	2*h001	120.9	114	126

Figure 7-7 reported the optimisation history of the sequential optimisation process

has a maximum of 52 runs. The best objective was located at run 36 (OPT_M&N), which is indicated by the red dashed line. The total runs are far less than that of MOGA. Figure 7-8 and Figure 7-9 show the NO_x versus soot and NO_x versus SFOC respectively. The blue diamond represents the optimal design obtained by MOGA, the black circles highlight the OPT_M&N. Obviously, the OPT_M&N, obtained by sequential methods, achieved a noticeable reduction of both NOx and soot emissions. However, it paid the price of a rise in SFOC. Specifically, the NO_x emissions, soot emissions and SFOC of OPT_M&N are 4.53 g/kWh, 0.041 g/kWh and 274 g/kWh respectively. By comparing to the OPT_M, the OPT_M&N design achieved a reduction of NO_x emissions and soot emissions of 11.4% and 35.9% respectively, with a penalty of SFOC rising by 3.6%. There is no doubt for OPT_M&N to achieve IMO Tier II regulations.

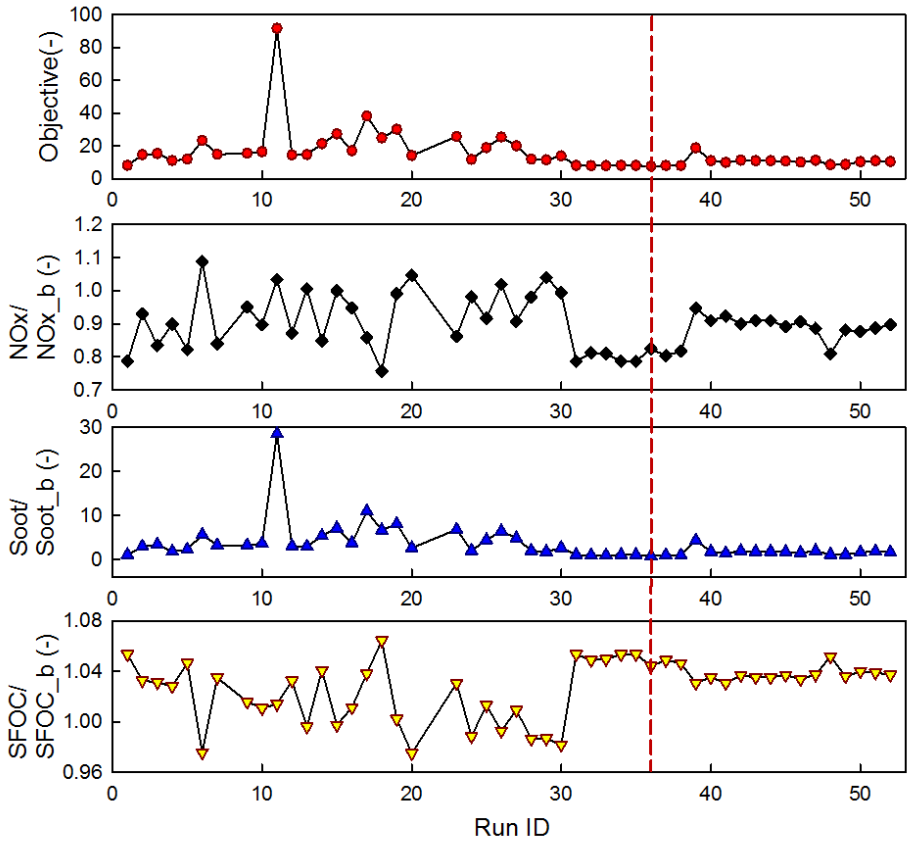

Figure 7-7 Optimisation history with sequential methods

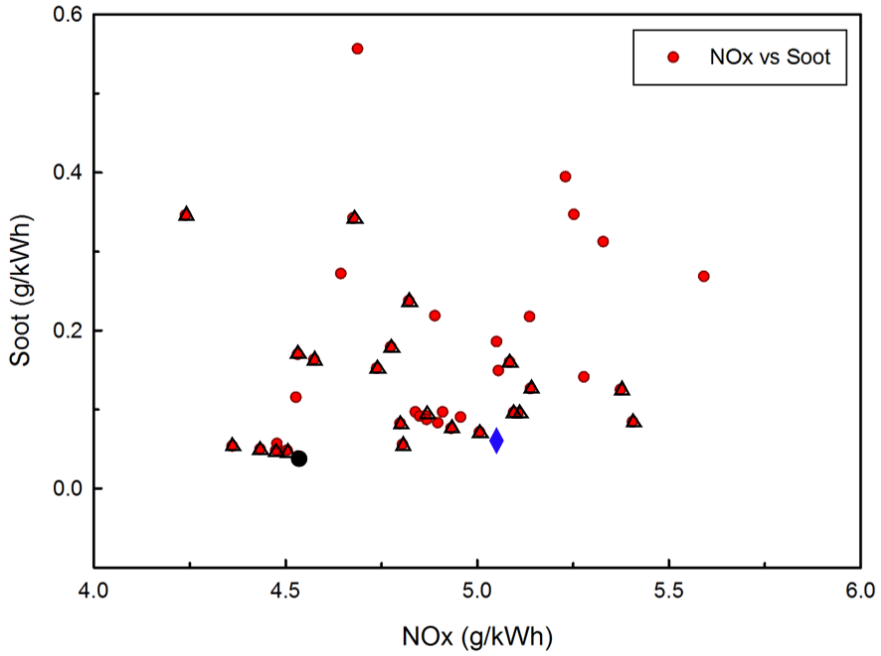

Figure 7-8 NO_x vs soot by sequential method

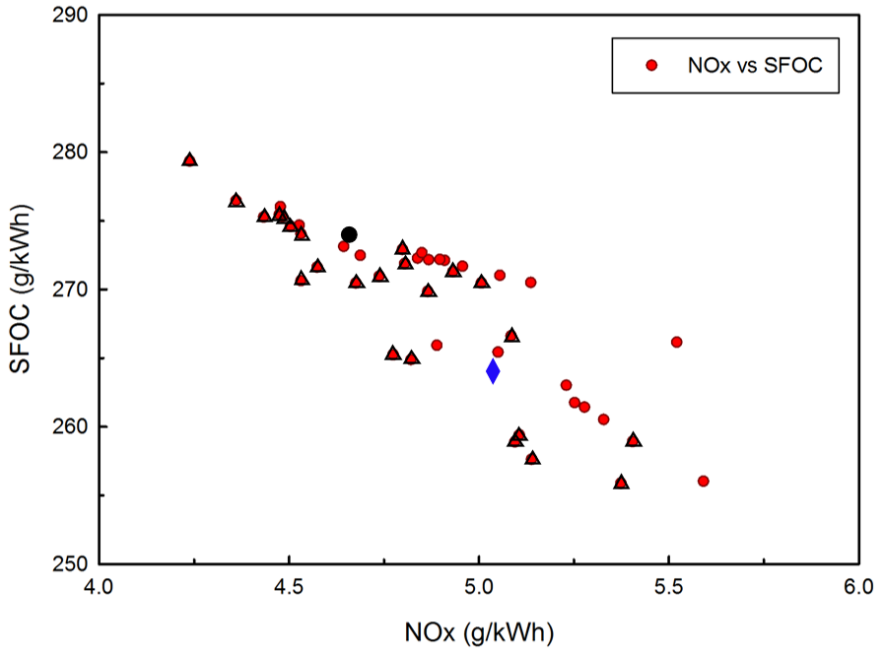

Figure 7-9 NO_x vs SFOC by sequential method

7.5. Detailed information about the combustion process

Table 7-7 reports detailed information about the values of the design parameters of the baseline and optimal designs. Comparisons of the combustion chamber shapes are shown in Figure 7-10, and the combustion details are given in depth in Figure 7-11 and Figure 7-12.

In Figure 7-10, the baseline shape is shown as grey background, while the shapes of OPT_N, OPT_M and OPT_M&N are indicated by blue, black and red lines respectively. It can be seen that optimum designs of OPT_M and OPT_M&N have a larger centre crown height, larger bowl diameter or larger toroidal radius in comparison to the baseline design. In general, the increase of the toroidal radius increases the volume of the piston bowl area, which leads to more room for fuel-air mixing and less wall impingement of the liquid fuel with the piston bowl surface. More homogenous mixing means that a better combustion can be achieved; this leads to a higher rate of heat release and a higher temperature. Better combustion also helps reduce soot emissions and improves fuel economy, but a high temperature encourages NO_x generation. The effects of the increase in bowl diameter on the sub-objectives similar to those with the increase in the toroidal radius. However, a too large bowl diameter results in the fuel oil injected solely targeting the bowl area of the piston to form high-density mixtures. It is not favourable for complete combustion, and so promotes soot formation and leads to a high SFOC. At the same time, a slightly lower temperature is achieved in comparison to that of a moderate bowl diameter situation to generate less NO_x emissions. Although optimal designs OPT_M and OPT_M&N both have large centre crown height, the effects of this may be unnoticeable, due to volume increment happens in the centre of the piston and low swirl is applied.

The optimal designs OPT_M and OPT_M&N also prefer late injection, low swirl and a large spray angle, as can be seen in Table 7-7. Late injection offers less time for fuel-air mixing, a large spray angle results in some liquid fuel adhering to the bottom

of the piston head and on the surface of the bowl area. Because of the low swirl in the combustion chamber, two separate high fuel density areas were spotted in Figure 7-12. These results lead to inadequate mixing. The low heat release and incomplete combustion suppress the maximum temperature, which is unfavourable for NO_x generation. That is one of the main reasons for the low NO_x emissions achieved in both the MOGA and sequential method. The detailed evidence is provided in Figure 7-11 (a), (b) and (c). Significantly high soot formation resulting from inadequate mixing were seen during the combustion progress in both optimal designs of MOGA and sequential method (see Figure 7-11 (d)). However, high soot formation rates do not necessarily mean high soot emissions thanks to the high rate of soot oxidation offered by the high temperature in the afterburning process. The high temperature in the afterburning process is the side benefit of late injection because more fuel is burned in the post combustion stage than in the baseline and OPT_N designs. Incomplete combustion in these optimal designs increased the high fuel consumption rate as well. A high swirl ratio is beneficial for fuel-air mixing, this can be proved by Figure 7-12, where the injection jets were distorted to be asymmetric. In 60 degree CA ATDC, a more homogeneous fuel distribution was seen the baseline and OPT_N designs, followed by a higher rate of heat release and maximum temperature, which encouraged NO_x formation and suppressed soot generation, as shown in Figure 7-11.

Table 7-7 Detailed design parameters of the baseline design and optimal designs

Designs	SOI (CA)	Swirl ratio	Spray angle (deg)	Nozzle protrusion length (mm)	Bowl diameter (mm)	Centre crown height (mm)	Toroidal radius (mm)
Baseline	710.0	1.0	143.0	2.5	120.0	6.0	20.0
OPT_N	713.1	1.7	145.9	2.5	119.6	5.7	20.1
OPT_M	719.0	0.6	147.9	1.7	120.9	8.2	21.3
OPT_M&N	719.6	0.3	154.5	1.0	126.0	8.9	20.2

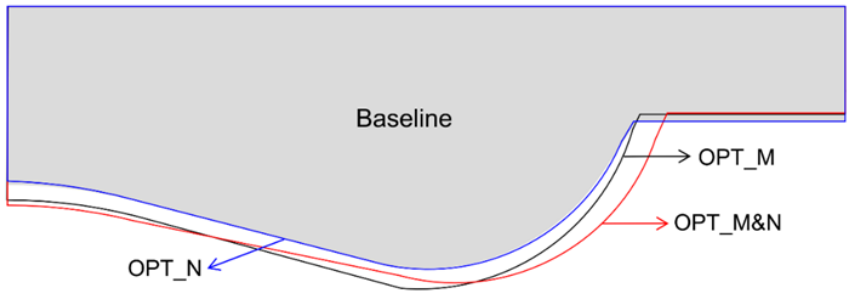

Figure 7-10 Comparison of combustion chamber shapes of the baseline design and optimal designs

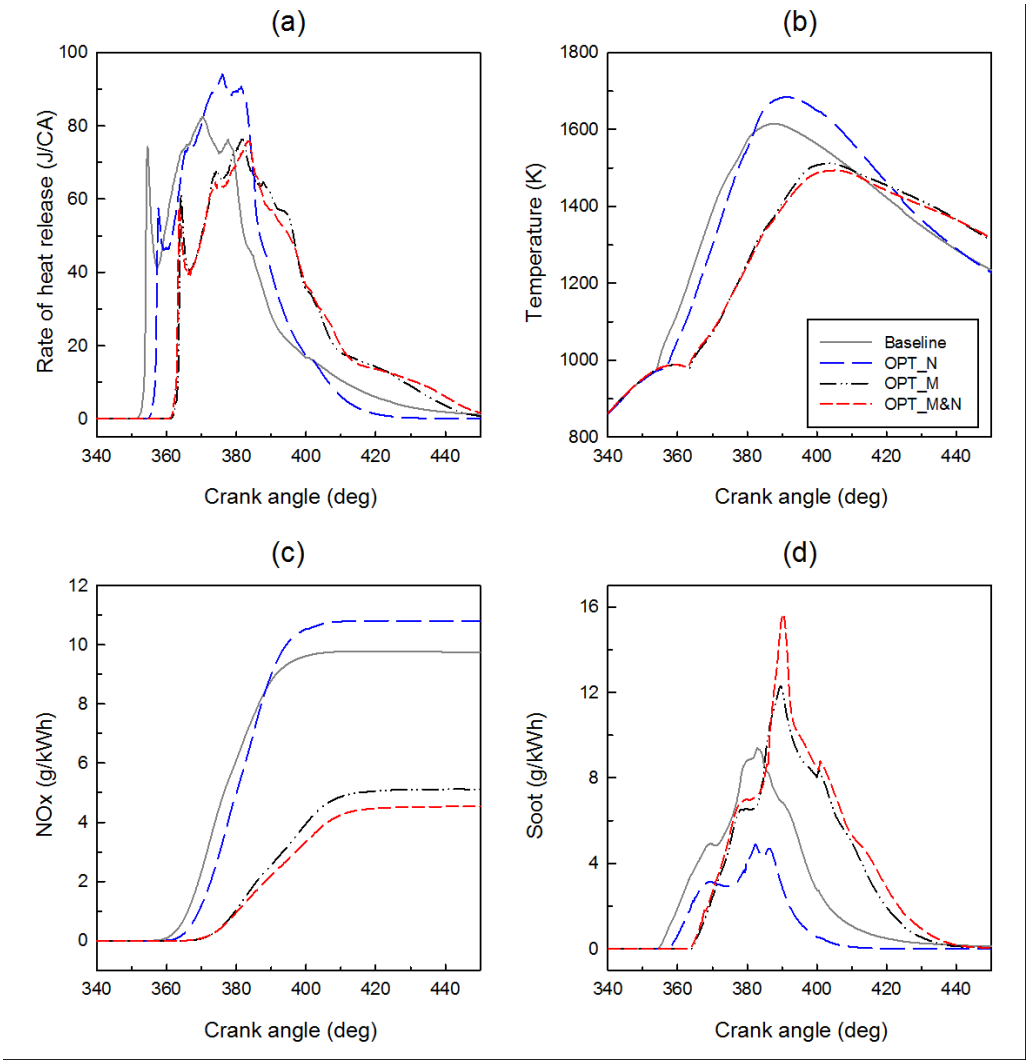

Figure 7-11 Detailed comparison of the baseline design and optimal designs

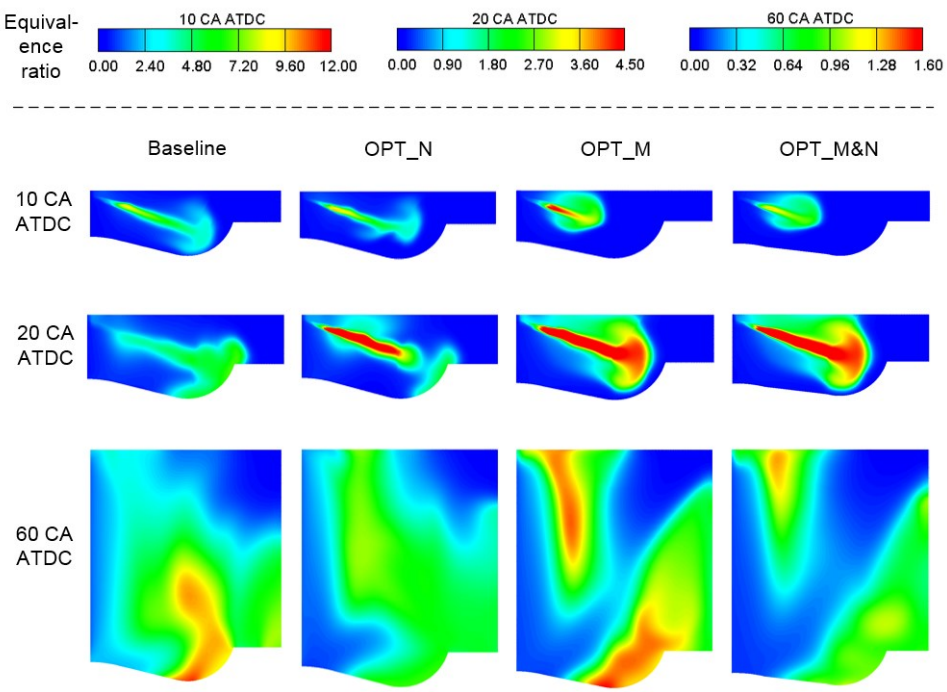

Figure 7-12 CFD comparison of fuel-air equivalence ratio of the baseline and optimal designs

7.6. RSM analysis

RSM was used to gain a better understanding of the influence of the important design parameters on the sub-objectives. Since a larger data set was obtained from MOGA, it is more suitable for RSM analysis. An SS-ANOVA algorithm was used to detect the most important design parameters prior to building RSM functions. Results are shown in Figure 7-13, Figure 7-14 and Figure 7-15. SOI has the largest effect on NO_x and SFOC, followed by SR and h001. Combustion chamber parameters have a larger impact on soot than other parameters, and the bowl diameter is the most influential one of all. Only the parameters ranked in the top three were selected for generating RSM functions.

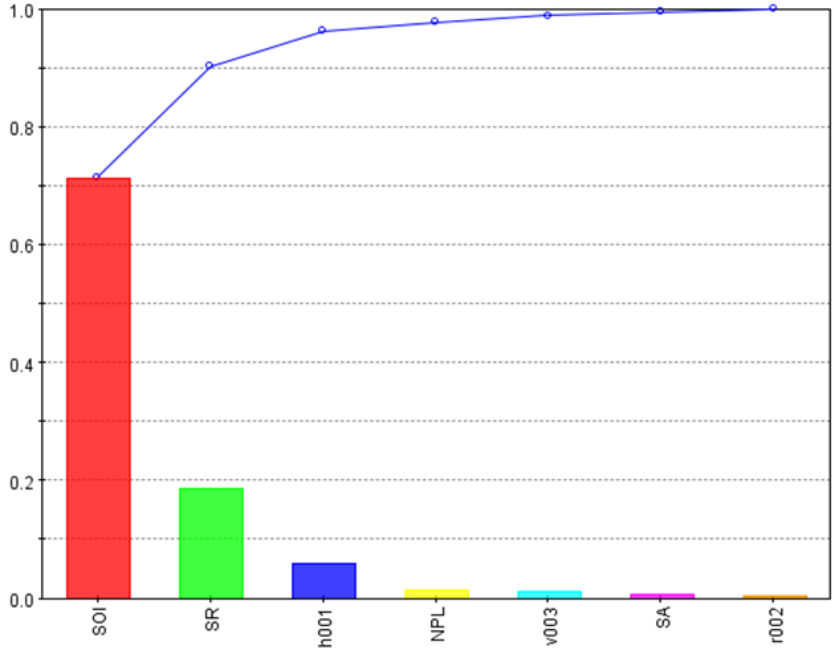

Figure 7-13 Sensitivity of design parameters on NO_x emissions

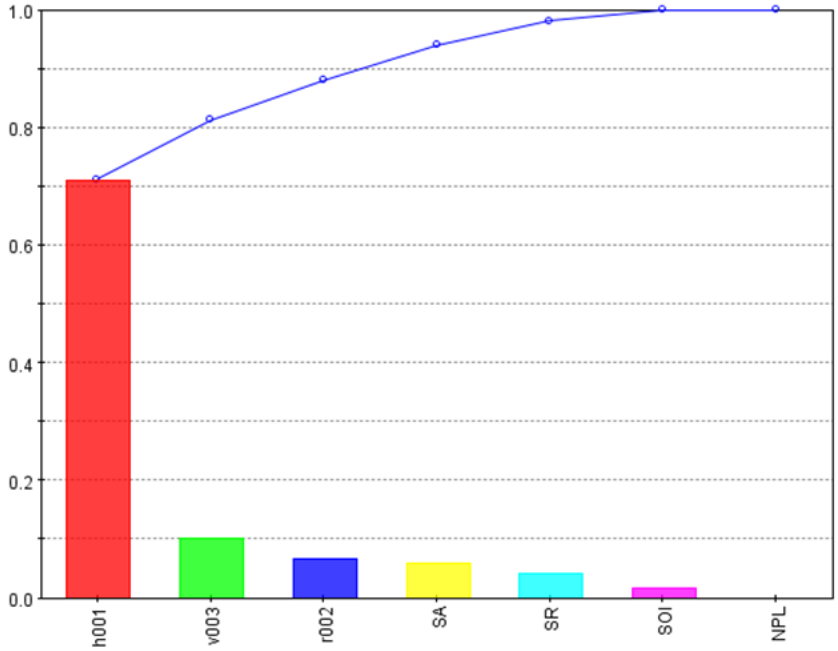

Figure 7-14 Sensitivity of design parameters on soot emissions

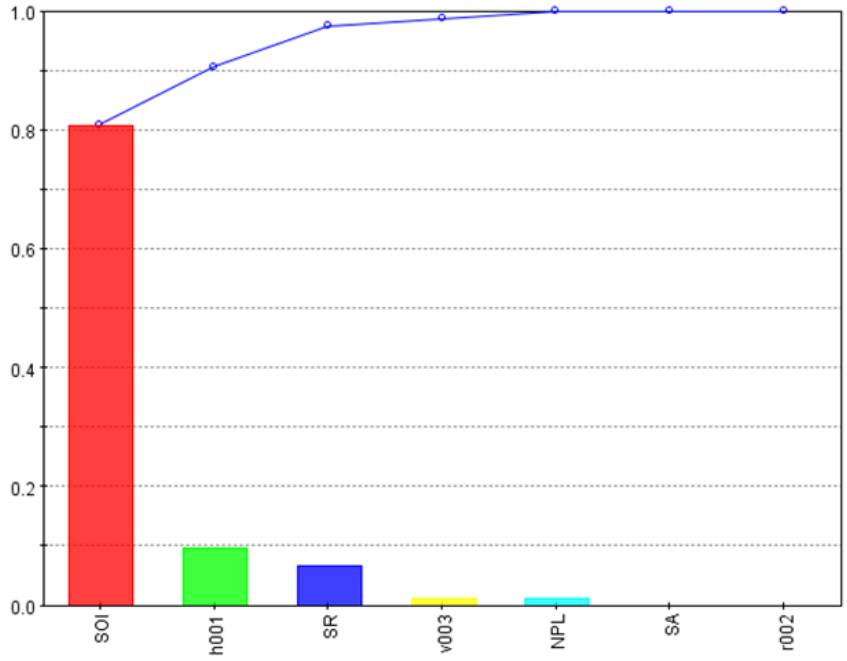

Figure 7-15 Sensitivity of design parameters on SFOC

The RSM contour charts were generated by the effect of these parameters on the sub-objectives, as shown in Figure 7-16. NO_x, soot and SFOC were represented on the first, second and third rows respectively. From the first row, SOI has an approximately uniformly distributed impact on NO_x, i.e. NO_x decreases with an increase in the SOI. The SR has a significant influence when it is larger than two, which greatly deteriorates NO_x emissions. The SFOC increases with an increase of SOI, which is also the most influential factor. The reasons were discussed in the previous section. The second row indicates that a large amount of soot would be generated in the condition of h001 larger than 62mm and v003 lower than 6.8mm.

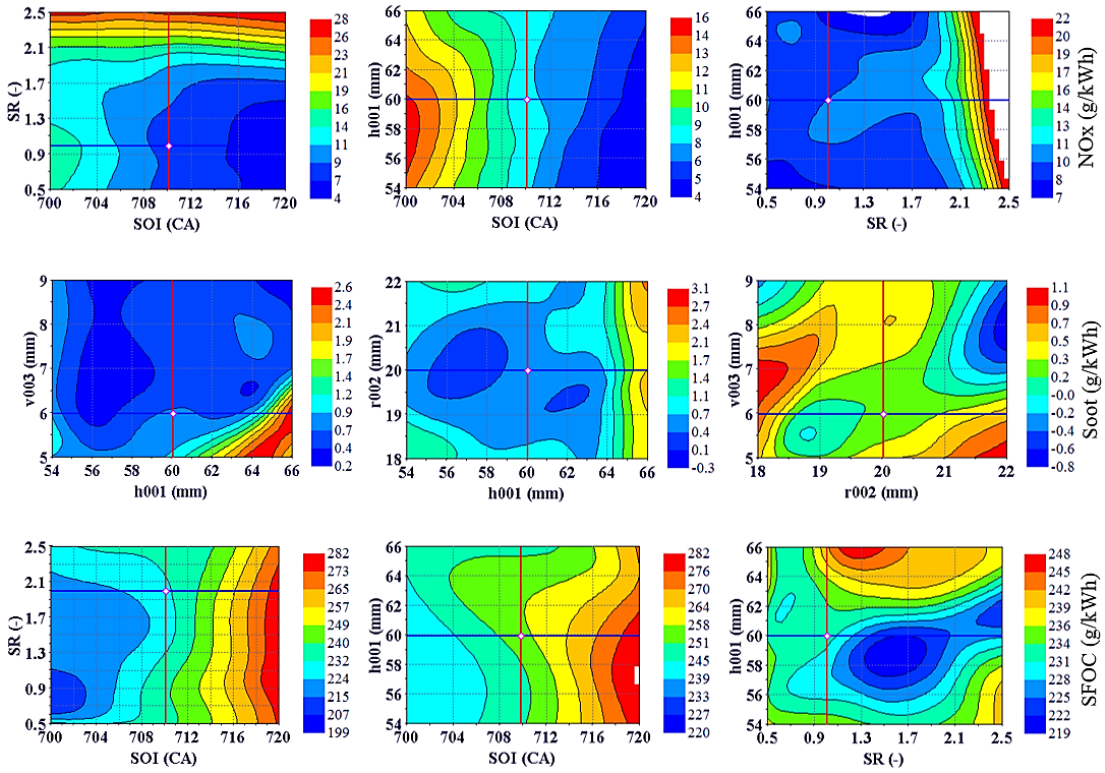

Figure 7-16 RSM contour maps

7.7. Summary

In this chapter, two multi-objective algorithms (NLPQL and MOGA) were introduced for the optimisation of four injection-related parameters and three combustion chamber geometries. It aimed to yield a set of parameters which achieved both a reduction of NO_x and soot emissions, with a slight sacrifice of fuel economy. Two algorithms were compared in four aspects, from optimisation history, objectives and sub-objectives to design parameters. The NLPQL algorithm probably failed to spot the optimal designs may be because of the improper weighting of the objectives. However, MOGA offers more Pareto optimums with a larger diversity and better sub-objectives. The NLPQL algorithm was known to be a local algorithm which heavily relies on the starting point. Thus, the optimal design of MOGA was set as the starting point of the NLPQL algorithm, in order to see whether a better design would result. The optimisation was carried out in a smaller range. Results show a

further reduction of NO_x emissions and soot emissions at the same time, with only a 3.6% rise in SFOC.

In addition, detailed information about the combustion process of the baseline design, optimal design obtained solely by the NLQPL algorithm, optimal design obtained solely by MOGA and the optimal design obtained by the sequential method were presented. Progress comparisons were made on rate of heat release, temperature, NO_x, soot and combustion.

Finally, the RSM method was used to study the sensitivity of the matched parameters on sub-objectives. The results implied that the combustion chamber parameters were the main influencers on soot, which was found by using RSM.

The main outcomes are as follows:

(1) The NLPQL algorithm approached optimal designs faster than MOGA with fewer runs; however, the weights of the merit function should be selected carefully.

(2) The NLPQL algorithm is not that effective when it is used for the optimisation task with seven engine parameters.

(3) MOGA is more time consuming but offers broader and finer solutions. Hence, more Pareto designs are provided and a better design is obtained in each sub-objective than that of the NLPQL algorithm.

(4) If a good starting point was provided by MOGA, the NLPQL algorithm is an effective way for offering a better optimal design.

(5) SOI has the dominant and clearly opposite effect on NO_x and SFOC.

(6) NO_x and soot can be reduced greatly at the same time by adopting late injection, low swirl and large spray angle, but fuel economy is sacrificed

(7) Combustion chamber geometries are influential on soot emissions.

Chapter 8. Conclusions and recommendations

The primary research of this thesis was to predict the emission characteristics and fuel economy when replacing an old mechanical fuel oil injection system with an HPCR one. Two parts of work were reported. In the first part, the effects of structural parameters on injector dynamic response were thoroughly studied. In the second part, the fuel injector calculations with a combustion chamber of a medium-speed marine diesel engine were also thoroughly investigated.

8.1. Summary and Conclusions

In the first part, A practical optimisation routine was proposed for the optimisation of electronic fuel injector structural parameters. This routine was validated on the Type-I fuel injector, and then introduced for the optimisation of the Type-II fuel injector with three additional design parameters. The schedules are as follows:

(1) A model of the Type-I electronic fuel injector was built and validated by the experimental data of the injection rate and injection mass under three different rail pressures.

(2) A parametric study was carried out to examine the effects of the CPD, IPD and OPD on injection characteristics, i.e. injection rate, injection quantity, needle valve lift and control chamber pressure.

(3) An optimisation routine was built in modeFRONTIER for multi-objective optimisation. The Type-I fuel injector model was included and the dynamic response of the valve opening delay and valve closing delay were calculated.

(4) The RSM function charts presented a good agreement with the parametric study. The influence of the electronic fuel injector structural parameters on the dynamic response was analysed by the RSM method.

(5) A Pareto optimum for the Type-I fuel injector with the best trade-off between the valve opening delay and the valve closing delay was selected as the optimum, which achieved a huge reduction of both the valve opening delay and valve closing delay.

(6) A detailed model of the Type-II fuel injector was built in AMESim according to the structural parameters of an actual electronic fuel injector. The proposed optimisation was introduced for the optimisation of the Type-II fuel injector. Three more design parameters were included. The sensitivity of design parameters on the dynamic response was examined before the RSM study in order to simplify analysis. The efficiency and practicality of the proposed optimisation routine were verified again.

The main conclusions for the optimisation of electronic fuel injectors are as follows:

(1) With an increase in control piston diameter and control oil inlet passage diameter, the valve opening delay increased and the valve closing delay reduced. However, the control oil outlet passage diameter seems to only affect the valve opening delay, which decreases with the increase in control oil outlet passage diameter.

(2) NSGA-II is an effective way for optimising the key structural design parameters of the electronic fuel injectors. A clear trade-off was spotted between the valve opening delay and valve closing delay.

(3) A large control piston diameter together with a large control oil inlet passage diameter increases the valve opening delay. However, they contribute to an increase in the valve closing delay, in which the control oil inlet passage diameter has a larger influence than the control piston diameter does. A small control piston diameter and a small control oil inlet passage diameter together lead to a significant increase in the valve closing delay.

(4) A small control piston diameter along with a large control oil outlet passage diameter contributes to a small valve opening delay and vice versa. However, a

small control piston diameter significantly worsens the valve closing delay.

(5) A small control oil inlet passage diameter and a large control oil outlet passage diameter significantly reduces the valve opening delay, and vice versa. The control oil inlet passage diameter has a much greater effect on the valve closing delay than the control oil outlet passage diameter.

(6) The optimum design shows a balanced dynamic response, which achieves considerable reductions of 40% and 25% compared with the baseline design on the valve opening delay and valve closing delay respectively.

(7) The sensitivity analysis shows that the control piston diameter, control oil inlet passage diameter, control oil outlet passage diameter and their interactions are influential factors for the valve opening delay, while the control oil inlet passage diameter has a dominant effect on the valve closing delay. If the same circulation area is guaranteed, the nozzle orifice diameter and nozzle orifice number have less impact on the dynamic response than the control piston diameter, control oil inlet passage diameter and control oil outlet passage diameter.

(8) The RSM function charts and the RSM contour maps disclosed that the influence of the control piston diameter, control oil inlet passage diameter and control oil outlet passage diameter of the Type-II fuel injector on the dynamic response is consistent with that of the Type-I fuel injector. In addition, they also indicated that the effects of the spring preload force on the valve closing delay are surprising noticeable under low rail pressure conditions. The valve closing delay decreases with the increase in the spring preload force.

(9) The dynamic response of the optimal design of Type-II fuel injector achieves a considerable reduction for three different rail pressures (80 MPa, 120 MPa and 160 MPa). More specifically, the valve opening delay was reduced by 29.8%, 29.2% and 20.8%, and the valve closing delay was reduced by 25.6%, 24.5% and 30.1% respectively.

In the second part, the study of the Type-II fuel injector match with the combustion chamber of a medium-speed marine diesel engine were investigated. A parametric study was carried out to investigate the effects of four injection-related parameters and three combustion chamber geometry parameters on NO_x emissions, soot emissions and SFOC respectively. Additionally, seven engine parameters were investigated by using the NLPQL algorithm and MOGA separately and together. Comparisons were made on objectives, sub-objectives, design parameters and detailed combustion process. Then, RSM was used to gain a better understanding of the influence of the design parameters on emissions and fuel consumption. The schedules are as follows:

(1) A CFD model was built and a parametric study was conducted under three engine loads in order to gain a better understanding of how the design parameters of the Type-II fuel injector and the combustion chamber geometries affect the emissions and fuel economy.

(2) The NLPQL algorithm and MOGA method were compared on four aspects: optimisation history, objectives, design parameters and combustion process. By doing this, the efficiency of multi-objectives algorithms for engine match optimisation were investigated.

(3) The optimal design of MOGA was set as the starting point of the NLPQL algorithm in order to search for a better design and examine whether a good starting point is crucial or not.

(4) The interactions and influence of the design parameters on emissions and fuel consumption were examined by RSM.

(5) The combustion process of optimums obtained by different optimisation methods were compared in detail to understand the reasons behind their performance.

The main conclusions found in the second part are as follows:

(1) NOx increases with an increase in the spray angle, while both the soot emissions and SFOC decrease.

(2) NOx emissions decrease with an increase in the nozzle protrusion length. In contrast, soot emissions and SFOC increase with an increase in the nozzle protrusion length.

(3) With the increase in injection timing BTDC, a consistent increasing trend of the NOx emissions is observed. In contrast, an opposite decreasing trend is observed in the case of the SFOC. The NOx emissions at 20 degrees BTDC are approximately three times higher than at the TDC. The SFOC decreased by nearly 20% from the TDC to 20 degrees BTDC. Soot emissions decrease slightly with an increase in the injection timing.

(4) The NOx emissions increase with an increase in the swirl ratio at high loads. However, the NOx emissions remain nearly the same at low loads. For soot emissions, an increasing trend is observed as the swirl ratio increases. The SFOC reports an increasing trend at low loads. However, the SFOC is not affected much by the swirl ratio at high loads.

(5) The NOx emissions increase with an increase in the bowl diameter and reach a peak when the bowl diameter is about 120 mm before they gradually decline. An opposite trend is witnessed for the SFOC. Soot emissions decrease in line with an increase in the bowl diameter and reach lowest value when the bowl diameter is 120 mm, then increase to nearly three times of their original value.

(6) The centre crown height has little effect on emissions and fuel consumption.

(7) NOx emissions slightly increase with an increase in the toroidal radius. Soot emissions and SFOC decrease with an increase in the toroidal radius.

(8) The NLPQL algorithm approached optimal designs faster than MOGA with fewer runs; however, the weights of the merit function should be selected

carefully.

(9) The NLPQL algorithm is not that effective when it is used for the optimisation task with seven engine parameters.

(10) MOGA is more time consuming but offers broader and finer solutions. Hence, more Pareto designs are provided and a better design is obtained in each sub-objective than that of the NLPQL algorithm.

(11) If a good starting point was provided by MOGA, the NLPQL algorithm is an effective way for offering a better optimal design.

(12) SOI has the dominant and clearly opposite effect on NO_x and SFOC.

(13) NO_x and soot can be reduced greatly at the same time by adopting late injection, low swirl and large spray angle, but fuel economy is sacrificed

(14) Combustion chamber geometries are influential on soot emissions.

8.2. Recommendations for the future work

Based on the study in this thesis, the following suggestions are recommended for future study:

(1) The model of the Type-II electronic fuel injector to be validated by injection rate data. If the experimental facilities are available for injection rate measuring in the future, the experiments will be fulfilled.

(2) The optimisation routine proposed for the optimisation of fuel injectors can also be extended for the optimisation of other components, i.e. high-pressure pump, high-pressure-tube and even the whole HPCR system.

(3) The merit function weights of the NLPQL algorithms were chosen according to the author's experience and the literature. How the weights affect the merit function and the optimisation process are worth investigating.

Funding

This work was supported by the project ‘An Investigation into the Characteristics of High-pressure Common Rail Injection System’ from Lloyds Register of Shipping of UK and the project ‘Engineering Development of a Medium-Speed Dual Fuel Engine (Ministry of Industry and Information Technology NO. (2013) 412, 2)’ from China.

Publications

1. **Nao Hu***, Peilin Zhou, Jianguo Yang. Comparison and combination of NLPQL and MOGA algorithms for a marine medium-speed diesel engine optimisation. *Energy Conversion and Management* 2017; 133: 138-152.

2. **Nao Hu***, Jianguo Yang, Peilin Zhou. Study of the impact of structural parameters on the dynamic response of an electronic fuel injector. *Energy Conversion and Management* 2017; 136: 202-219.

3. **Nao Hu***, Peilin Zhou, Jianguo Yang. Reducing emission by optimising the fuel injector matching with the combustion chamber geometry for a marine medium-speed diesel engine. *Transportation Research Part D: Transport and Environment* 2017; 53: 1-16.

4. **Nao Hu***, Jianguo Yang, Peilin Zhou. Optimisation of injection-related parameters under different engine loads by using the NLPQL algorithm. *Internal Journal of Engine Research* 2017; 1-14.

5. **Nao Hu***, Jianguo Yang, Peilin Zhou. Sensitivity analysis of the dynamic response of an electronic fuel injector regarding fuel properties and operating conditions. *Applied Thermal Engineering*. Accepted.

References

[1] Goldsworthy L. Design of Ship Engines for Reduced Emissions of Oxides of Nitrogen. Available from: www.flamemarine.com. Visiting date: 03-03-2017.

[2] International Maritime Organization. (2008). Annex VI of MARPOL 73/78 an NO_X Technical Code. London.

[3] MEPC 58/23/Add. 1, Annex 13: Resolution MEPC. 176 (58), Adopted on 10 October 2008.

[4] Murayama Y., Tagai T., Takahisa M., Goto S. (2013). Demonstration of emission control technology for IMO NO_x Tier III. *CIMAC Congress* 2013, shanghai, paper no: 127.

[5] Christer W. (2013). Tier III technology development and its influence on ship installation and operation, *CIMAC Congress* 2013, Shanghai, paper no: 159.

[6] Pueschel M., Buchholz B., Fink C., Ricket C., Ruschmeyer K. (2013). Combination of post-injection and cooled EGR at a medium-speed diesel engine to comply with IMO Tier III emission limits. *CIMAC Congress* 2013, shanghai, paper no: 76.

[7] Steffe P., Liepert K., Losher R., Bader I. (2013). High performance solutions for IMO TIER III -system integration of engine and after treatment technologies as element of success. *CIMAC Congress* 2013, shanghai, paper no: 212.

[8] Darby S.M. (2014). Top automotive innovations: History of fuel oil injection. Available form: http://bestride.com/blog/top-automotive-innovations-history-of-fuel-injection/2780/. Visiting date: 26-12-2016.

[9] Armstrong J. (2004). Electronic fuel oil injection: A history lesson. Available form: http://www.autonews.com/article/20040823/SUB/408230807/electronic-fuel-injection:-a-history-lesson. Visiting date: 21-12-2016.

[10] Huber, R., (1969). Electromagnetic fuel-injection valve, US Patent 3464627. Available form: http://www.google.com/patents/US3464627. Visiting date: 03-01-2017.

[11] Industriemuseum S. (2010). Versuchsmotor mit Common Rail-Einspritzsystem. Available form: http://www.saechsisches-industriemuseum.de/c1/c1/redaktion?latestVersion=true&workshop=-1&URLID=6213. Vising date: 03-01-2017.

[12] Williams, D.L. (1982). Electromagnetic diesel fuel injector. US Patent 4360163. Available from: http://www.google.com/patents/US4360163. Visiting date: 03-01-2017.

[13] Miyaki, M., Fujisawa H., Masuda A., Yamamoto Y. (1991). Development of new electronically controlled fuel oil injection system ECD-U2 for diesel engines, *SAE Technical Paper*, 910252, doi:10.4271/910252.

[14] Jääskeläinen H., Khair M.K. (2015). Common rail fuel oil injection. Available form: https://www.dieselnet.com/tech/diesel_fi_common-rail.php. Visiting date: 05-01-2017.

[15] Breitbach, H., (2002). Fuel oil injection systems Overview. Delphi Corporation.

[16] Catania A.E., Ferrari A. (2012). Development and performance assessment of the new-generation CF fuel injection system for diesel passenger cars. Applied Energy, 91: 483-495.

[17] Ping T., Fang W.C., Pu W.H. (2009). The development of high pressure common rail systems for marine diesel engines. *Shanghai Ship Building*, (3): 34-37.

[18] MAN Diesel & Turbo Common Rail - Design & Field Experience. Available from: chrome-extension://ikhdkkncnoglghljlkmcimlnlhkeamad/pdf-viewer/web/viewer.html?file=https%3A%2F%2Fmarine.man.eu%2Fdocs%2Flibrariesprovider6%2F4-Stroke-Engines%2Fcommon-rail-design.pdf%3Fsfvrsn%3D6. Visiting date:12-01-2017.

[19] Ganser M., Moser U., Hauger L. (2007). New Common Rail Systems suited for Diesel Engines from 1 to 5 Megawatt: modeling simulations and hardware results. *CIMAC Congress* 2007, paper no: 70.

[20] Stiesch G., Baumann H., Wachter V., Schmitz J., Teetz C. (2007). Utilizing multiple injections for optimized performance and exhaust emissions with the MTU series 2000 common rail marine engines. *CIMAC Congress* 2007, paper no: 50.

[21] Xu J.L. (2004). Diesel engines electronic Injection Technology. China. Communication Press. 279-292.

[22] Seykens X.L.J., Somers L.M.T., Baert R.S.G. (2005). Detailed modeling of common rail fuel oil injection process. *MECCA*, 3(2-3): 30-39.

[23] Kim J., Jo I., Sung G., Chung J., Jeong S., Lee J. (2005). Experimental investigation of spray and combustion characteristics by direct needle-driven diesel injector in a CRDi Engine. *SAE International*, 2015-01-0004.

[24] Molina S., Salvador F.J., Carreres M., Jaramillo D. (2014). A computational investigation on the influence of the use of elliptical orifices on the inner nozzle flow and cavitation development in diesel injector nozzles. *Energy Conversion and Management*, 79: 114-127.

[25] Benajes J., Pastor J.V., Payri R., Plazas A.H. (2004). Analysis of the influence of diesel nozzle geometry in the injection rate characteristics. *J. Fluids Eng.*, 126: 63-71.

[26] Payri R., Garcia J.M., Salvador F.J., Gimeno J. (2005). Using spray momentum flux measurements to understand the influence of diesel nozzle geometry on spray characteristics. *Fuel*, 84: 551-561.

[27] Han J.S., Lu P.H., Xie X.B., Lai M.C., Henein N.A. (2002). Investigation of diesel spray primary breakup and development for different nozzle geometries. *SAE Paper*, 2002-01-2775.

[28] He Z., Zhong W., Wang Q., Jiang Z., Fu Y. (2013). An investigation of transient nature of the cavitating flow in injector nozzles. *Applied Thermal Engineering*, 54: 56-64.

[29] Moon S., Gao Y., Park S., Wang J., Kurimoto N., Nishijima Y. (2015). Effect of the number and position of nozzle holes on in- and near-nozzle dynamic characteristics of diesel injection. *Fuel*, 150: 112-122.

[30] Salvador F.J., Martínez-López J., Caballer M., De Alfonso C. (2013). Study of the influence of the needle lift on the internal flow and cavitation phenomenon in diesel injector nozzles by CFD using RANS methods. *Energy Conversion and Management*, 66: 246-256.

[31] Salvador F.J., Gimeno J., De la Morena J., Carreres M. (2012). Using one-dimensional modeling to analyze the influence of the use of biodiesels on the dynamic behavior of solenoid-operated injectors in common rail systems: Results of the simulations and discussion. *Energy Conversion and Management*, 54: 122-132.

[32] Wang C., Li G.X., Sun Z.Y., et al. (2016). Effects of structure parameters on flow and cavitation characteristics within control valve of fuel injector for modern diesel engine. *Energy Conversion and Management*, 124: 104-115.

[33] Beccari S., Pipitone E., Cammalleri M., Genchi G. (2014). Model-based optimization of injection strategies for SI engine gas injectors. *Journal of Mechanical Science and Technology*, 28 (8): 3311-3323.

[34] Cheng Q., Zhang Z.D., Xie N.L. (2015). Power losses and dynamic response analysis of ultra-high-speed solenoid injector within different driven strategies. *Applied Thermal Engineering*, 91: 611-621.

[35] Salvador F.J., Gimeno J., Carreres M., Crialesi-Esposito M. (2016). Fuel temperature influence on the performance of a last generation common-rail diesel ballistic injector. Part I: Experimental mass flow rate measurements and discussion. *Energy Conversion and Management*, 114: 364-375.

[36] Payri R., Salvador F.J., Carreres M., DelaMorena J. (2016). Fuel temperature influence on the performance of a last generation common-rail diesel ballistic injector. Part II: 1D model development, validation and analysis. *Energy Conversion and Management*, 114: 376-391.

[37] Seykens X.L.J., Somers L.M.T., Baert R.S.G. (2005). Detailed modelling of common rail fuel oil injection process. *J Middle Eur Construct Des Cars (MECCA)*, 3: 30-39.

[38] Rahim R., Mamat R., Taib M.Y., Abdullah A.A. (2012). Influence of fuel temperature on diesel engine performance operating with biodiesel blend. *J Mech Eng Sci.*, 2: 226-36.

[39] Payri R., Salvador F.J., Martí-Aldaraví P., Martínez-López J. (2012). Using one-dimensional modelling to analyse the influence of the use of biodiesels on the dynamic behaviour of solenoid-operated injectors in common rail systems: Detailed injection system model. *Energy Conversion and Management*, 54: 90-99.

[40] Salvador F.J., Plazas A.H., Gimeno J., Carreres M. (2014). Complete modelling of a piezo actuator last-generation injector for diesel injection systems. *International J of Engine Research*, 15 (1): 3-19.

[41] Shi X.Y. (2007). Study on influence of fuel oil injection strategy on performance and exhaust emission of diesel engine, Shandong University Doctoral Dissertation.

[42] Stiesch G. Modeling Engine Spray and Combustion Processes. Available from: https://link.springer.com/chapter/10.1007/978-3-662-08790-9_3. Visiting data: 17-09-2017.

[43] SCRYU. Available from: http://www.cradle-cfd.com/products/sctetra/index.html. Visiting date: 11-09-2017.

[44] PowerFLOW. Available from: http://www.pwrfs.com/powerflow/. Visiting date: 11-09-2017.

[45] ANSYS Fluent. Available from: http://www.ansys.com/Products/Fluids/ANSYS-Fluent. Visiting date: 11-09-2017.

[46] STAR-CD. Available from: http://mdx.plm.automation.siemens.com/star-cd. Visiting date: 11-09-2017.

[47] AVL FIRE™, Available from: https://www.avl.com/fire2/-/asset_publisher/gYjUpY19vEA8/content/avl-fire-?inheritRedirect=false&redirect=https%3A%2F%2Fwww.avl.com%3A443%2Ffire2%3Fp_

p_id%3D101_INSTANCE_gYjUpY19vEA8%26p_p_lifecycle%3D0%26p_p_state%3Dnormal%26p_p_mode%3Dview%26p_p_col_id%3Dcolumn-2%26p_p_col_count%3D1. Visiting date: 08-03-2017.

[48] Taghavifar H., Khalilarya S., Jafarmadar S. (2014). Engine structure modifications effect on the flow behavior, combustion, and performance characteristics of DI diesel engine. *Energy Conversion and Management*, 85: 20-32.

[49] Park S. (2012). Optimisation of combustion chamber geometry and engine operating conditions for compression ignition engines fueled with dimethyl ether. *Fuel*, 97: 61-71.

[50] Mobasheri R., Peng Z. (2012). Analysis of the effect of re-entrant combustion chamber geometry on combustion process and emission formation in a HSDI diesel engine. *SAE International*, 2012-01-0144.

[51] Senecal P. K. and Reitz R.D. (2000). Simultaneous reduction of engine emissions and fuel consumption using genetic algorithms and multi-dimensional spray and combustion modelling. *SAE Technical Paper Series*, 2000-01-1890.

[52] Shi Y., Reitz R.D. (2008). Optimisation study of the effects of bowl geometry, spray targeting, and swirl ratio for a heavy-duty diesel engine operated at low and high load. *Int. J. Engine Res.*, 9: 325-346.

[53] Taghavifar H., Jafarmadar S., Taghavifar H., Navid A. (2016). Application of DOE evaluation to introduce the optimum injection strategy-chamber geometry of diesel engine using surrogate epsilon. *Applied Thermal Engineering*, 106: 56-66.

[54] Jeong S., Obayashi S., Minemura Y. (2008). Application of hybrid evolutionary algorithms to low exhaust emission diesel engine design. *Eng Optimization*, 40(1): 1-16.

[55] Chen Y. and Lv L. (2014). The multi-objective optimisation of combustion chamber of DI diesel engine by NLPQL algorithm. *Applied Thermal Engineering*, 73(1): 1332-1339.

[56] Taghavifar H, Jafarmadar S, Taghavifar H, Navid A. Application of DoE evaluation to introduce the optimum injection strategy-chamber geometry of diesel engine using surrogate epsilon-SVR. Applied Thermal Engineering 2016, 106: 56-66.

[57] Cioppa TM, Lucas TW. (2007). Efficient Nearly Orthogonal and Space-Filling Latin Hypercubes. Technometrics, 49(1): 45-55.

[58] Senecal P.K., Pomraning E., Richards K.J. (2002). Muti-mode genetic algorithm optimization of combustion chamber geometry for low emissions. *SAE 2002 World Congress*, 2002-01-0958.

[59] Holland J.H. (1975). Adaptation in natural and artificial systems. Ann Arbor: University of Michigan Press.

[60] Gen M., Cheng R. (1997). Genetic algorithms and engineering design. London: Wiley.

[61] Goldberg D.E. (1989). Genetic algorithms in search, optimization and machine

learning. Addison Wesley Publishing Company Inc.

[62] Abdullah K., David W.C., Alice E.S. (2006). Multi-objective optimization using genetic algorithms: A tutorial. *Reliability Engineering and System Safety*, 91: 992-1007.

[63] Deb K., Pratap A., Agarwal S., Meyarivan T. (2002). A fast and elitist multiobjective genetic algorithm: NSGA-II. *Evol Comput*, 6(2): 182-197.

[64] Schittkowski K. (1985). NLPQL: A fortran subroutine solving constrained nonlinear programming problems. *Annals of operations research*, 5(6): 485-500.

[65] Ali O.M., Mamat R., Najafi G., Yusaf T., Ardebili S.M.S. (2015). Optimization of biodiesel-diesel blended fuel properties and engine performance with ether additive using statistical analysis and response surface methods. *Energies*, 8(12): 14136-14150.

[66] Taghavifar H., Taghavifar H., Mardani A., Mohebbi A. (2014). Modeling the impact of in-cylinder combustion parameters of DI engines on soot and NO_x emissions at rated EGR levels using ANN approach. *Energy Conversion and Management*, 87: 1-9.

[67] Taghavifar H., Taghavifar H., Mardani A., Mohebbi A., Khalilarya S. Jafarmadar S. (2015). On the modeling of convective heat transfer coefficient of hydrogen fueled diesel engine as affected by combustion parameters using a coupled numerical-artificial neural network approach. *International journal of hydrogen energy*, 40(12): 4370-4381.

[68] Taghavifar H., Taghavifar H., Mardani A., Mohebbi A. Khalilarya S. (2015). A numerical investigation on the wall heat flux in a DI diesel engine fueled with n-heptane using a coupled CFD and ANN approach. *Fuel*, 140: 227-236.

[69] Poles S., Lovison A. (2006). Shepard's and k-nearest's methods in the newly implemented response surfaces. *Technical Report*, 2006-004.

[70] User manual of modeFRONTIER, 2014.

[71] Tosun E., Aydin K., Bilgili M. (2016). Comparison of linear regression and artificial neural network model of a diesel engine fueled with biodiesel-alcohol mixtures. *Alexandria Engineering Journal*, 55(4): 3081-3089.

[72] Isermann R., Schaffnit J., Sinsel S. (1999). Hardware-in-the-loop simulation for the design and testing of engine-control systems. *Control Engineering Practice*, 7: 643-653.

[73] Wu H., Li M.F. (2016). A Hardware-in-the-Loop (HIL) Bench Test of a GT-Power Fast Running Model for Rapid Control Prototyping (RCP) Verification. *SAE Technical Paper*, 2016-01-0549.

[74] Yang, X., Zhu G. (2011). A Two-zone Control Oriented SI-HCCI hybrid Combustion Model for the HIL Engine Simulation. *American Control Conference (ACC)*, 973-978.

[75] Saad, C., Maroteaux, F., Millet, J., Aubertin, F. (2011). Combustion Modeling of a Direct Injection Diesel Engine Using Double Wiebe Functions: Application to HiL Real-Time Simulations. *SAE Technical Paper*, 2011-24-0143.

[76] Schuette H., Ploeger M. (2007). Hardware-in-the-Loop Testing of Engine Control Units - A Technical Survey. *SAE International*, 2007-01-0500.

[77] Klaus Lamberg D.M., Peter Wältermann D.I. (2000). Using HIL Simulation to test Mechatronic Components in Automotive Engineering. *2nd Congress on "Mechatronik im Automobil" Haus der Technik*, Munich, 15/16.

[78] LMS Imagine.Lab Amesim. Available form: https://www.plm.automation.siemens.com/en/products/lms/imagine-lab/amesim/. Visiting date: 11-09-2017.

[79] modeFRONTIER. Available from: http://www.esteco.com/modefrontier. Visiting date: 11-09-2017.

[80] Payri R., Salvador F.J., Carreres M., De la Morena J. (2016). Fuel temperature influence on the performance of a last generation common-rail diesel ballistic injector. Part II: 1D model development, validation and analysis. *Energy Conversion and Management*, 114: 376-391.

[81] Shi Y., Reitz R.D. (2008). Assessment of optimization methodologies to study the effects of bowl geometry, spray targeting and swirl ratio for a heavy-duty diesel engine operated at high-load. *SAE Int. J. Engines*, 1(1): 537-557.

[82] Payri R., Salvador F.J., Carreres M., De la Morena J. (2016). Fuel temperature influence on the performance of a last generation common-rail diesel ballistic injector. Part II: 1D model development, validation and analysis. *Energy Conversion and Management*, 114: 376-391.

[83] LABCAR Component Overview HiL Systems. Available from: https://www.etas.com/en/products/solutions_labcar_component_overview.php?langS=true&. Visiting data: 13-09-2017.

[84] Chawner J. (2013). Quality and Control -Two Reasons Why Structured Grids Aren't Going Away. Available from: http://www.pointwise.com/theconnector/March-2013/Structured-Grids-in-Pointwise.shtml. Visiting data: 13-05-2017.

[85] Chatterjee A. (2004). Novel multi-block strategy for CAD tools for microfluidics type applications. *Advances in Engineering Software*, 35: 443-451.

[86] Hanjalic K, Popovac M, Hadziabdic M. (2004). A robust near-wall elliptic relaxation eddy-viscosity turbulence model for CFD. *Int J Heat Fluid Flow*, 25: 1047-1051.

[87] Popovac M and Hanjalic K. (2007). Compound wall treatment for RANS computation of complex turbulent flows and heat transfer. *Flow Turbul Combustion*, 78: 177-202.

[88] Issa RI. (1985). Solution of the implicit discretised fluid flow equations by operator splitting. *J Comput Phys*, 62: 45-60.

[89] Emans M. (2009). AMG for Linear Systems in Engine Flow Simulations. *PPAM 2009*, Part II, LNCS 6068, 350-359.

[90] Dukowicz JK. (1997). Quasi-steady droplet change in the presence of convection. *Los Alamos Scientific Laboratory*, LA7997-MS.

[91] Liu A, Mather D, Reitz RD. (1993). Modelling the effects of drop drag and breakup on fuel sprays, *SAE Technical Paper*, DOI: 10. 4271/930072.

[92] Reitz RD. (1987). Modelling atomization processes in high-pressure vaporizing sprays, *Atomization and Spray Technology*, 3: 309-337.

[93] Naber JD and Reitz RD. (1988) Modelling engine spray/wall impingement. *SAE Technical Paper*, 880107.

[94] Cabrera E and Gonzalez JE. (2003). Heat flux correlation for spray cooling in the nucleate boiling regime. *Exp Heat Transf*, 16: 19-44.

[95] Spalding DB. (1971). Mixing and chemical reaction in steady confined turbulent flames. *Symp (Int) Combust*, 13(1): 649-657.

[96] Magnussen BF and Hjertager BH. (1997). On mathematical modelling of turbulent combustion with special emphasis on soot formation and combustion. *Symp (Int) Combust*, 16(1): 719-729.

[97] Zeldovich YA, Frank-Kamenetskii D, Sadovnikov P. (1947). The oxidation of nitrogen in combustion and explosions. *Publishing House of the Academy of Sciences of USSR*.

[98] Wang H and Frenklach M. (1997). A detailed kinetic modelling study of aromatics formation, growth and oxidation in laminar premixed ethylene and acetylene flames. *Combust Flame*, 110: 173-221.

[99] Apple J, Bockhorn H, Frenklach M. (2000). Kinetic modelling of soot formation with detailed chemistry and physics: laminar premixed flames of C2 hydrocarbons. *Combust Flame*, 121: 122-136.

[100] Balthasar M and Frenklach M. (2005). Detailed kinetic modelling of soot aggregate formation in laminar premixed flames. *Combust Flame*, 140: 130-145.

[101] Navid A., Khalilarya S., Taghvifar H. (2016). Comparing multi-objective non-evolutionary NLPQL and evolutionary genetic algorithm optimisation of a DI diesel engine: DOE estimation and creating surrogate model. *Energy Conversion and Management*, 126: 385-399.

[102] User guide of design of experiments and optimisation. (2013). Version 2013. Austria: AVL LIST GmbH.

[103] Soteriou C., Smith M., Andrews R. (1995). Direct injection diesel sprays and the effects of cavitation and hydraulic flip on atomization. *SAE Paper*, 950080.

[104] Poles S., Lovison A. (2006). Shepard's and k-nearest's methods in the newly implemented response surfaces. Technical Report, 2006-004.

[105] Nikoskinen T. (2015). From neural networks to deep neural networks. Aalto University School of Science.

[106] Taghavifar H., Khalilarya S., Jafarmadar S. (2014). Diesel engine spray characteristics prediction with hybridized artificial neural network optimized by genetic algorithm. Energy, 71: 656-664.

[107] Levenberg K. (1994). A method for the solution of certain problems in least squares, Quarterly of Applied Mathematics, 5: 164-168.

[108] Marquardt D. (1963). An algorithm for least-squares estimation of nonlinear parameters, SIAM Journal on Applied Mathematics, 11(2): 431-441.

Appendix A: Modelling of Type-I fuel injector

Assumptions of the model

For the Type-I fuel injector model used in Chapter 3, the following assumptions were made: a) all the variations are isothermal, so, the fuel temperature was assumed to be constant along the injector and equal to the one at the injector inlet. b) the fuel property was considered to be constant [36]. 3) a constant pressure source was adopted here to simulate the pressure from the high-pressure pump, thus neglecting the pressure fluctuations caused by the periodical oil supply from the high-pressure pump. 4) the pressure wave propagation was not considered in the model.

1D model of the Type-I fuel injector

The Type-I electronic fuel injector used in Chapter 3 was from a standard second generation common rail fuel oil injection system. It has a conical type of orifices. The 1D model was built in AMESim according to the reference [39]. The structure and the 1D model of the Type-I fuel injector are shown in **Error! Reference source not found.** and **Error! Reference source not found.**.

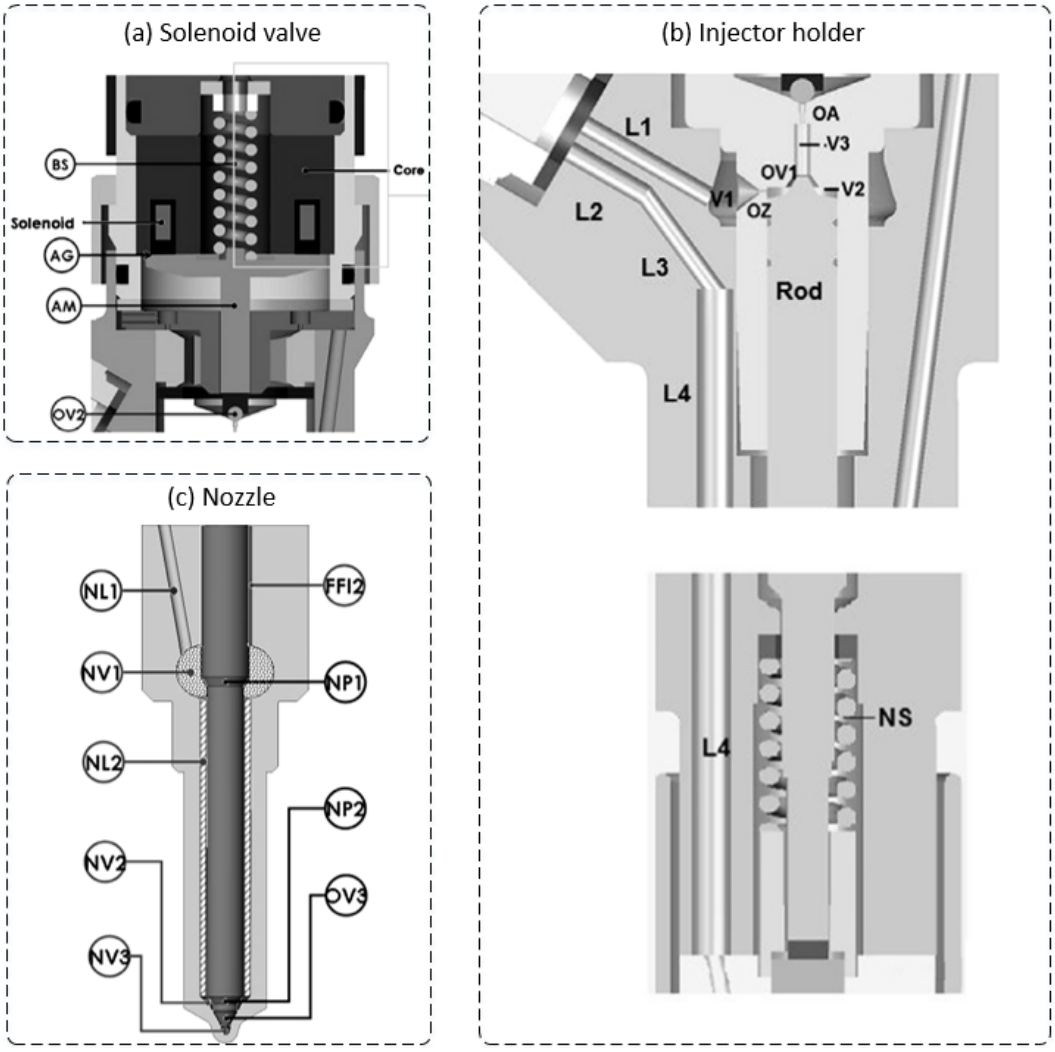

Figure 0-1 Structural view of the Type-I electronic fuel injector

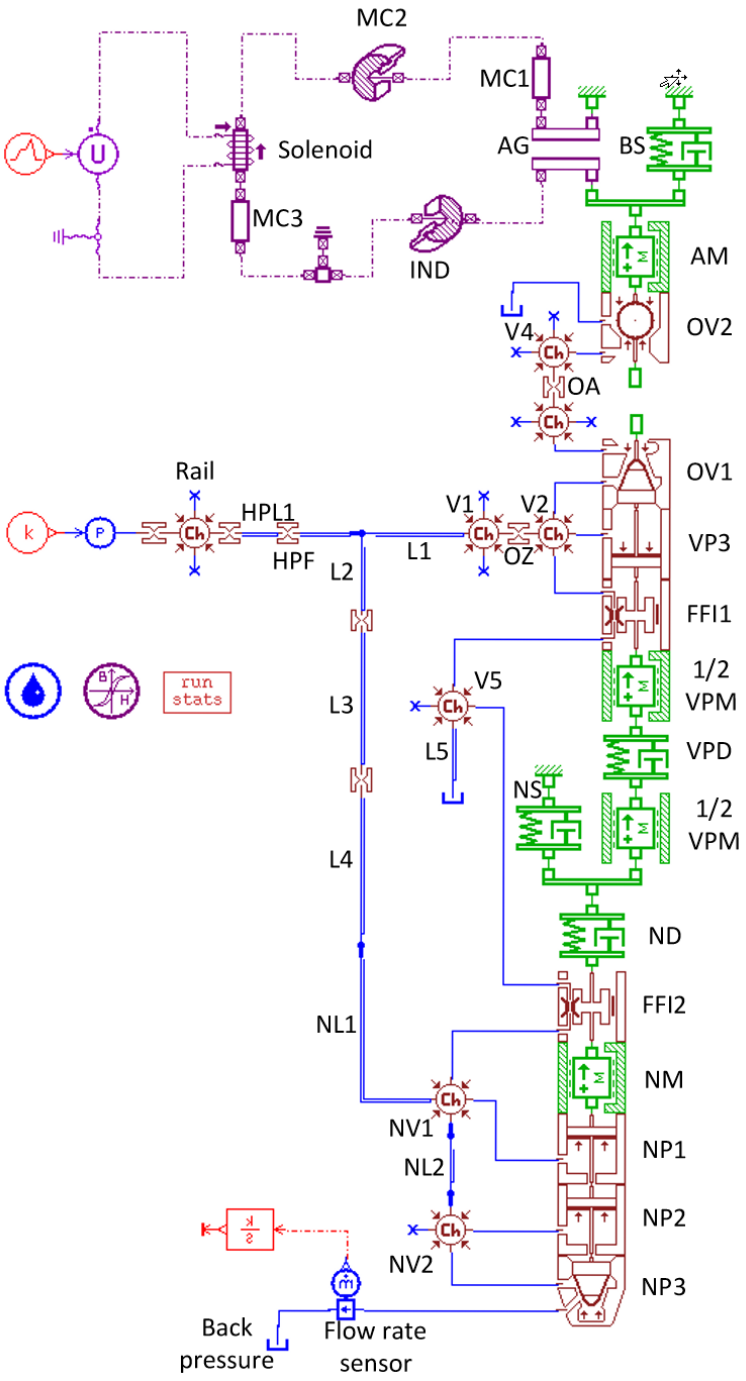

Figure 0-2 1D model of the Type-I electronic fuel injector

The parameters fed into injector model are also from Payri et al. [39] (see **Error! Reference source not found.** to **Error! Reference source not found.**). These detailed parameters of the fuel injector were obtained by Payri et al. [39] through silicone moulds and scanning electron microscope (SEM) technologies. The

geometry of the volumes and internal channels as well as the dimensions of the control passages and nozzle orifices were determined by silicone molds. Images were taken in the microscope and processed in CAD software with a reference dimension.

Table 0-1 Parameters for the solenoid valve model [39]

Element	Length (mm)	Mass (g)	Area (mm^2)	No. Coils	Resis-tor	Spring rate (N/m)	Resistor (Ω)
Solenoid	-	-	-	32	0.46	-	-
MC1	23.32	-	89.34	-	-		
MC2	6.5	-	-	-	-	-	-
MC3	23.32	-	89.34	-	-		
IND	6.5	-	-	-	-	-	-
AG	0.075	-	86.55	-	-	-	-
AM	-	5.9	-	-	-	-	-
BS	-	-	-	-	-	69000	10

Table 0-2 Parameters for the injector holder model [39]

Element	Length (mm)	Diameter (mm)	Volume (cm3)	Mass (g)	Spring rate (N/m)	Dumper rating (N/(m/s))
OV2	-	0.385	-	-	-	-
V4	-	-	5.65E-05	-	-	-
OA	-	0.246	-	-	-	-
V3	-	-	2.3E-.	-	-	-
Rail	-	-	24	-	-	-
HPL1	90	2.5	-	-	-	-
HPF	1	-	-	-	-	-
L1	7.57	1.44	-	-	-	-
V1	-	-	0.125	-	-	-
OZ	-	0.216	-	-	-	-
V2	-	-	0.0115	-	-	-
L2	7.22	1.22	-	-	-	-
L3	3.39	1.11	-	-	-	-
L4	115	2.16	-	-	-	-
V5	-	-	0.115	-	-	-
L5	58	1.35	-	-	-	-
1/2 VPM	-	-	-	6.43	-	-
VPD	-	-	-	-	28100000	50
NS	-	-	-	-	24093	25

Table 0-3 Parameters for the nozzle model [39]

Element	Length (mm)	Diameter (mm)	Volume (cm^3)	Mass (g)	Spring rate (N/m)	Damper rating (N/(m/s))
NL1	15	2.16	-	-	-	-
FFI2	12.6	4	-	-	-	-
NV1	-	-	0.032	-	-	-
NM	-	-	-	3.1	-	-
NP1	-	4	-	-	-	-
NL2	27	2.4	-	-	-	-
NV2	-	-	0.005	-	-	-
NP2	-	3.04	-	-	-	-
OV3	-	0.57	-	-	-	-
NV3	-	-	5.84E-05	-	-	-
ND	-	-	-	-	39330000	50
Orifices	-	0.13	-	-	-	-

The discharge coefficient of the control oil inlet passage, control oil outlet passage and nozzle orifices were test as a function of the pressure drop. It can be calculated by using equation (A.1).

$$C_d = \frac{\dot{m}_j}{A_0 \sqrt{2\rho_f (P_{inj} - P_b)}} \tag{A.1}$$

Where, C_d is the discharge coefficient, $\dot{m}_j$ is the mass flow rate, A_0 is the geometrical cross section of the passage or orifice, ρ_f is the liquid density, P_{inj} is the injection pressure and P_b is the ambient pressure.

The tests were carried out by Payri et al. [39] and results are shown in **Error! Reference source not found.** and **Error! Reference source not found.**.

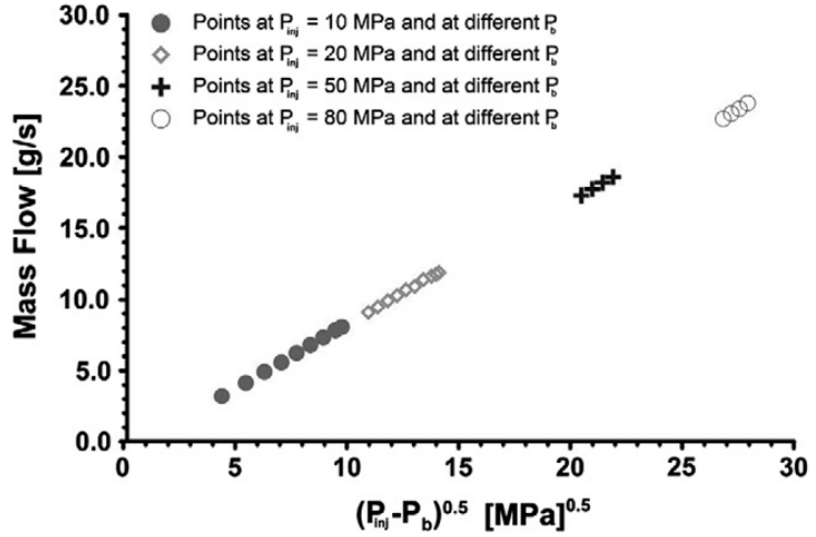

Figure 0-3 Mass flow against square root of pressure drop for the nozzle orifices

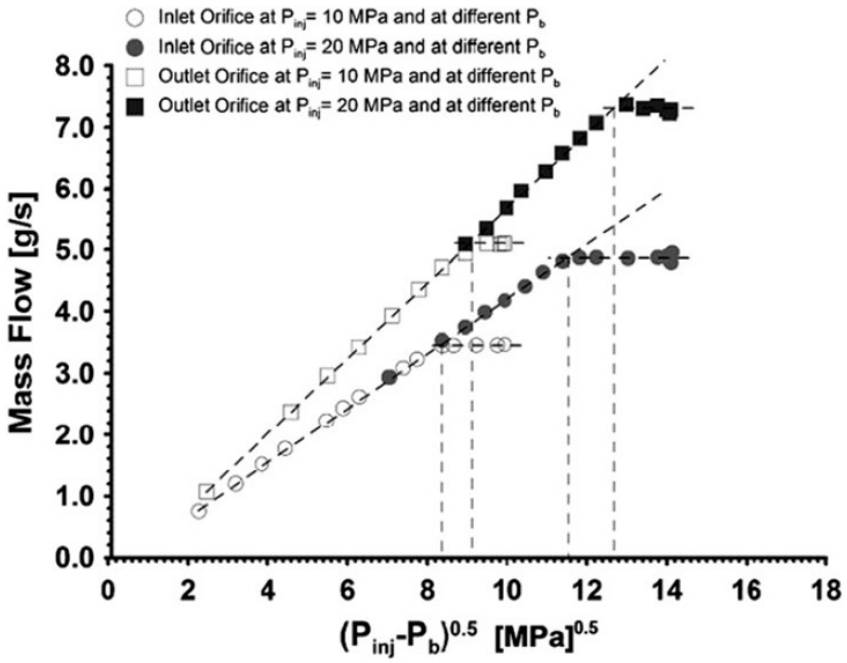

Figure 0-4 Mass flow against square root of pressure drop for the fuel oil inlet and outlet passages

The Reynolds number can be get by equation (A.2):

$$\mathrm{Re} = \frac{D_o U_o}{v_f} \tag{A.2}$$

Where, D_o is the outlet diameter, U_o is the velocity if the orifice outlet, and v_f is the kinematic viscosity.

The discharge coefficient of the nozzle against the Reynolds number is shown in **Error! Reference source not found.**.

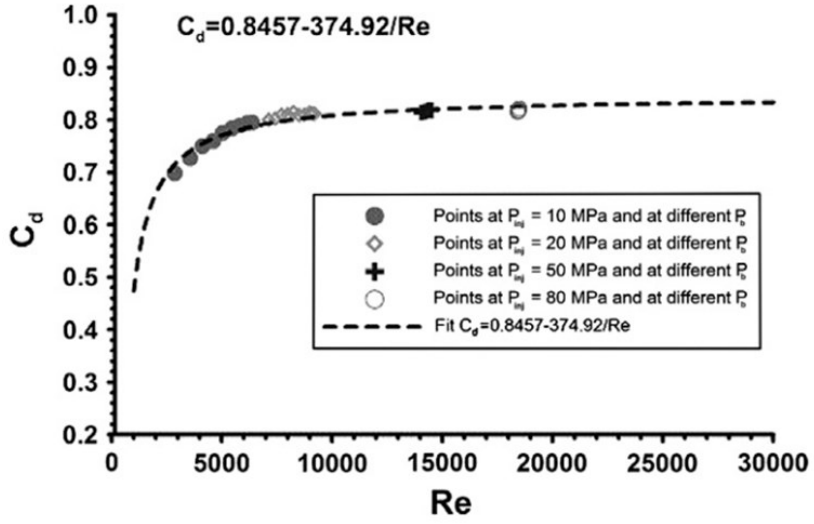

Figure 0-5 The discharge coefficient of the nozzle orifices against the Reynolds number

From **Error! Reference source not found.**, the cavitation happens when the mass flow rate stops increasing with the increase in pressure difference. The cavitation number definition used by Soteriou et al. [103] was introduced.

$$CN = \frac{P_{inj} - P_b}{P_b - P_v} \tag{A.3}$$

Where, P_v is the saturation vapor pressure, it can be ignored since it is too small to be considered by comparing to the injection pressure or the back pressure.

The critical cavitation number is defined as CN_{crit}, From **Error! Reference source not found.**, the critical cavitation number are 2.4 and 2 for the control oil inlet passage at 10 MPa and 20 MPa rail pressure respectively. While $CN_{crit} = 4.82$ and $CN_{crit} = 4.17$ for the control oil outlet passage respectively.

If cavitation happens, the discharge coefficient can be calculated by the following equation:

$$C_d = C_c \sqrt{1 + \frac{1}{CN}} \tag{A.4}$$

Where, C_c is the contraction coefficient in the orifice owing to cavitation phenomena which can be easily obtained particularizing that equation for the critical cavitation conditions.

If the cavitation does not occur in passages or orifices, their discharge coefficient refers to **Error! Reference source not found.**.

Appendix B: RSM method

K-nearest

The k-nearest method [104] used in Chapter 3 and Chapter 4 for generating RSM contour maps is a non-parametric classification and regression method with non-intensively computation.

Assume a training dataset,

$$D := \{(x_i, y_i) : x_i \in \Omega \subset R^M, y_i \in R, i = 1,...,n\} \tag{B.1}$$

Consisting of points $x_i \in \Omega$ and respective values $y_i \in R$ be assigned, $s_k(x)$ is defined as the interpolate value to be determined. The k-nearest average will be only on the nearest k data points to the unknown point x , for every $x \in \Omega$, sort $x_1,...,x_n$ in proximity order,

$$i : \{1,...,n\} \times \Omega \to \{1,...,n\} \tag{B.2}$$

$$(j,x) \to i(j,x) \tag{B.3}$$

$$\{x_{i(1,x)},...,x_{i(n,x)}\} = \{x_1,...,x_n\} \tag{B.4}$$

$$\| x - x_{i(j,x)} \| \leq \| x - x_{i(j+1,x)} \| \tag{B.5}$$

Thus, the k-nearest method is defined as follows,

$$s_k(x) := \begin{cases} \sum_{j=1}^{k} \frac{\| x - x_{i(j,x)} \|^{-p}}{\sum_{j=1}^{k} \| x - x_{i(j,x)} \|^{-p}} y_{i(j,x)} & if \quad x \neq x_i, \forall i = 1,...,n \\ y_i & if \quad x = x_i \end{cases} \tag{B.6}$$

Neural networks

Neural networks used for generating RSM contour maps in Chapter 7 are based on the idea of imitating the structure of information process in human brains. They are made up of fundamental computing units and perceptrons, which are assembled to form a network. Neural networks are suitable for nonlinear problems by introducing nonlinear transformations to the flow of information between the layers of perceptrons [105].

The neural networks used here is a classical feedforward one, with one hidden layer and an efficient Levenberg-Marquardt back propagation training algorithm. The scheme of typical classical feedforward neural networks is depicted in **Error! Reference source not found.**. It is also called multilayer perceptron neural network. In this type of network, all units are arranged in a layered feedforward topology. Each input units x_i are connected with all of the hidden units h_j with weights. The hidden layer also is connected to the output units y_k in a similar manner with different weights [105, 106]. Levenberg-Marquardt algorithm is popular for neural networks training. It was independently developed by Kenneth Levenberg and Donald Marquardt [107,108]. It solves a problem by minimizing a non-linear function with fast speed and stable convergence.

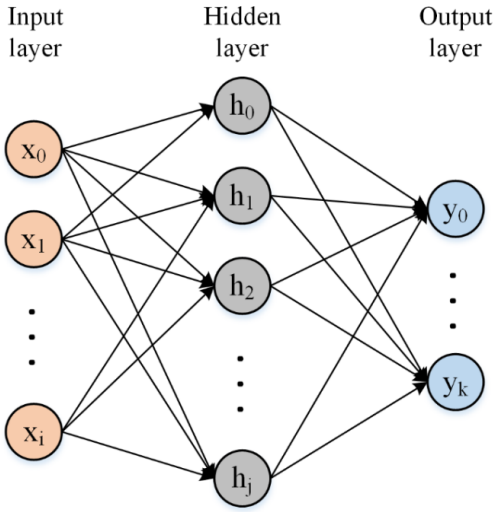

Figure 0-6 Architecture of classical feedforward neural networks